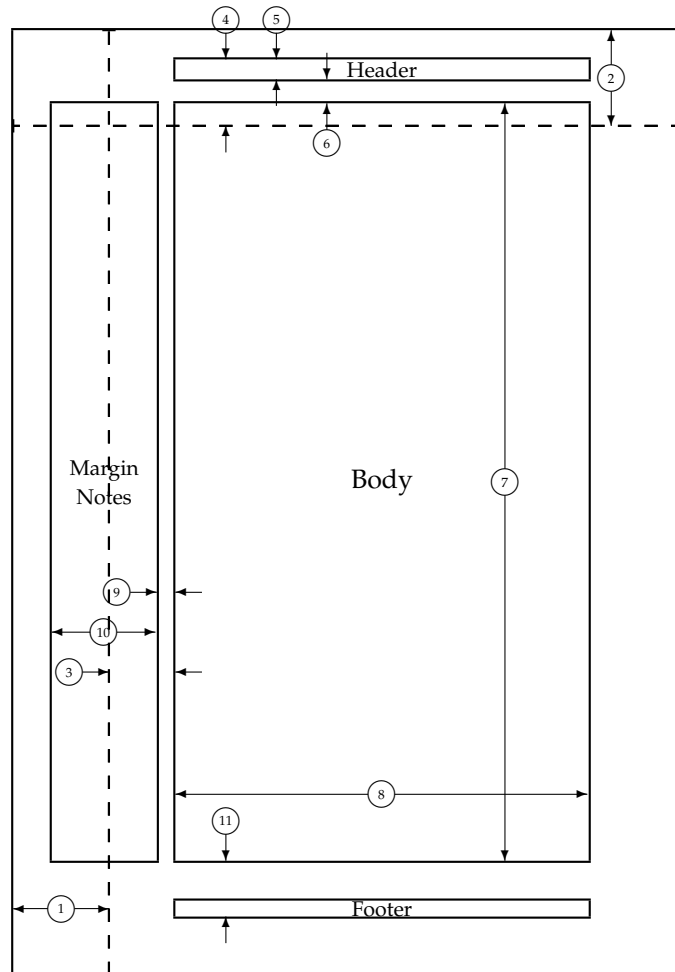


1 one inch + \hoffset	2 one inch + \voffset
3 \oddsidemargin = -5pt	4 \topmargin = -50pt
5 \headheight = 15pt	6 \headsep = 18pt
7 \textheight = 570pt	8 \textwidth = 311pt
9 \marginparsep = 14pt	10 \marginparwidth = 79pt
11 \footskip = 42pt	\marginparpush = 5pt (not shown)
\hoffset = 0pt	\voffset = 0pt
\paperwidth = 500pt	\paperheight = 711pt



- 1 one inch + \hoffset
- 2 one inch + \voffset
- 3 \evensidemargin = 50pt
- 4 \topmargin = -50pt
- 5 \headheight = 15pt
- 6 \headsep = 18pt
- 7 \textheight = 570pt
- 8 \textwidth = 311pt
- 9 \marginparsep = 14pt
- 10 \marginparwidth = 79pt
- 11 \marginparpush = 5pt (not shown)
- \footskip = 42pt
- \hoffset = 0pt
- \paperwidth = 500pt
- \voffset = 0pt
- \paperheight = 711pt

MIQUEL CASADEMONT VIÑAS

ADVANCES OF RAINBOW ORGANIC SOLAR CELLS

ADVANCES OF RAINBOW ORGANIC SOLAR CELLS

MIQUEL CASADEMONT VIÑAS



Facultat de ciències i biociències
Universitat autònoma de Barcelona (UAB)

Institut de ciència de materials (ICMAB)
Nanostructured Materials for Optoelectronics and Energy Harvesting
(NANOPTO)

PhD in Materials Science
October 2024

The real innovators did their innovating just by being themselves.

Count Basie

Life is a lot like jazz. It's best when you improvise.

George Gershwin

Dedicat als meus pares i als meus avis,
a qui els hi dec la vida.

ABSTRACT

Abstract in english

RESUM

Resum en català

RESUMEN

Resumen en castellano

PUBLICATIONS

1. Casademont-Viñas, M., Capolat, D., Quesada-Ramírez, A., Reinfelds, M., Trimmel, G., Sanviti, M., Martín, J., Goñi, A. R., Kirchartz, T. & Campoy-Quiles, M. Combinatorial screening of wide bandgap organic solar cell materials with open-circuit voltage between 1.1 and 1.4 V. *Journal of Materials Chemistry A*. ISSN: 2050-7488. <https://xlink.rsc.org/?DOI=D4TA01944J> (2024).
2. Casademont-Viñas, M., Gibert-Roca, M., Campoy-Quiles, M. & Goñi, A. R. Spectrum on demand light source (SOLS) for advanced photovoltaic characterization. *Review of Scientific Instruments* **94**, 103907. ISSN: 10897623. [/aip/rsi/article/94/10/103907/2917787/Spectrum-on-demand-light-source-SOLS-for-advanced](https://aip.org/doi/10.1063/5.017787) (10 Oct. 2023).
3. Gibert-Roca, M., Casademont-Viñas, M., Liu, Q., Vandewal, K., Goñi, A. R. & Campoy-Quiles, M. RAINBOW Organic Solar Cells: Implementing Spectral Splitting in Lateral Multi-Junction Architectures. *Advanced Materials*, 2212226. ISSN: 0935-9648. <https://onlinelibrary.wiley.com/doi/10.1002/adma.202212226> (Apr. 2023).
4. Gibert-Roca, M., Casademont-Viñas, M., Goñi, A. R. & Campoy-Quiles, M. *Spectral shaper illumination device* 2023. <https://patents.google.com/patent/WO2023227290A1/en?oq=WO2023227290A1>.

ACKNOWLEDGMENTS

Put your acknowledgments here.

CONTENTS

1	Introduction	1
1.1	Motivation	1
1.1.1	Environmental scenario	1
1.1.2	Photovoltaic technologies	2
1.2	Organic photovoltaics	3
1.2.1	Organic semiconductors	3
1.2.2	Working principles	3
1.2.3	Device geometry	3
1.2.4	Figures of merit	3
1.3	Multi-junction organic solar cells	3
1.3.1	The Shockley-Queisser limit	3
1.3.2	Multi-junction solar cells geometries	3
1.3.3	The RAINBOW geometry	3
2	Materials and methods	5
2.1	Organic solar cell fabrication	5
2.1.1	Substrate cleaning protocol	5
2.1.2	Electron Transport Layer (ETL)	6
2.1.3	Active Layer (AL)	6
2.1.4	Hole Transport Layer (HTL) and back electrode	7
2.2	$J - V$ curve characterization	7
2.2.1	partial coverage radial (PCR) spin coating	7
3	Spectrum On demand Light Source (SOLS)	11
3.1	State of the art	11
3.2	SOLS setup embodiment	14
3.2.1	Dispersive element	16
3.2.2	Filtering element: 3D-printed masking cards	17
3.2.3	Filtering element: guillotines	23
3.2.4	Reconcentrator and homogenizer	26
3.3	Output light characterization	28
3.3.1	Measuring the output spectrum	28
3.3.2	Spectral match	29
3.3.3	Spatial non-uniformity	30
3.3.4	Temporal instability	32
3.4	Limitations, conclusions, and outlook	33
3.4.1	Spectral resolution	33
3.4.2	External Quantum Efficiency	36
3.4.3	Conclusions and outlook	38
4	RAINBOW solar cells	41
4.1	Introduction	41
4.2	Toolkit for RAINBOW optimization	44
4.2.1	RAINBOW concept	44

xiv CONTENTS

4.2.2	RAINBOW simulation model	45
4.2.3	RAINBOW characterization with SOLS	51
4.2.4	Monolithic proof-of-concept device	59
4.3	RAINBOW simulations with multiple materials	64
4.3.1	Effect of active layer thickness	64
5	Wide band-gap organic photovoltaics	67
5.1	Introduction	67
5.2	Combinatorial screening	69
5.2.1	Active layer materials	69
5.2.2	$J-V$ characterization	77
5.2.3	V_{oc} loss analysis	86
5.2.4	FCC-Cl as a promising wide band-gap NFA	92
5.3	Application examples of wide band-gap OPV	93
5.3.1	Indoor light harvesting	93
5.3.2	RAINBOW solar cells	97
5.4	Upscaling of PTQ10:O-IDFBR OPV	98
5.4.1	Depositing the active layer at ambient air	98
5.4.2	Effect of cell width on modules performance	100
5.4.3	Studying cell width dependence	102
5.5	Conclusions and outlook	105
	Bibliography	107

LIST OF FIGURES

Figure 2.1	PCR Spin coating working principle and substrates	8
Figure 2.2	PCR Spin Coating Raman Characterization	9
Figure 3.1	Examples of useful spectra for novel applications of OPV.	12
Figure 3.2	SOLS setup schematics	15
Figure 3.3	Light dispersion by the double Amici Prism.	17
Figure 3.4	3D-printed masking card schematics.	18
Figure 3.5	Examples of the slits system for the calibration of 3D-printed masks.	19
Figure 3.6	Spectra basis vectors for 3D-printed masks.	20
Figure 3.7	Slits calibration system imperfections	20
Figure 3.8	Spectra from 3D-printed masking cards examples	21
Figure 3.9	Masking cards encoding fitted spectra from Figure 3.8	21
Figure 3.10	Comparison of OPV performance under 1 Sun measured with SOLS and with Xenon arc lamp solar simulator.	22
Figure 3.11	Schematics of the motorized blue guillotine	24
Figure 3.12	Results of the motorized guillotines calibration	25
Figure 3.14	Effect of the homogenizing apparatus	26
Figure 3.13	Degradation of the custom mirror Ag surface.	27
Figure 3.15	SOLS output spectrum measurement	28
Figure 3.16	Workflow diagram for the measurement of a SOLS spectrum.	29
Figure 3.17	Spatial non-homogeneity classification.	31
Figure 3.18	Effect of input light collimation and width reduction to wavelength resolution.	34
Figure 3.19	Half width at half maximum (HWHM) as a function of the central wavelength for the slit spectra shown in Figure 3.18.	35
Figure 3.20	Slits-EQE _{PV} measurements with different input light treatments.	38
Figure 3.21	Sweep-EQE _{PV} measurement of a PM6:IO-4Cl solar cell.	39
Figure 4.1	Schematics of different multi-junction geometries	42
Figure 4.2	Rainbow simulation with equal sub-cells	48

xvi LIST OF FIGURES

Figure 4.3	Relevant examples of RAINBOW simulations with top-hap EQE_{PV}	49
Figure 4.4	Main sentence	50
Figure 4.5	EQE_{PV} and $J - V$ curves of the selected materials used for the simulation model	53
Figure 4.6	RAINBOW simulations with solar cells fabricated with the selected materials.	54
Figure 4.7	Results of RAINBOW characterization with SOLS	
Figure 4.8	RAINBOW analysis with SOLS characterization for PTB7-Th:COTC-4F // PM6:IO-4Cl and for PTB7-Th:COTIC-4F // PM6:Y6 2-J RAINBOW systems.	57
Figure 4.9	Simulations to determine the effect of the spectral resolution of the SOLS setup on RAINBOW performance	58
Figure 4.10	Monolithic RAINBOW performance calculations	60
Figure 4.11	LED solar simulator custom spectra	61
Figure 5.1	Photographs of all 18 samples prepared in the wide E_{bg} combinatorial screening	71
Figure 5.2	HOMO and LUMO energy levels of the materials selected for the wide E_{bg} combinatorial screening	72
Figure 5.3	Refractive index n and extinction coefficient k of the wide E_{bg} donors and acceptors	73
Figure 5.4	GIWAXS results for PTQ10:O-IDFBR material system deposited from CB and CF	75
Figure 5.5	GIWAXS results for PTQ10:IO-4Cl material system deposited from CB and CF	76
Figure 5.6	Dependence of PCE on active layer thickness	78
Figure 5.7	$J - V$ curves of the best performing cells for each of the six materials tested (donors and acceptors)	78
Figure 5.8	Best power conversion efficiency (PCE) values as a function of the corresponding V_{oc} achieved for each donor-acceptor-solvent combination	80
Figure 5.9	V_{oc} heatmap of all donor-acceptor-solvent combinations	81
Figure 5.10	Energy difference between $LUMO_{acceptor}$ s and the $HUMO_{donor}$ as a function of V_{oc}	82
Figure 5.11	$J - V$ measurements results for the two IO-4Cl batches used	83
Figure 5.12	FF vs. V_{oc} for the 18 best-performing devices of the combinatorial screening	84
Figure 5.13	J_{sc} results	85

Figure 5.14	EL fits for extend the EQE_{PV} for V_{oc} losses calculations	88
Figure 5.15	ΔV_{oc} loss analysis	91
Figure 5.16	ΔV_{oc}^{nr} as a function of V_{oc}^r compared with literature	92
Figure 5.17	Thickness dependence FoM of PTQ10:FCC-Cl sample	93
Figure 5.18	Characteristics of LED light source for indoor measurements in Figure 5.19	94
Figure 5.19	Indoor characterization of PTQ10:O-IDFBR deposited from CB sample	95
Figure 5.20	Evaluation PTQ10:O-IDFBR leakage with light-intensity dependent measurements	96
Figure 5.21	Comparison with the state-of-the-art indoor organic solar cell efficiency	97
Figure 5.22	Comparison between solar cells of PTQ10:O-IDFBR prepared inside and outside the glovebox.	99
Figure 5.23	Schematics of laser patterning used to fabricate PTQ10:O-IDFBR modules	101
Figure 5.24	Electroluminescence of a module where P1 final laser patterning is not done correctly	102
Figure 5.25	Geometrical fill factor for the modules fabricated	103
Figure 5.26	Optical microscopy images of the interconnection between cells	103
Figure 5.27	Cell width study of PTQ10:O-IDFBR modules	104

LIST OF TABLES

Table 3.1	Class A, B and C Standards and Specifications Defined by ASTM E 927-10.	28
Table 3.2	Classification following the ASTM E927-10 standards of the four spectra shown in Figure 3.8.	30
Table 3.3	Short-term instability (STI) and long-term instability (LTI) of the input and output light of the SOLS	33
Table 4.1	V_{oc} losses of the blends studied	53
Table 4.2	Figures-of-merit of the active layer materials selected for the RAINBOW study	54

Table 4.3	RAINBOW FoM for materials simulations shown in Figure 4.6. *The third combination c), do not show any RAINBOW efficiency increase. For this reason, IoBC is 0, and $\lambda_{d,\text{opt}}$ do not has a value. 55
Table 4.4	RAINBOW FoM of the SOLS characterization of Figure 4.8 58
Table 4.5	Monolithic RAINBOW device performance, with PM6:IO-4Cl as the blue sub-cell and PTB7-Th:COTIC-4F as the red sub-cell 61
Table 4.6	Monolithic RAINBOW device performance, with PM6:Y6 as the blue sub-cell and PTB7-Th:COTIC-4F as the red sub-cell 62
Table 4.7	Comparison between the RAINBOW characterization with LEDs solar simulator and the simulations for the two RAINBOW systems studied 63
Table 5.1	State of the art of the wide E_{bg} blends explored. 70
Table 5.2	Comparison of E_{bg} of materials measured with different methods 73
Table 5.3	d-spacing (d) and coherence length (L_c) analysis for (100), (010) planes, and low q region 77
Table 5.4	Figures-of-merit from $J - V$ measurements. 79
Table 5.5	Benchmark of PM6:IO-4Cl and D18:PPMI-FF-PMI active layer systems 82
Table 5.6	Results of V_{oc}^{r} calculation 90
Table 5.7	Tabulated values of V_{oc} losses analysis 90

ACRONYMS

1

INTRODUCTION

1.1 MOTIVATION

1.1.1 *Environmental scenario*

Humankind is nowadays facing one of the most challenging technological problems: the increasing energy consumption and the environmental impact of its production. The economy of developed countries, centered on high consumption of resources, and the impact of countries in development is increasing the energy demand. Fossil fuels has been the main, and during most of the time the unique, source for energy production resulting in an increasing concentration of greenhouse gases on earth atmosphere increasing the greenhouse effect resulting in the so called global warming. The later leaded to an alarming climate change which nowadays is present in our daily lives. For example, the storms Gloria and Filomena that happened in Catalunya during the years 2020 and 2021 are examples of metheorologic phenomena not common of a Mediterranean region. These are just examples of the already proved climate change and global warming, which according to the actual scientific community has arrived to an inflection point where the damaged produced to earth environment in the past is almost impossible to solve in the near future.

Nevertheless, it is still in our hands the responsibility of learning from the errors of the past humankind to have the best possible future. In this direction, replacing the actual fossil fuels for renewable energy sources is mandatory to reduce the greenhouse gases in the atmosphere and mitigate the climate change. This was the objective of the Neat Zero scenario proposed by the United Nations on 2015.[UNNeatZero] The actual Neat Zero agreement is to reduce to zero the greenhouse gas emissions by 2050. In this transition, renewable energies are key and scientific and political efforts are needed to develop new green technologies. One of the drawbacks of renewable energy sources is the incapability of on-demand production, both in time and space. For this reason, the development of all kind of renewable energy sources is needed for a successful future reduction of fossil fuels as well as a green solution for energy storage and distribution.[IEAEnergyOutlook2023] Nevertheless, among all the renewable energy sources there are some specially promising considering the vast amount of energy available. These are the technologies taking the solar light as the energy source.

2 INTRODUCTION

The energy received from the sun at earth surface in one hour (posarnum) is in the order of the humankind energy consumption during one year (posarnum). Among all different technologies that harvest this solar energy, the photovoltaic (PV) solar cells are devices that directly convert the received sunlight into electricity, the most used energy vector of humankind.

The last report on renewable energies from the international energy agency (IEA) states that Solar PV generation increased by a record 270 TWh (up 26%) in 2022, reaching almost 1300 TWh.[**IEARenewables2023**] It demonstrated the largest absolute generation growth of all renewable technologies in 2022, surpassing wind for the first time in history. This generation growth rate matches the level envisaged from 2023 to 2030 in the Net Zero Emissions by 2050 Scenario. Continuous growth in the economic attractiveness of PV, massive development in the supply chain and increasing policy support, especially in China, the United States, the European Union and India, are expected to further accelerate capacity growth in the coming years.[**IEARenewables2023**]

1.1.2 Photovoltaic technologies

In the actual scenario, the energy produced by photovoltaic modules represents the X% of all energy production. Its main contribution comes from silicon solar cells, efficiencies reaching XX% and with its production cost scaling down (XXX per XXXXX) facilitating the implementation of photovoltaic energy harvesting. Historically, the active layer of the first silicon solar cells were composed by thick crystalline silicon, which results in high weight and brittle modules with dark appearance. Those are known as first generation solar cells, and while their properties are suitable for being installed in roofs or solar farms, it is difficult to imagine its implementation in other applications such as portable objects or aesthetic architecture. Nevertheless, actual commercial silicon modules are not composed of thick crystalline silicon but thin-film amorphous silicon. These modules are considered the second generation family and improves the lightness, brittleness and cost of first generation silicon solar cells. This generation comprises any thin-film photovoltaic technology composed of inorganic materials, which includes Cadmium Telluride (CdTe), copper indium gallium selenide (CIGS) or Gallium Arsenide (GaAs). It is worth mentioning the band-gap tunability of the mentioned inorganic semiconductors, which enabled the multi-junction approach leading to the highest efficiencies achieved in the photovoltaic solar cells. Nevertheless, the use of these materials introduces new drawbacks such as its toxicity or the scarce of the materials compared to the second most common element in earth's crust (silicon).//

BlaBlaBla...

1.2 ORGANIC PHOTOVOLTAICS

Photovoltaic solar cells are capable of converting energy from light (i.e. photons) into electrical energy (i.e. electrons). From a solid-state physics point of view, this effect takes place in semi-conductor materials. These materials,

1.2.1 *Organic semiconductors*

1.2.2 *Working principles*

1.2.3 *Device geometry*

1.2.4 *Figures of merit*

1.3 MULTI-JUNCTION ORGANIC SOLAR CELLS

1.3.1 *The Shockley-Queisser limit*

1.3.2 *Multi-junction solar cells geometries*

1.3.3 *The RAINBOW geometry*

2

MATERIALS AND METHODS

In this chapter...

2.1 ORGANIC SOLAR CELL FABRICATION

The fabrication of organic solar cells is a fundamental procedure during the development of this thesis. In this scope, the knowledge of the NANOPTO group is a valuable resource. All solar cells fabricated in this thesis have the inverted geometry, i.e. the electron transport layer (ETL) is near the transparent electrode while the hole transport layer (HTL) is at the back reflective contact side. During the first stages of the thesis, some devices were fabricated in the normal geometry, however these results are not part of the manuscript. This section intends to describe the standard procedure of device fabrication at the NANOPTO group. Materials and methodologies that differ from the standard in certain parts of this thesis manuscript are described in their corresponding place.

2.1.1 *Substrate cleaning protocol*

The fabrication starts with glass substrates that are coated with ITO with a certain pattern. These substrates are bought from Ossila and the dimensions of the substrate and the patterned ITO are depicted in XXX. This patterning defines a total of 24 cells, 12 on each side of the substrate. To identify the substrates afterward, they are manually scratched from the glass side with a diamond tip. These marks have to be done outside the area of the working devices and would be unique for every substrate one may ever fabricate. Afterward, substrates are cleaned by sequentially sonicating them in acetone, 2% vol% Hellmanex[©] soap solution in H₂O, isopropanol and 10% sodium NaOH solution in H₂O; during 5, 5, 5, and 10 minutes respectively. The first tree baths aim to clean the surface from any organic moiety, while the last bath aims to activate the surface of the ITO to improve wettability for the blade-coating deposition of the ETL. Afterward, the samples are submerged in H₂O to clean any remaining NaOH and the H₂O is washed from the substrate with compressed air. In this last step, it is important to avoid the evaporation of the water on the substrate surface since it could lead to the deposition of any impurity present in the water. On the contrary, compressed air has to be used to push the water to one side of the

6 MATERIALS AND METHODS

substrate where a clean room wipe can suck it.

2.1.2 Electron Transport Layer (ETL)

The first layer deposited is the electrode transport layer (ETL). In the standard procedure, a solution of ZnO nanoparticles bought from Avantama (Avantama N10) is deposited via blade coating with a constant blade speed of 5 mm/s, a blade gap of 50 μm , and a temperature of 40 °C. Afterward, the layer is cleaned on the sides of the substrate to avoid electrical shortcuts of the contacts to form the desired device structure. This is done with the help of a 3D printed guide and a cleaning wipe wetted with isopropanol. Finally, annealing at 110 °C is done to evaporate all remaining solvent and form a compact layer difficult to scratch. The resulting thickness is between 30 and 35 nm.
add an image of the 3d printed guide in the sidenote?

2.1.3 Active Layer (AL)

The desired O₂ and H₂O are below 1.5 parts per million (ppm)

Make a small table with solvents and recommended stirring temperatures

The active layer (AL) is generally deposited inside the glovebox, where the controlled low levels of O₂ and H₂O prevents the degradation of the organic materials forming the active layer. For this reason, it is also recommended to store the organic materials and prepare the solutions for the AL deposition inside the glovebox. The solutions are generally prepared at 1:1.5 donor:acceptor ratio with a 15 – 20 mg of solute for each mL of solvent. Nevertheless, the solution composition cannot be generalized to any material combination since it is one of the most important parameters affecting the final efficiency. The solutions are kept in stirring for at least 4 hours to ensure proper dissolution of the materials. Generally applying temperature helps to the dissolution process, nevertheless it can never be higher than the boiling point of the solvent to avoid its evaporation, which would cause a change in the solution concentration.

As a general rule, the active layer is deposited with a thickness gradient along the long side of the substrate to evaluate the effect of thickness on the device performance, resulting in 12 device pairs of different thicknesses (a total of 24 devices per substrate). This is achieved thanks to the deacceleration of the blade during the deposition of the active layer, which is controlled thanks to an Arduino electrically connected to the blade moving motor. This modification was done by Dr. Bernhard Döring during his PhD thesis^{ref}. To achieve a thickness gradient between 250 and 40 nm approximately, the blade speed is linearly decreased from 90 mm/s to 10 mm/s between the first and the

last cell of the substrate respectively. To align the blade speed gradient with the sample, one sacrificial glass is added before the substrate. Additionally, a sacrificial glass after the substrate is used to avoid the evaporation of the remaining solution at the edge of the substrate. Finally, similarly to the ETL, the active layer is cleaned in the laterals to build the proper cell geometry and avoid any possible electrical leakage. At this point, annealing treatment (if desired) can be done before the evaporation of the hole transport layer (HTL) and the back electrode.

2.1.4 Hole Transport Layer (HTL) and back electrode

The last step of the device fabrication is the evaporation of the hole transport layer (HTL) and the back electrode. An evaporation mask is used to define the desired pattern of the evaporated layers. The mask shape can be seen at [xxx](#). The standard procedure consists of depositing between 10 and 15 nm of molybdenum (VI) oxide (MoO_3) as HTL. In general, a thick MoO_3 would increase the selectivity of the HTL increasing the fill factor (FF) of the resulting solar cell at expenses of free charges reaching the contacts (i.e. less photocurrent (J_{sc})). The latter also results in a lower dark current, generally desired for photodetectors. A thin MoO_3 will have the opposite effect, increasing J_{sc} at expenses of FF . Finally, a minimum of 150 nm of silver (Ag) is deposited as the reflective back electrode to ensure an electrically conductive contact.

2.2 $J - V$ CURVE CHARACTERIZATION

2.2.1 partial coverage radial (PCR) spin coating

This technique consists in depositing the solution in only one half of the substrate, and regulating the amount of liquid, maximum angular velocity and acceleration, to reliably cover half of the substrate, leaving the other half completely untainted (Figure ?? (a)). The working principle of this technique relies on the fact that the liquid will only try to move outwards within the substrate due to centrifugal forces, preventing the uncovered side from getting contaminated.

This new technique allows to partially cover a substrate with, in principle, n different layers, as long as they are radially distributed, since the main force the liquid experiences is radially pointing outwards, forcing the liquid away from the center. With this technique, we were able to deposit up to 4 different solutions on a single substrate by depositing them in a radial distribution (Figure ?? (c)). Consequently,

8 MATERIALS AND METHODS

we have named this technique Partial Coverage Radial (PCR) spin coating.

One limitation of this technique is that if we do not correctly adjust the amount of liquid, the angular velocity and acceleration, the solution can be dragged through the substrate, staining the uncovered part (Figure ?? (d)). However, tuning the parameters makes it easy to achieve optimal deposition conditions. For a small $20 \times 15 \text{ mm}^2$ substrate we typically use around $25 \mu\text{l}$, with angular accelerations as low as 100 rpm s^{-1} , with higher viscosity liquids allowing for higher angular accelerations. The other main disadvantage is that the precision of the partial coverage greatly depends on the steady hand of the operator during the deposition. To mitigate this, we have 3D-printed a guide that guarantees a straight line every time.

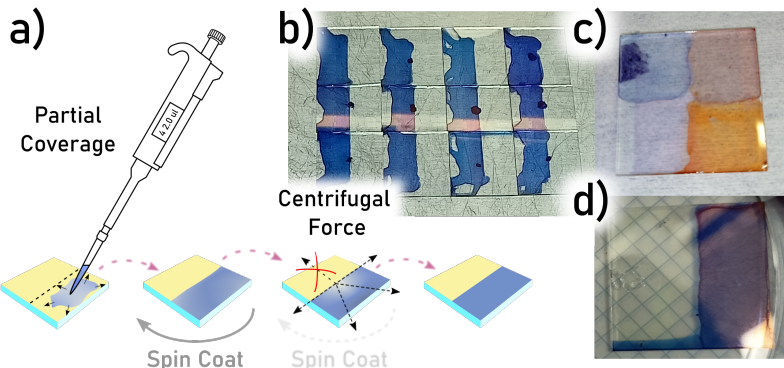


Figure 2.1: (a) PCR spin coating working principle and steps. (b) Partially spin coated substrates with a high degree of repeatability, with (c) up to four different layers on the same substrate without cross contamination. (d) Unoptimized angular velocity and acceleration lead to cross contamination as illustrated in this photograph.

The assessment of the quality of the deposition using the PCR method has been carried out by Raman scattering imaging, as illustrated in Figure ???. Two excitation wavelengths were used to selectively probe the two systems, namely 785 nm for PTB7-Th:COTIC-4f and 488 nm for PBDB-T-2F:IO-4Cl. The Raman peak centered at 1322 cm^{-1} corresponds to the signal of PTB7-Th:COTIC-4f. By integrating the intensity of this peak over the scanned region, we can clearly see that this blend only appears on the left part of the device (Figure ?? (b)). Similarly, by monitoring a peak centered at 1428 cm^{-1} we can see the signal of PBDB-T-2F:IO-4Cl, and how this material is only distributed on the right hand side of the sample (Figure ?? (c)). The absence of any significant intermixing between the materials of two adjacent sub-cells sequentially deposited with the PCR method is clearly demonstrated

by the sharpness and negligible overlap of the Raman profiles shown in Figure ?? (e), each one corresponding to a characteristic Raman peak of each organic blend. Interestingly, applying a cluster analysis to the data (not shown) also demonstrates the existence of two distinctive spectra, one for each side. Note that the signal of the blend is higher under the metal electrode due to the enhanced electric field granted by strong light reflection at the metal.

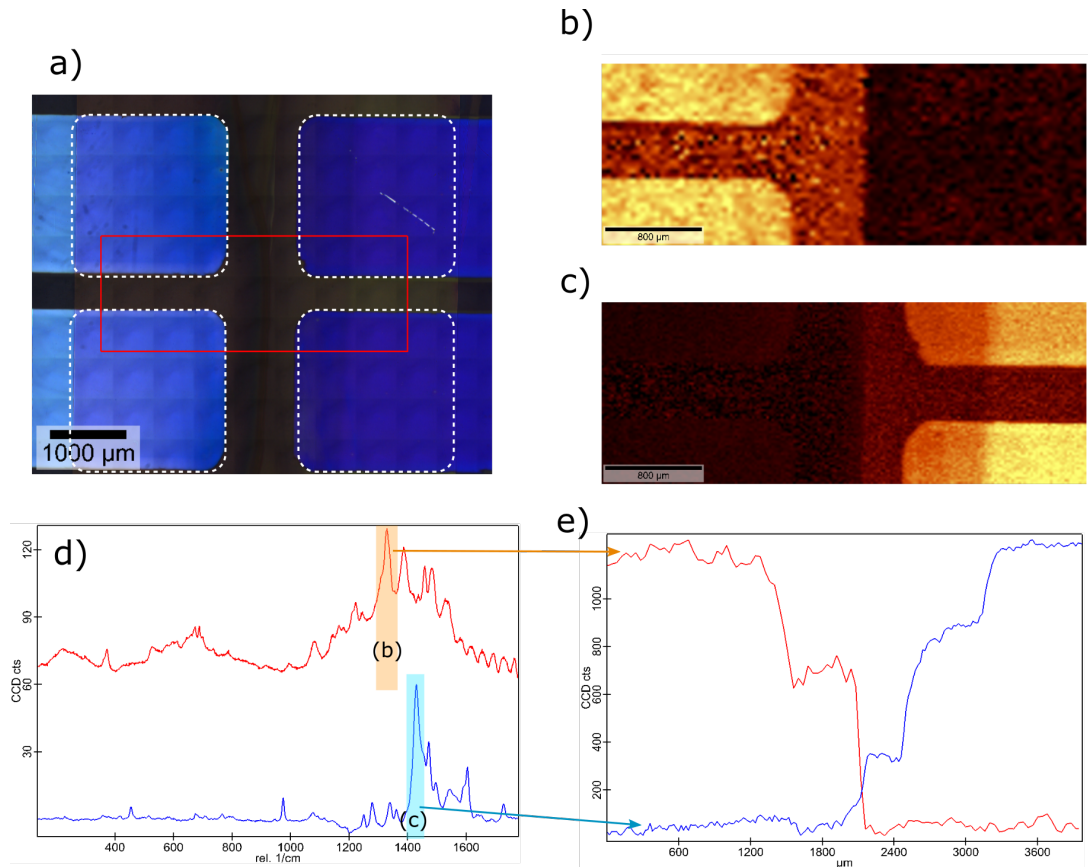


Figure 2.2: Raman characterization of the RAINBOW monolithic proof-of-concept device fabricated using the PCR spin-coating technique. PTB7-Th:COTIC-4f and PBDB-T-2F:IO-4Cl corresponds respectively to the left and right half of the substrate. (a) Stitching image of the measured sample where 4 devices (discontinuous white squares) are shown as well as the region where Raman spectra was measured (red rectangle). (b) Raman intensity map corresponding to peak at 1322 cm^{-1} acquired with 785 nm laser excitation (spectrum shown in (d) panel in red). (c) Raman intensity map corresponding to peak centered at 1428 cm^{-1} acquired with 488 nm laser excitation (spectrum shown in (d) panel in blue). (d) Raman spectrum of PTB7-Th:COTIC-4f when excited with 785 nm laser (red) and PBDB-T-2F:IO-4Cl when excited with 488 nm laser (blue). Panel (e) corresponds to the integrated intensity of panels (b) and (c) in the horizontal direction and shows that the step between the two materials is on the order of tenths of μm .

3

SPECTRUM ON DEMAND LIGHT SOURCE (SOLS)

This chapter describes a setup named Spectrum On demand Light Source (SOLS) which was developed during the first stages of the thesis and has been improved throughout the whole thesis.^[1] Although the motivation behind SOLS was the characterization of RINABOW sub-cells, its posterior development led to a setup with more potential. For this reason, SOLS application examples are present in other thesis chapters. Moreover, intellectual property was protected by a patent.^[2] The latter was a great opportunity to be conscious of the importance of technology transfer inside the academic environment. It was also a good opportunity to learn more about this complex field. This chapter first introduces the state of the art and motivation behind SOLS development. Afterward, it describes the setup embodiment used in the lab and its working principles. The most important parts are explained in depth in order to provide a better description of the setup and its possibilities. The output light is also classified as a solar simulator following ASTM standards. Finally, the chapter proposes ideas to improve the setup and describes the next steps to produce a first pre-industrial prototype.

3.1 STATE OF THE ART

Developing and optimizing materials for emergent photovoltaic technologies to work in different conditions and environments increasingly calls for novel light sources capable of adapting the irradiance conditions to the targeted application. Examples include modules placed on vertical walls (e.g. for building integrated PV),^[3] at different altitudes (and thus different UV amounts),^[4] different air masses and turbidities,^[5] underwater photovoltaics^[6] or for indoor applications.^[7, 8, 9] Moreover, multi-junction solar cells based on the spectral splitting concept have recently attracted renewed attention.^[10, 11, 12, 13] In this case, an optical element separates the sunlight into a number of beams exhibiting different spectral ranges that match the bandgap of each sub-cell. For optimizing this geometry, each sub-cell should be investigated as a function of a fraction of the sun spectrum. Sources capable of producing tunable low and high-wavelength pass and band-pass filters would be needed. While promising results have been obtained for different applications, we believe the field would greatly benefit from novel characterization tools that could help to adapt studies to specific

See [Figure 3.1](#) for spectra examples of different air masses (a), artificial indoor light (b), underwater (c), and tunable filter (d).

geometries and applications.

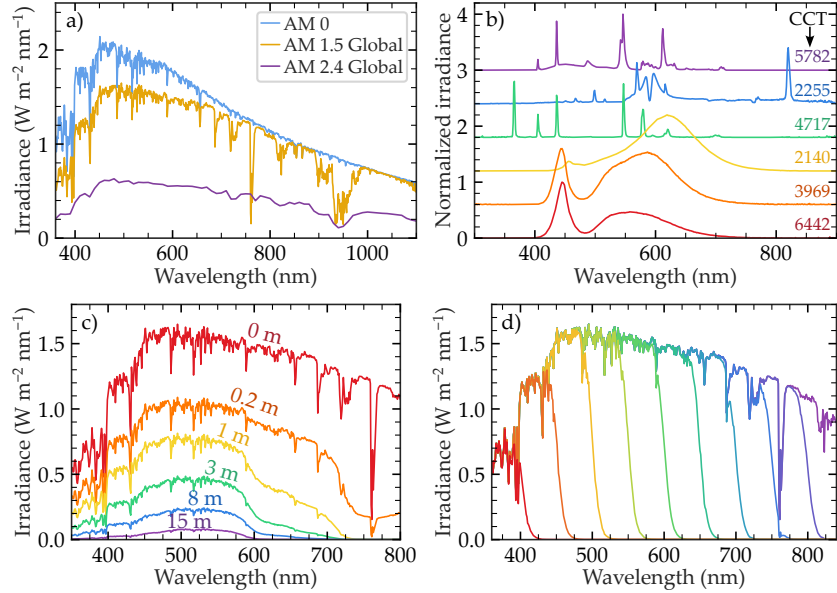


Figure 3.1: Examples of useful spectra for novel applications of OPV. (a) Spacial AM 0 spectrum (blue) and terrestrial AM 1.5 Global (yellow).[14] Purple spectrum is calculated using [15] at my hometown (Torrella de Montgrí) on day 2024/05/24 at 17 h corresponding to an air-mass of 2.42. (b) Examples of artificial light sources measured in Madrid city corresponding to compact fluorescent (purple), sodium (blue) and mercury vapor (green) lamps as well as different LEDs (yellow, orange, and red).[16, 17] Correlated color temperaure (CCT) is indicated on the right side of the plots. (c) Downwelling spectra irradiance as a function of water depth at geographical latitude 46.0053° and longitude -8.1543° between Majorca and Algeria.[18, 19] (d) Example of spectra resulting from a low-wavelength-pass tunable filter useful for RAINBOW solar cells characterization.

The standard and more used characterization procedure in PV is the measurement of the power conversion efficiency (PCE) under 1 Sun illumination (the standard terrestrial AM1.5G broad-band spectrum).[20, 21] Another essential characterization is the external quantum efficiency (EQE), which provides information on the photon-to-electron conversion effectiveness.[20] More advanced measurements are used to investigate solar cells besides PCE and EQE measurements. For instance, the dependence of the photocurrent and open circuit voltage with illumination intensity has been used to investigate different recombination mechanisms in organic [22, 23, 24] and hybrid-based photovoltaics.[25]

Currently, these measurements rely on the use of different filters and/or different light sources and/or different setups. Importantly, a recent attractive method to have a light source whose light spectrum

can be modified in shape and intensity is using an array of individually addressable light-emitting diodes (LEDs). These devices are particularly useful for producing different broad-band spectra (e.g. AM0 and AM1.5G) as well as different narrow-band spectra.[21, 26, 27] Having a single piece of equipment for testing many conditions is advantageous. However, LED illumination has several intrinsic limitations, such as poor spectral resolution. Typical systems have < 20 LEDs to cover a spectral range of more than 900 nm; therefore, the LEDs used for these devices have FWHMs of several tens of nanometers. Another problem is the non-linear response of LEDs with current, which strongly limits the dynamic range of the illumination source. The latter implies that LED-based solar simulators may not be well fitted for experiments requiring a large dynamic range (e.g., the recombination studies mentioned earlier) or to reproduce indoor illumination conditions unless a combination of (non-automatic) filters is used. Finally, it seems that the most critical aspect is that achieving spatial homogeneity for large areas is complex and expensive.

Regarding beam characteristics, all the discussed characterization techniques require the beam to be homogeneous in terms of intensity and spectrum, apart from stable over time. Therefore, the different light sources are set up to meet these criteria. One notable exception to this requirement is the mentioned multi-junction solar cells based on the spectrally split (RAINBOW) concept, which is the main focus of this thesis.[10] In this case, a spectrally split beam is required so each sub-cell can be illuminated with the appropriate fraction of the sun spectrum. Thus, a highly tunable setup is required to investigate and optimize this geometry.

With the latter being our primary motivation, we have developed a spectrum on-demand light Source (SOLS) capable of providing a tunable light spectrum, which can be spectrally shaped in intensity and/or wavelength range with respect to a primary light source. The distinctive features that differentiate the SOLS light source from the current state of the art are:

1. It offers two types of spectrally shaped output: A spatially homogeneous beam over its cross section with the demanded spectral shape, used for homogeneous areal illumination, and a spatially and spectrally split beam divided into different wavelength components, a unique capability for illuminating lateral-tandem (RAINBOW) solar cells.
2. It provides a high light throughput and a large spectral window (at least from 380 to 1100 nm) by implementing a dispersive optical element based on refraction instead of diffraction.

14 SPECTRUM ON DEMAND LIGHT SOURCE (SOLS)

3. It can output a highly tunable broad-band spectrum shaped to suit a large range of applications, e.g. AM1.5, AM0, indoors, building integrated PV, agrovoltaics, tunable low/high pass filter for spectral splitting PV, stability measurements, etc. At the same time, it can output narrow-band spectra with a broad tunability of the central wavelength and FWHM, suitable for EQE measurements, among others.
4. SOLS has a large intensity dynamic linear range (about two orders of magnitude) realizable without the need of optical density filters, which could compromise the broad-band spectral filtering uniformity. The intrinsic linearity dependence and its wide dynamic range lead to a much simpler and less time-consuming procedure to spectrally shape the output spectrum, as compared to LED solar simulators.
5. First implementation of SOLS already exhibits excellent temporal stability in terms of intensity and spectrum (e.g., <2%, type A solar simulator) and fairly good spatial (e.g., <5%, type B) and spectral (e.g., <2%, type A) homogeneity over the output illuminated area.

Hence, SOLS offers great versatility with the mentioned features, such that it can be used to test different PV properties like PCE, EQE, efficiency under specific illumination conditions, tandem optimization, automatic light intensity scans, etc., adapting simultaneously the output spectrum to match the illumination requirements of a particular application.

3.2 SOLS SETUP EMBODIMENT

This subsection describes the working principles of the SOLS and focuses on the actual embodiment of the setup. [Figure 3.2](#) shows a sketch and a photograph of the actual SOLS setup. We can divide the underlying concept for the proposed setup into three main blocks. In the first block (green in [Figure 3.2](#)), white light coming from a broad-band lamp is dispersed into its constitutive wavelengths with a dispersive optical element. The choice of optical element is discussed later in the section. After this stage, the light beam is spectrally split into its composing wavelengths in the direction perpendicular to light propagation.

A second block (blue in [Figure 3.2](#)) is placed in the beam's path to partially mask it, controlling the transmitted light at each wavelength. This block is the part of the SOLS that shapes the output spectrum, being able to produce any spectrum by subtraction of the original

light. We have implemented two different masking systems in the SOLS setup, which will be discussed afterward. Implementing other masking systems is also discussed for a future upgrade of the setup.

Finally, a third block (red in Figure 3.2) is responsible for reconcentrating the spectrally split beam. At any point during this path, the beam light is spectrally split. To our knowledge, the latter is a novel feature not present in any setup available on the market. Nevertheless, for most of the applications, a homogeneous spot is needed. For this reason, some optical elements can be added at the focal point of the spectrally split beam to spatially and spectrally homogenize the light beam. Additionally, the output light has to be characterized in terms of its power and spectrum to quantify the effect of the masking systems and the overall setup. Unless specified, all spectra and output characterization shown in this chapter are measured at position (6) of Figure 3.2. The latter also applies to SOLS spectrum shown throughout the whole thesis.

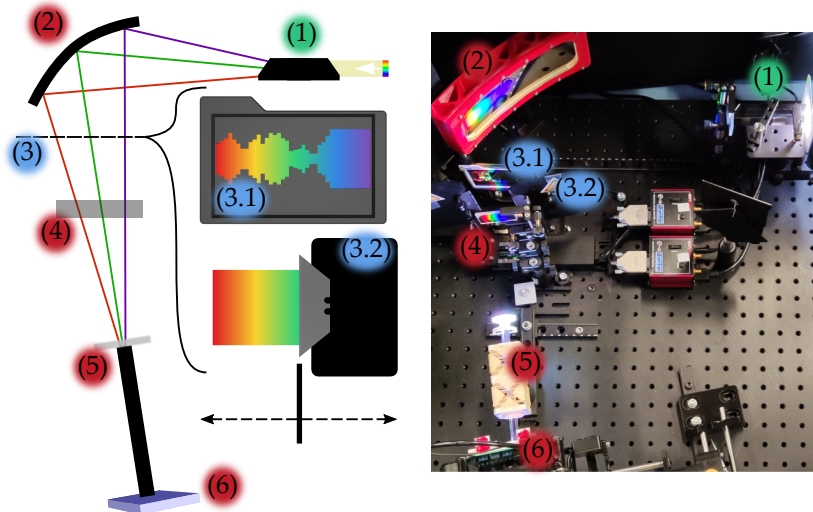


Figure 3.2: SOLS setup schematics. (a) Schematic of the SOLS setup. (b) Photograph of the actual SOLS setup. The main parts composing the setup are labeled as (1) double Amici prism, (2) custom mirror to concentrate spectrally split light, (3) masking plane (3.1) 3D-printed mask (3.2) motorized guillotines, (4) cylindrical lens to concentrate light in the vertical direction, (5) light pipe homogenizer, and (6) light output and cell holder. The three main blocks are differentiated with green (dispersive element), blue (filtering elements), and red (reconcentration and homogenizing elements) background in the numbering.

3.2.1 Dispersive element

Dispersive optical elements based on a combination of diffraction and refraction have advanced functionalities. Nevertheless, they are unsuitable for this setup

A dispersive element is an optical element that physically separates an input light, typically broad-band, into its composing wavelengths (colors). The latter can be done thanks to diffraction and/or refraction of light. Diffraction-based dispersive elements generally have better light separation than refractive-based ones due to a higher wavelength resolution and a more homogeneous dispersion dependence on wavelength. Nevertheless, their optical window is limited due to overlapping multiple diffraction orders of different wavelengths. Additionally, the latter is a source of light loss, reducing light output. Although modern monochromators use diffractive gratings as dispersive elements, their disadvantages are incompatible with the SOLS application. The overlapping of diffraction orders of different wavelengths limits the spectral range of operation of the device: the ratio between the maximum and the minimum wavelengths has to be between 1 and 2. For example, suppose the maximum wavelength that we want to achieve is 1000 nm. The second dispersion order of 500 nm will appear in the same direction as the first diffraction order of 1000 nm, limiting the spectral range between 500 and 1000 nm. Additionally, the diffraction efficiency has a strong wavelength dependence, drastically dropping for wavelengths far from the wavelength at which the grating is optimized. The latter reduces the light output and strongly impacts the spectral shape of the diffracted light. On the other hand, refraction-based dispersive elements have no spectral limitations except from the transparency range of the materials composing the optical element. Since these are typically optical-grade SiO₂ (fused silica and similar optical glasses), their operation range is approximately 300 nm to 3 μm. Additionally, the transparency in that range is near 100%, and the main losses are due to reflection at the interfaces. Although *a-priori* refraction-based dispersive elements have a worst dispersion because they heavily rely on the dispersion of the refractive index, they can be designed to satisfy a wide range of applications.[28, 29, 30]

Refraction-based dispersive elements typically are geometrical blocs of glass, thus referred to as prisms.

The discussed advantages and disadvantages between diffraction and refraction-based dispersive elements resulted in the choice of refraction-based for the SOLS equipment. Among all possible dispersive prisms, we choose the double Amici prism as the dispersive element.[31, 32] The double Amici prism consists of three triangular prisms in contact, with the first and the last typically being made from a medium-dispersion crown glass and the middle one made from a higher-dispersion flint glass (see [Figure 3.3](#) (a)). The main advantage of the double Amici prism compared to other types of dispersive prisms is that a certain wavelength of the incoming beam (≈ 550 nm for our prism) remains in the optical axis of the input light, facilitating the geometric design

of optical setups.[33] This prism can be optimized and designed to achieve dispersion comparable to gratings.[28, 30]

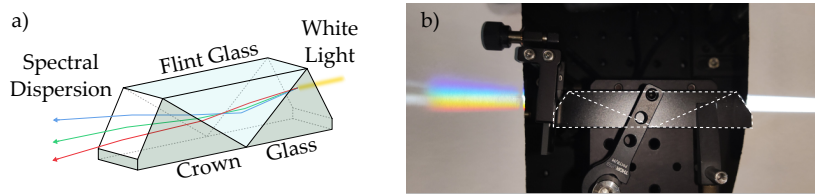


Figure 3.3: White light dispersion in a double Amici Prism. (a) Schematics of the geometry of the double Amici prism and (b) photograph of the double Amici prism used in the SOLS setup with the three different glass slabs marked with dashed white lines.

In our implementation, the light source is a Xenon arc lamp (150 W). In general, it can be any (broad-band) light source; nevertheless, some aspects have to be considered for a better light separation (i.e. wavelength resolution). The incoming beam should be as collimated as possible since any degree of divergence or convergence of the input light will result in different incoming light angles and, therefore, different exit angles for the same wavelength, resulting in a poorer color separation. The width of the incoming light beam also affects the latter since a wider collimated input light will result in a wider spatial distribution of the same wavelength that exits the prism with the same angle. We had to improve the collimation of the Xenon arc lamp before the double Amici prism to increase wavelength resolution at the expense of light power. The latter is further discussed in the last section of this chapter. The actual implementation of the double Amici prism with the corresponding input light source can be seen in [Figure 3.3](#) (b). The photograph shows the dispersion introduced by the prism to the broad-band input light (right side), which produces the rainbow pattern observed at the output of the prism (left side).

3.2.2 Filtering element: 3D-printed masking cards

The second block (blue in [Figure 3.2](#)) corresponds to the filtering elements placed in the beam's path where the beam is spectrally separated. These filtering elements are crucial components that enable simple and versatile spectral shaping. For demonstration, we have implemented the use of 3D-printed "cards" (element (3.1) in [Figure 3.2](#)), such that by insertion of a card with a given slit-height versus wavelength profile, a predefined spectrum is obtained. The shadow mask encodes the intensity-wavelength information in the form of slit height as a function

of lateral position as shown in [Figure 3.4](#).

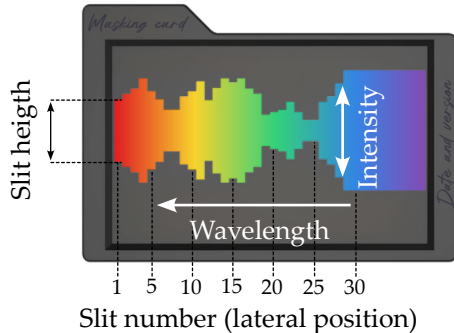


Figure 3.4: 3D-printed masking card schematics. Example of the design of a 3D-printed masking card wherein the lateral position is discretized as slit number, and the height of each slit tune the light intensity transmitted.

The plane where the mask element is placed can be defined by two orthogonal directions, the one in which light becomes spectrally separated (wavelength) and the direction corresponding to the actual size of the light beam (intensity), as depicted in [Figure 3.4](#). This plane contains a continuous distribution of wavelengths along the wavelength direction. Nevertheless, for simplification, one can discretize this distribution by considering a set of N contiguous vertical slits equally distributed along the wavelength direction. The slits correspond to masks that transmit light along the intensity direction but only in a defined wavelength range. In our case, we implemented a total of 40 slits of 2 mm width, adopting consecutive positions throughout the wavelength direction. [Figure 3.5 \(a\)](#) shows a photograph of four consecutive vertical slits; while [Figure 3.5 \(b\)](#) shows the color resulting from other four slits when placed into the SOLS setup. During the thesis, I have experimented colors that I had never seen before. Unfortunately, the difficulty of capturing them in a photograph makes the endless possibilities of output colors a unique beauty of the setup in live.

The spectrum that emerges from each vertical slit, $\varphi_i(\lambda)$ measured at the sample position, can be used as basis vectors for expressing any spectrum as a linear combination of the latter, with coefficients, a_i , ranging from 0 to 1.

$$\theta_{\text{calc}} = \begin{bmatrix} a_1 & \dots & a_i & \dots & a_N \end{bmatrix} \cdot \begin{bmatrix} \varphi_1(\lambda) \\ \vdots \\ \varphi_i(\lambda) \\ \vdots \\ \varphi_N(\lambda) \end{bmatrix} = \vec{a} \cdot \vec{\varphi}(\lambda) \quad (3.1)$$

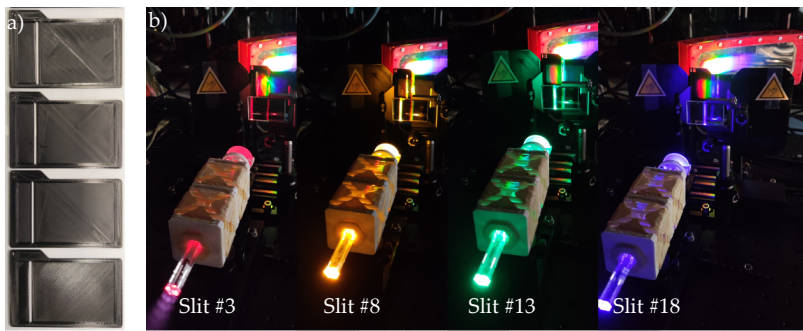


Figure 3.5: Examples of the slits system for the calibration of 3D-printed masks. (a) 3D-printed slits of the slits mask system from slit number 6 (bottom) to slit number 9 (top), wherein the complementarity of the slits is apparent. (b) Photograph of different slits acting as a unique mask system in the SOLS setup. The different colors show the SOLS's ability to act as a monochromator.

Figure 3.6 shows a set of slits spectra used for the calibration of the 3D-printed masking cards. Although the plane is discretized with 40 slits, the spectrally split beam does not pass through all of them because its width is smaller than the width of all 40 slits, resulting in a null spectrum for some of the slits at the extremes. Their position is maintained fixed with respect to the other parts, therefore small changes in light directions due to re-calibrations or movements of other parts of the setup results in a change of the slits spectrum. In this case, the actual vector basis is reduced to about 26 spectra. Assuming that each slit spectrum is uniformly distributed along the intensity direction, the a_i coefficients (\vec{a}) correspond to the relative height of each slit in the intensity direction. The latter is a reasonable assumption for a homogeneous and collimated beam incident at the entrance of the double Amici prism since the dispersive element does not affect the vertical direction of the rays that pass through it. A Python code can rapidly find the coefficients vector \vec{a} , looking for the linear combination that better fits a target spectrum. The latter is done using a minimization function (`Scipy.optimize.minimize`) from the `scipy` package.[34, 35] The integrated spectral difference between the fitted and the target spectrum is the function to minimize and \vec{a} is the vector parameter to fit. Afterward, the coefficients are introduced

Since the SOLS has been evolving during the thesis, slits-related data may correspond to different setup stages (i.e. different recalibrations)

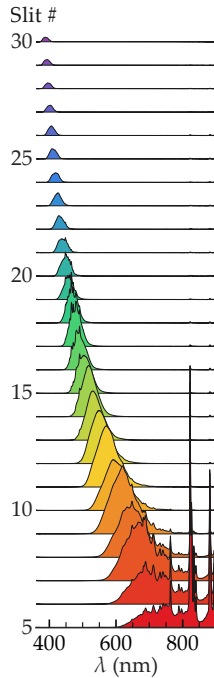


Figure 3.6: Spectra basis vectors for 3D-printed masks. Series of spectra from vertical slits used as basis vectors to calibrate the 3D-printed masks.

$\vec{1}_N$ is a vector of length N containing ones:

$$\begin{bmatrix} 1 & \dots & 1 & \dots & 1 \end{bmatrix}$$

in a parametric 3D design of the masking card, resulting in a model for 3D printing that matches the target spectrum.

If the slits were complementary and the light distribution along the intensity direction was homogeneous, the designed mask should result in the exact calculated spectrum. Nevertheless, this is not the case in the actual SOLS setup. The distribution along the intensity direction is not homogeneous but more concentrated in the central part. The latter is shown in [Figure 3.7 \(a\)](#), wherein slit spectrum was measured as a function of slit height. The measured spectra were integrated along the slit peak, and its total power density, normalized with the full slit spectrum, is plotted as a function of the slit height. The latter is decreased linearly for slits in the blue (425 nm), green/yellow (550 nm), red (650 nm) and infrared (900 nm) regions of the spectrum. The experimental points fall slightly above the expected trend for an ideal homogeneous distribution, indicating that light is not entirely homogeneously distributed along the intensity direction, being more concentrated in the central region. Moreover, [Figure 3.7 \(b\)](#) shows that the linear combination with $\vec{a} = \vec{1}_N$ for all slits (solid line) results in a spectrum lower than the measured spectrum without masks (dashed line). The combination of both effects results in the measured spectrum being slightly different than the calculated for a masking card. Therefore, a few extra optimization steps were needed to fabricate a masking card for each target spectrum.

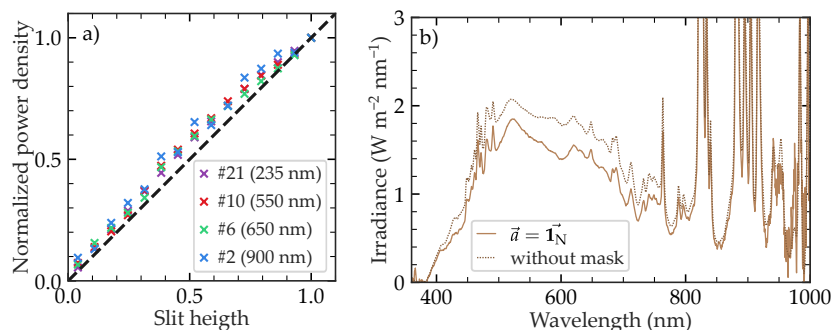


Figure 3.7: Slits calibration system imperfections (a) Power density transmitted as a function of slit height for slits at different spectral regions (central wavelength indicated in brackets). The ideal homogeneous distribution (grey dotted line) is also plotted for comparison. (b) Spectrum measured without a mask (dashed line) and spectrum resulting from the linear combination with $\vec{a} = \vec{1}_N$ (solid line).

For demonstration, [Figure 3.8](#) shows four examples of different target spectra (solid lines) and their corresponding SOLS output spectra (shaded curves). The first targeted spectrum ([Figure 3.10 \(a\)](#)) corresponds to the AM1.5G. It can be seen that the SOLS output spectrum

[Table 3.2 of Section 3.3.2](#) shows the spectral match evaluation of all spectra shown in [Figure 3.8](#)

closely reproduces the target spectrum. The latter is evaluated in [Table 3.2](#) of [Section 3.3.2](#), resulting in a Class A qualification between 400 and 1000 nm. Therefore, the SOLS is suitable for standard PV characterization under 1 Sun illumination. To confirm the good spectral match, we used three different OPV systems with energy band-gaps across the visible spectrum as a reference. We measured their efficiency with SOLS using the AM1.5G mask and with a commercial AAA solar simulator based on a xenon arc lamp. [Figure 3.10](#) (a) show less than 5% difference for each measurement, corroborating the good spectral match.

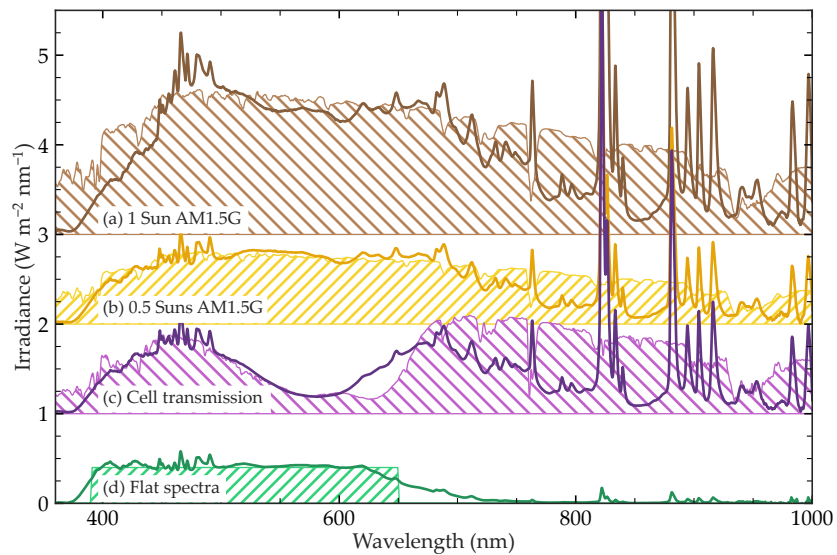


Figure 3.8: Spectra from 3D-printed masking cards examples Example of four different target spectra (filled area) and their corresponding SOLS output spectra (solid line) made with the slits calibration system. The physical masks that encode each spectrum are shown in [Figure 3.9](#), while their spectral match evaluation can be found at [Table 3.2](#).

[Figure 3.8](#) (b) corresponds to the 0.5 Sun AM1.5G spectrum exhibiting a Class A qualification as well, between 400 and 1000 nm (see [Table 3.2](#)). It demonstrates the setup's ability to perform light intensity-dependent PV characterization. By scaling the slit height profile of a mask card but maintaining the same spectral shape, the integrated spectral intensity can be substantially varied at least two orders of magnitude, as also shown in [Figure 3.7](#) (a). Thus, the dynamic range of the SOLS is larger than that of currently available spectral shaping alternatives, like the LED-based solar simulator, enabling the study of light intensity-dependent phenomena in greater detail. Additionally, it has a linear dependence on slit height, which facilitates the 3D-printed mask design procedure. For example, this feature would be handy for studying the

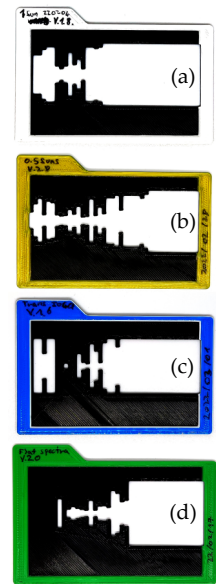


Figure 3.9: Masking cards encoding the fitted spectra from Figure 3.8. The 3D-printed masks were designed using the fitting procedure explained in this section.

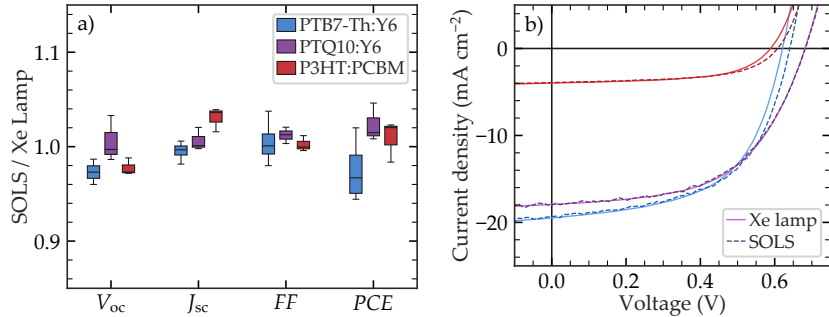


Figure 3.10: Comparison of OPV performance under 1 Sun measured with SOLS and with Xenon arc lamp solar simulator. (a) Statistical comparison between SOLS and Xenon lamp J-V measurements. (b) J-V curves of single organic solar cell measured with SOLS (dashed) and standard Xenon arc lamp (solid). Each box plot comprises four cells with different thicknesses and overall PCE.

nature of recombination processes in the photoactive layer, which requires measuring multiple J-V curves with a range of light intensities while maintaining the same spectral shape.

The SOLS is not limited to uniform intensity variations. By varying the relative intensity of each wavelength component, we can emulate the transmission spectrum of semitransparent solar cells, which can be an interesting feature in the thickness and blend composition optimization of tandem PV. For example, in Figure 3.8 (c), we emulate the transmission spectrum of a thin PBDBT-2F:IO-4Cl organic solar cell, which would act as the tandem top cell, with a band gap around 700 nm. With this “filtered” transmission spectrum, one can study the performance of multiple bottom cells before manufacturing the actual tandem device.

Besides simulating the pure or “filtered” solar spectrum, the SOLS is capable of producing entirely custom-shaped spectra, like the one shown in Figure 3.8 (d) (green curve), which targets a top-hat flat spectrum with an intensity of $0.4 \text{ W m}^{-2} \text{ nm}^{-1}$, between 400 and 650 nm, and $0 \text{ W m}^{-2} \text{ nm}^{-1}$ in every other wavelength. The resulting SOLS spectrum is also Class A within the relevant wavelength range, fitting the target spectrum quite well (see also Table 3.2). This custom output spectra capability expands the possible applications of the SOLS beyond PV characterization. As an example, these custom spectra could be used for calibration purposes that require a flat spectrum.

An important part of the versatility of this filtering element relies on the use of 3D printing. This introduces some limitations which are directly related to the intrinsic properties of this fabrication technique.

Fused deposition modeling (FDM) 3D printing has resolutions on the order of a few hundred of μm in the plane where slits are created. This resolution is more than enough for the vast majority of applications. For example, the slits of the vertical slits system are 2 mm in width and 50 mm in height. And typical values for slit height in [Figure 3.5](#) varies between 50 mm and 10 mm. Therefore, for most of the applications, the resolution of FDM 3D printing is enough. Nevertheless, if one wants to reproduce spectra comprising vertical slit height below 1 mm (corresponding to a relative slit height of 0.02), some problems may occur due to the 3D printing process. Then, the solution may require the fabrication of the mask with other methods such as printing the mask in black ink on transparent plastic film or using CNC machinery of metals. Another solution could be the use of optical elements (such as filters) to reduce the light intensity and therefore increase the relative slit height needed. Nevertheless, we have not found these resolution problems and the use of 3D printing was the easiest choice in this case. Nevertheless, another limitation is related to time, since 3D-printing a mask is far from an automated process. This could be mitigated with automated systems, as discussed in the last section of this chapter.

which is it can be reduced (or distorted) at the edges

. This resolution is more than enough for the lateral dimensions of slits. The latter is also true for

3.2.3 Filtering element: guillotines

As a part of the second block, we have introduced a partial automatization of the filtering process for more advanced experiments. This is a motorized filtering stage composed of two guillotines. Each guillotine masks the spectrum entirely above or below a given wavelength, producing the function of a tunable high-pass or low-pass filter. [Figure 3.11](#) shows the blue guillotine acting as a high wavelength pass filter (i.e. performing a red sweep) as an example. These filtering elements are designed to characterize and optimize solar cells in spectral-splitting multijunction geometries.

In order to perform these measurements, a previous calibration needs to be done. The calibration aims to determine mathematically the effect of each guillotine on the output spectrum by associating the position of the guillotine with a mathematical function. For this reason, we first modeled the masking effect of the blue guillotine masking the blue fraction of the spectrum on the spectral shape when performing a red sweep. For each position of the guillotine motor, the measured

Additionally, the combined effect of both guillotines corresponds to a band-pass filter which can be tuned in width and central wavelength.

The blue guillotine masks the blue fraction of the spectrum. Therefore, it generates a red sweep because the resulting spectrum contains the red fraction.

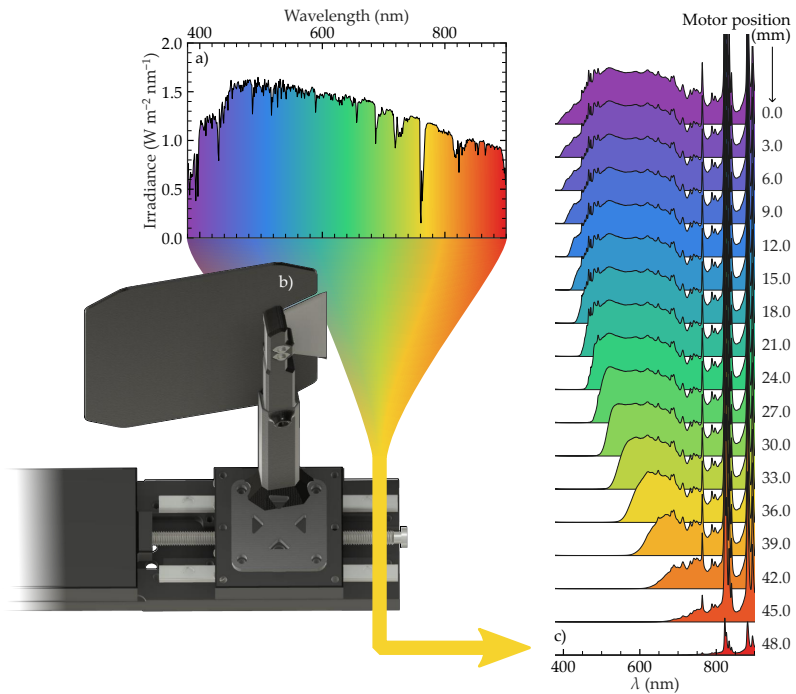


Figure 3.11: Schematics of the motorized blue guillotine (a) Solar spectrum spectrally split at the masking plane. (b) Motorized blue guillotine masking the blue fraction of the spectrum. (c) Individual spectra resulting from the movement of the blue guillotine (red sweep), which acts as a high wavelength pass filter. This set of spectra is used to calibrate the motor positions.

spectrum φ_{out} is divided by the full spectrum φ_{TOT} and the resulting ratio is fitted with an edge function $H(\lambda)$, following:

$$\frac{\varphi_{\text{out}}(\lambda)}{\varphi_{\text{TOT}}} = H(\lambda) \quad (3.2)$$

The edge function is a step function given by the Fermi-Dirac distribution (Equation 3.3), where h is the height, λ_d is the edge central wavelength and FWHM is the full width at half maximum of the edge:

$$H(\lambda) = \frac{h}{1 + e^{\frac{\lambda_d - \lambda}{\text{FWHM}}}} \quad (3.3)$$

Notice that the first derivative of the Fermi-Dirac distribution is symmetric with respect to the central wavelength λ_d . Nevertheless, due to the non-linear dispersion of the double Amici prism, the first derivative of the measured spectrum when a guillotine is acting as a filter is not totally symmetric. Nevertheless, this effect is very small in most of the spectral range, and the Fermi-Dirac distribution is enough

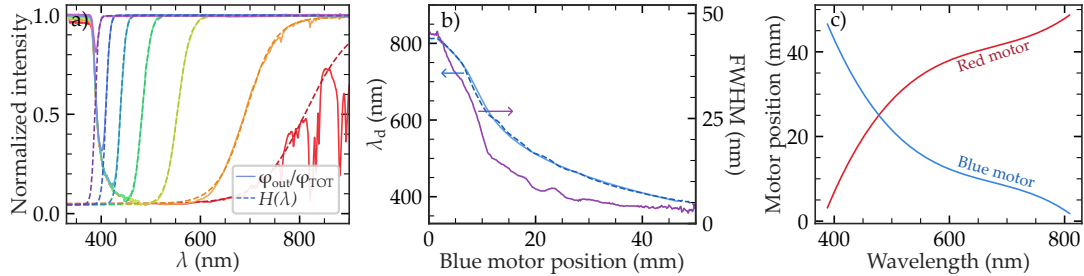


Figure 3.12: Results of the motorized guillotines calibration (a) A few examples of fitting the H function to the red-sweep data. (b) λ_d and FWHM as a function of the blue motor position resulting from the 250 spectra fitted. (c) The final calibration result shows the relation between motor position and dividing wavelength for the red and the blue motors.

to describe the effect of the guillotines. Figure 3.12 (a) show three examples of the described and in all cases except for the red line corresponding to λ_d in the IR region, the fit is close to the spectrum.

The dependence of λ_d and FWHM on the motor position for the blue guillotine is fitted to a spline to smooth the results. Figure 3.12 (b) shows the fitted λ_d and FWHM as a function of blue motor position. In order to calibrate the red motor position (i.e. the guillotine that performs the blue sweep), we search for the best complementary blue sweep spectrum for each red sweep spectrum. As a result, for each position of the blue motor, we have an associated λ_d and FWHM resulting from the fitting using Equation 3.3, and a red motor position with a complementary spectrum. λ_d is considered as the wavelength at which the spectrum is divided in the blue and the red part by the guillotines. For this reason, λ_d is named as dividing wavelength along the thesis.

In the scope of this thesis, the guillotines were used to characterize organic solar cells as sub-cells in a RAINBOW two-junction geometry, namely “blue” and “red” sub-cells with higher and lower bandgaps, respectively. Under AM1.5G illumination and in spectral splitting geometry, the red sub-cell receives the lower energy part of the solar spectrum, from ca. 1100 nm up to the dividing wavelength, λ_d . In contrast, the blue sub-cell receives the complementary part, i.e. between λ_d and 390 nm. The corresponding chapter (Chapter 4) explains all the experimental details of the RAINBOW characterization and results.

The third block of the setup (red in Figure 3.2) consists of an optical element that corrects the divergence applied by the prism to reconcentrate the spectrum (different colors) into a spot. The best and simplest option we found is a custom-made mirror, whose size and, most importantly,



Figure 3.14: Effect of the homogenizing apparatus. Spectrally split light beam entering the homogenizing apparatus through the diffuser (top image) and exiting the homogenizing apparatus through the light pipe (bottom image).

its curvature must be designed according to the output of the double Amici prism. Dr. Martí Gibert-Roca did the design and first fabrication of the custom-curvature mirror.[36] Besides considering the measured light divergence after the double Amici prism, the calculation also considers the distance that the spectrally split beam is forced to travel. The latter is to guarantee a correct spatial wavelength separation to attain the desired wavelength resolution. In our implementation, the distance between the prism and the curved mirror is designed to be about 30 cm. The mirror consists of a 3D-printed structure that provides the calculated curvature of an evaporated silver-coated 0.5 mm thick rectangular polyethylene terephthalate glycol-modified (PETG). The first two mirrors fabricated had the Ag exposed to air. The latter resulted in a decrease in reflectivity over time, especially in the UV region. Appart from that, the degradation was obvious to the naked eye ([Figure 3.13 \(a\)](#)). Trying to protect the Ag surface with a 40 nm thick LiF film was insufficient to avoid degradation over time. Nevertheless, the Ag/PETG interface barely showed degradation, as seen in [Figure 3.13 \(b\)](#). For this reason, in the successive iteration (evaporated mirror shown in [Figure 3.13 \(c\)](#)), we inverted the PETG sheet to reflect the light at the Ag/PETG interface. In that configuration, the Ag is sandwiched between the PETG and the 3D-printed frame, decreasing its possibility of degrading. This modification increased the durability of the mirror. Nowadays, the mirror is about two years old, and we have not observed any decrease in reflectivity yet, nor is degradation visually noticeable ([Figure 3.13 \(d\)](#)).

The reconcentration applied by the custom 3D-printed mirror is in the horizontal direction (wavelength direction in [Figure 3.4](#)). In addition, a cylindrical lens concentrates the beam along the vertical direction (intensity direction in [Figure 3.4](#)) to provide a tight focus on the next optical element. The focal length matches the mirror's focus in the horizontal direction in order to be in focus simultaneously in both directions to ensure minimal light losses.

3.2.4 Reconcentrator and homogenizer

The equipment delivers a focused but spectrally split beam in the path and at the focal plane where light is concentrated (where element (5) is placed in [Figure 3.2](#)). The latter could be used to characterize a multi-junction RAINBOW solar cell by placing the device at the correct distance before or beyond that focal plane. Nevertheless, this has not been implemented yet in the SOLS. In all the reported experiments, a homogenizing apparatus is placed at the focal point of the mirror and the cylindrical lens. It consists of a diffusing element in front of

a homogenizing light pipe. In this way, the diffusing element introduces significant randomness in the direction of the incoming light. Together with the homogenizing light pipe, the output beam produces a homogeneous illumination area, both spectrally and intensity-wise. The latter is shown in [Figure 3.14](#). Moreover, an analysis of the non-homogeneity of the output is done in [Section 3.3.3](#), wherein the effect of the diffuser on the output homogeneity is also discussed. In our current implementation, the resulting illuminated area ((6) in [Figure 3.2](#)) is about 50 mm^2 (a 4 mm inner radius hexagon).

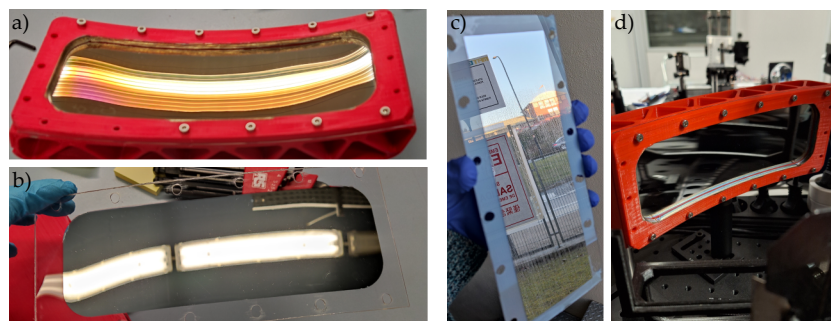


Figure 3.13: Degradation of the custom mirror Ag surface. Custom mirror showing degradation only in the Ag/air surface after approximately 6 months mounted on the SOLS from the front side (a) mounted on the 3D-printed frame, and from the rear side (b). (c) Mirror from the front side right after evaporation. (d) Show the same mirror mounted in the SOLS after 2 years (nowadays photo).

3.3 OUTPUT LIGHT CHARACTERIZATION

To use the SOLS as a solar simulator, we need to characterize its output following a standardized definition of a solar simulator. We chose the standard ASTM E-927 10, although other standards exist. This standard assesses the spectral match, the spatial non-uniformity of irradiance, and the temporal stability of the light produced by a light source that approximates the illumination of natural sunlight. A solar simulator gets a classification for each aspect, following [Table 3.1](#). The classification is Class A for the best scenario and Class C for the worst. Therefore, the classification of a solar simulator is defined by three letters. This section explains in detail the SOLS characterization according to the ASTM E-927 10 standards. But first of all, we need to explain the setup and methodology used to measure the output spectrum.

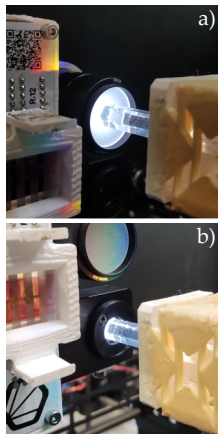


Figure 3.15: SOLS output spectrum measurement.
Photograph (a) Shows the measurement contraption while acquiring a spectrum, while photograph (b) shows a power measurement with the thermopile during calibration.

3.3.1 Measuring the output spectrum

In order to determine which is the spectrum delivered by the SOLS, we perform a direct measurement at the output of the light homogenizer. This corresponds to exchanging the sample at position (6) in [Figure 3.2](#) by the following contraption: a 1" tube containing a diffuser, a concentrator lens, and a glass fiber connected to a Flame spectrometer, as shown in [Figure 3.15](#) (a). Here, the purpose of the (second) diffuser is to make the measurement of the spectrum independent of the position of the tube with respect to the light pipe. The spectral response of the combined elements of the contraption, including the CCD and the Flame spectrometer, is unknown but, *a-priori*, not flat (i.e. it has an unknown dependence on wavelength). Hence, first of all, one needs to calibrate the contraption response. The calibration is performed by illuminating the contraption with an input light with a well-known irradiance spectrum, $E_{\text{ref}}(\lambda)$, which in our case corresponds to a LEDs solar simulator with a calibrated built-in spectrometer. By dividing

	Spectral Match*	Spatial non-uniformity SNU	Temporal instability TI
Class A	0.75-1.25	2 %	2 %
Class B	0.6-1.4	5 %	5 %
Class C	0.4-1.2	10 %	10 %

Table 3.1: Class A, B and C Standards and Specifications Defined by ASTM E 927-10.

* Acceptable range ratio of ideal % according to related table values for Ideal Spectral Match standards for ASTM E 927-10.

$E_{\text{ref}}(\lambda)$ by the Flame spectrometer data expressed in CCD counts for a certain integration time t_{int} , $\text{CCD}_{\text{cts}}^{t_{\text{int}}}(\lambda)$, we obtain the spectral response function, $k(\lambda)$; apart from a scaling factor, $A(t_{\text{int}})$, which only depends on t_{int} :

$$\frac{E_{\text{ref}}(\lambda)}{\text{CCD}_{\text{cts}}^{t_{\text{int}}}(\lambda)} = A(t_{\text{int}})k(\lambda) \quad (3.4)$$

The scaling factor $A(t_{\text{int}})$ is calculated only for 1 ms integration time since this is the limit of the Flame spectrometer, right below saturation for the AM1.5G spectrum. $A(t_{\text{int}})$ calculation is done by matching the power density integrated across the whole spectrum with that measured with a thermopile placed at the output of the light pipe (as in [Figure 3.15 \(b\)](#)) instead of the contraption for measuring the spectrum (as in [Figure 3.15 \(a\)](#)). [Figure 3.16 \(b\)](#) shows the product $A(t_{\text{int}})k(\lambda)$ resulting from the calibration. In principle, this calibration must be performed only once. Afterward, when a spectrum is measured with the contraption, we obtain the $\text{CCD}_{\text{cts}}^{t_{\text{int}}}(\lambda)$ spectrum ([Figure 3.16 \(a\)](#)). By applying [Equation 3.4](#) with the calibration curve, we can get the measured spectra in terms of irradiance ($E_{\text{out}}(\lambda)$), as in [Figure 3.16 \(c\)](#).

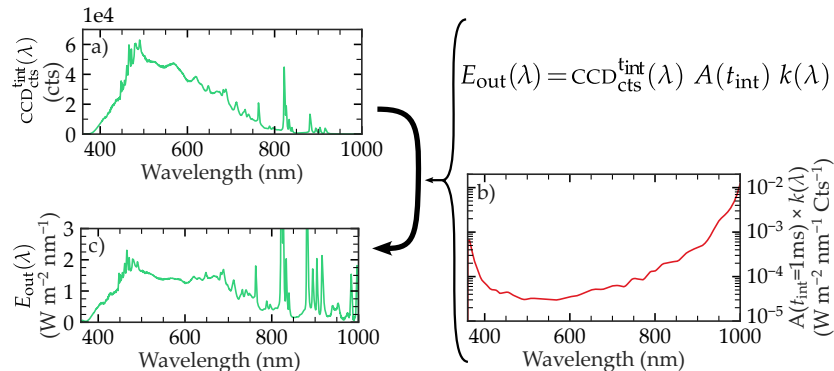


Figure 3.16: Workflow diagram for the measurement of a SOLS spectrum. In the first instance, a CCD cts. vs. wavelength spectrum is acquired (a). Using [Equation 3.4](#) and the calibrated $A(t_{\text{int}})k(\lambda)$ (b), the acquired spectrum is converted to irradiance vs. wavelength (c).

3.3.2 Spectral match

To assess the spectral match, we designed a 3D-printed masking card with the AM1.5G standard as target spectrum. [Figure 3.8 \(a\)](#) shows the target AM1.5G spectrum and the output spectrum of the SOLS achieved with the 3D-printed mask ([Figure 3.9 \(A\)](#)). The first row of [Table 3.2](#) shows the classification according to the ASTM standards.

The results indicate that the SOLS achieves a Class A between 400 and 1000 nm.

	400-500 nm	500-600 nm	600-700 nm	700-800 nm	800-900 nm	900-1000 nm
Spectrum A 1 Sun AM1.5G	Class A (-10.06 %)	Class A (-4.80 %)	Class A (1.80 %)	Class A (-21.16 %)	Class A (6.78 %)	Class A (-2.71 %)
Spectrum B 0.5 Sun AM1.5	Class A (-2.51 %)	Class A (3.65 %)	Class A (8.67 %)	Class A (-22.45 %)	Class A (-1.4 %)	Class A (-12.26 %)
Spectrum C Cell transmission	Class A (-0.51 %)	Class A (1.49 %)	Class C (52.12 %)	Class C (-44.38 %)	Class B (-25.34 %)	Class B (-32.65 %)
Spectrum D Flat spectrum	Class A (8.04 %)	Class A (4.93 %)	Class B (28.85 %)	*	*	*

Table 3.2: Classification following the ASTM E927-10 standards of the four spectra shown in Figure 3.8.

* Corresponds to spectra data which cannot be evaluated with the standards since the target spectra irradiance is 0, therefore the percentage difference cannot be calculated.

3.3.3 Spatial non-uniformity

For the measurement of the spatial non-uniformity (SNU), we mounted a 500 μm in diameter pinhole at the entrance of the spectra measuring contraption. This pinhole collects only a small part of the light that exits the homogenizing light pipe. Spectra was measured in front of the homogenizing light pipe in a grid of 10 by 9 pixels, every pixel of $1 \times 1 \text{ mm}^2$ in size. Because the output light spreads relatively fast, this measurement is very sensitive to the distance between the light pipe and the pinhole. Additionally, the small dimensions of the output light made it difficult to ensure parallelity between the light pipe output facet and the mesh measurement plane. As a result, the measurement had a gradient offset. The latter was corrected by fitting the data to an offset plane, which corrects for the non-parallelity between the light pipe output facet and the mesh measurement plane. Additionally, the scaling factor $A(t_{\text{int}})$ was corrected by the relation between the measuring area with and without pinhole.

SNU of a certain area is calculated considering the pixels with the maximum and the minimum power values (P_{\max} and P_{\min} respectively), and following:

$$\text{SNU}(\%) = 100 \frac{P_{\max} - P_{\min}}{P_{\max} + P_{\min}} \quad (3.5)$$

The resulting spatial power density distribution, Figure 3.17 (a), shows that the spatial non-uniformity is 4.16% in a large area over the central part enclosed by the yellow dashed line. It corresponds

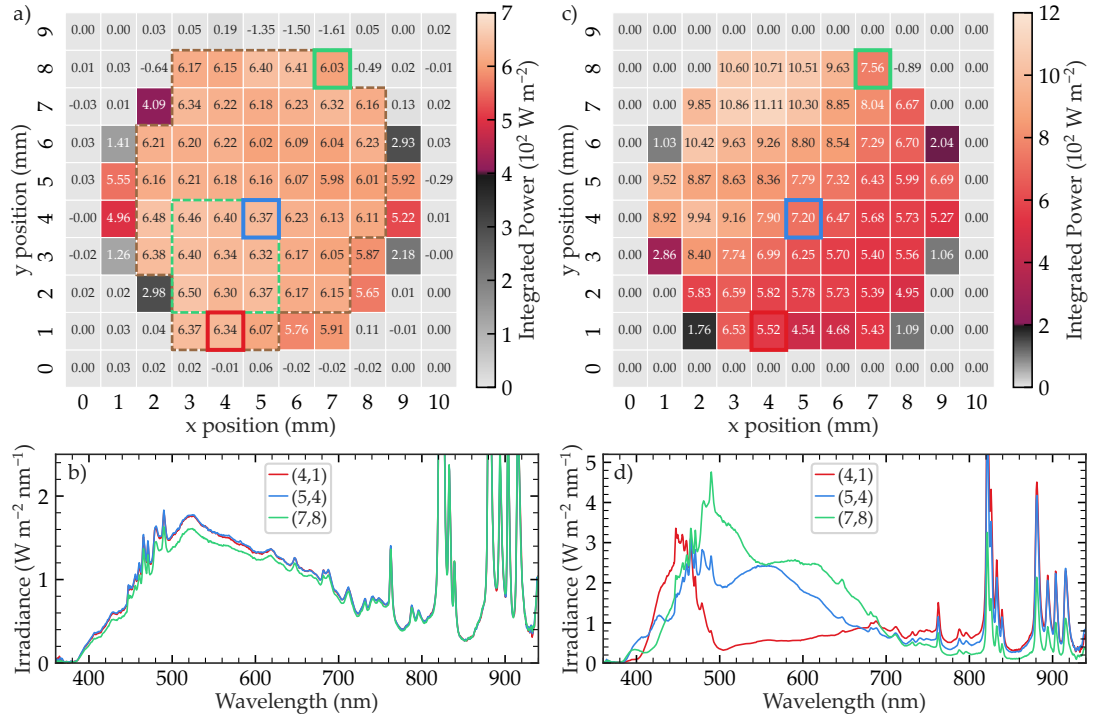


Figure 3.17: Spatial non-homogeneity classification. (a) Spatial distribution of SOLS output light plane with a 1 mm by 1 mm pixel grid. The dashed brown line encloses a large Class B region with 4.16% spatial non-uniformity, while the green dashed region has a 1.56% spatial non-uniformity corresponding to a Class A. The green, blue, and red solid squares highlight the pixels whose spectrum is shown in (b). (c) and (d) correspond to the same measurement and analysis performed respectively in (a) and (b) but without the diffuser element before the homogenizing light pipe. The lack of diffuser drastically affects the non-homogeneity of the output light.

to a Class B spatial non-uniformity according to ASTM standards. Nevertheless, if we consider a lower area, such as the one enclosed by the green dashed line, the non-uniformity can be reduced to 1.56%, achieving a region with Class A spatial non-uniformity. Figure 3.17 (b) shows the spectra from 3 different pixels, highlighted with solid lines in Figure 3.17 (a), to show that the spectral shape over the whole output plane is consistent. The former indicates that the small changes in the integrated power of Figure 3.17 (a) are mainly related to a change in the intensity of the spectrum rather than a change in its shape.

The same procedure was carried out without the initial diffuser to understand the diffuser's role in homogenizing the light output. It is worth mentioning that the difference is obvious to the eye, making the output much more homogeneous when using the diffuser. Additionally, the measurements showed higher intensity, indicating null losses due to scattered light before the homogenizing light pipe. The results

The diffuser which was taken out for this measurement is the one corresponding to the homogenizing apparatus shown in Figure 3.14

of this experiment are shown in [Figure 3.17](#) (c). In this case, the spatial distribution is less homogeneous than the case with the diffuser ([Figure 3.17](#) (a) and (b)). The differences are especially notorious when considering the spectra in different pixels, as shown in [Figure 3.17](#) (d). The different pixels show completely different spectral shapes when the diffuser is not used. Conversely (when the diffuser is used), spectral shapes are very similar. Finally, the spatial inhomogeneity classification is poorer than Class C for most of the area. Thus, the need for the diffuser is justified and mandatory when comparing the spatial distribution of the output light with ([Figure 3.17](#) (a) and (b)) and without ([Figure 3.17](#) (c) and (d)) the diffuser. Although it comes at the expense of light intensity.

3.3.4 Temporal instability

We expect the temporal instability of the setup to be defined by the temporal stability of the input light source since none of the SOLS parts is moving while a fixed spectrum is given at the output of the equipment. To verify this hypothesis, we have measured the temporal instability of the light entering the SOLS as well as its output light. To do that, the light power time dependence was measured with a silicon photodetector, and [Equation 3.6](#) was used to calculate the temporal instability. While JIS C and IEC standards differentiate between short-term and long-term temporal instability (STI and LTI respectively), ASTM standards do not. Nevertheless, it is useful to differentiate between short-term and long-term instability. In this case, we will be considering the measurement of I - V curves, which takes around 5 seconds. In that case, STI is understood as the temporal instability between data points in the same J - V curve. For STI, data was acquired every 10 ms for a total of 5 seconds. Analogously, LTI represents the temporal instability between different J - V curve measurements. In that case, LTI data was acquired every 1 second for 50 seconds. Analogous to spatial non-uniformity, STI or LTI are calculated taking into account the maximum and the minimum power measured for each data set (P_{\max} and P_{\min} respectively) and following:

$$\text{STI or LTI}(\%) = 100 \frac{P_{\max} - P_{\min}}{P_{\max} + P_{\min}} \quad (3.6)$$

The results in [Table 3.3](#) show that both input and output STI averages are statistically the same value, while, in the case of LTI, average values are statistically different, with the LTI of the output the smaller value. These observations indicate that the SOLS setup does not introduce temporal instability to the light source used, a xenon-arc lamp, confirming the starting hypothesis. We can also deduce from the results that with the light source employed in this embodiment, the temporal

Measurement	STI (%)		LTI (%)	
	Input	Output	Input	Output
1	0.73	0.88	0.30	0.22
2	0.88	0.81	0.38	0.20
3	0.69	0.62	0.28	0.27
4	0.80	0.56	0.31	0.24
5	0.78	0.88	0.39	0.21
Average	0.78 ± 0.07	0.75 ± 0.15	0.33 ± 0.05	0.23 ± 0.03

Table 3.3: Short-term instability (STI) and long-term instability (LTI) of the input and output light of the SOLS. 5 measurements were done for each situation and the average and standard deviation are shown in the last row.

stability is Class A according to ASTM standards since STI and LTI are significantly lower than 2%.

3.4 LIMITATIONS, CONCLUSIONS, AND OUTLOOK

3.4.1 Spectral resolution

The main advantage of SOLS with respect to other light sources is the spectrum customizability. This is strongly linked to the wavelength resolution, and thus to the wavelength distribution/separation along the masking plane wherein the filtering systems act. In order to distinguish between two wavelengths, their intensity distributions in that plane need to be sufficiently separated in the lateral (wavelength) direction. This is directly related to the way the dispersive element, the double Amici prism, separates the light.[28] In any refractive optical element, the separation between two adjacent wavelengths is determined by the difference in the deviation angles for the two wavelengths and the distance they travel. The former is governed by the wavelength variation of the refractive index (a.k.a. dispersion) of the two materials composing the double Amici prism. In the visible spectral range, and as a rule of thumb for any glass combination, this angle is higher for shorter wavelengths. Therefore, the wavelength resolution of the SOLS setup is higher in the blue than in the red part of the spectrum. The wavelength resolution or color separation can also be improved by increasing the distance between the prism and the mirror at the expense of increased equipment size.

Moreover, other factors directly impact the resolution, namely the degree of collimation (how paraxial the incident beam is) and the lateral extension (width) of the beam at the entrance of the double Amici prism. Ideally, if the input light is perfectly collimated and enters the prism

34 SPECTRUM ON DEMAND LIGHT SOURCE (SOLS)

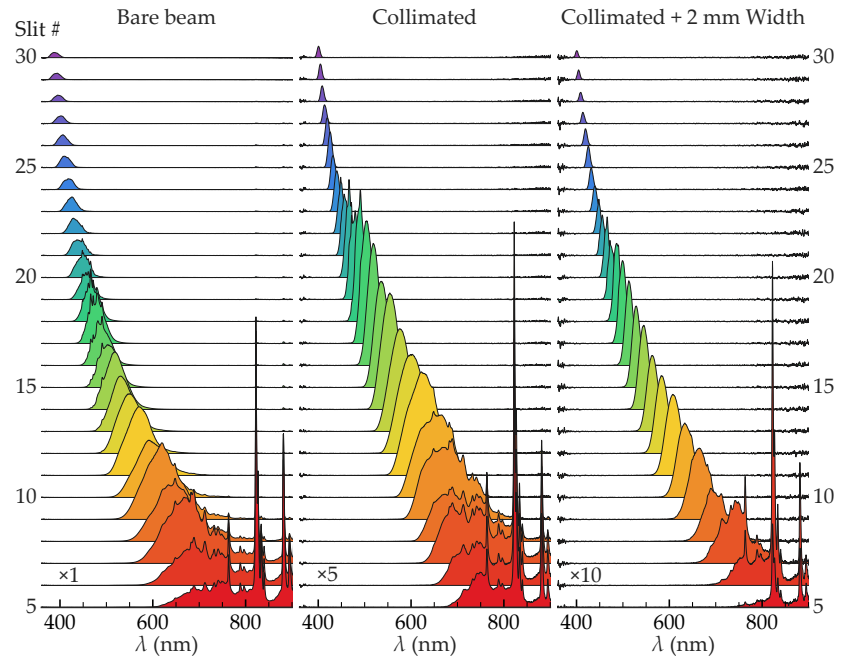


Figure 3.18: Effect of input light collimation and width reduction to wavelength resolution. Series of spectra corresponding to vertical slits used in Section 3.2.2 for different treatment of the light entering the double Amici prism: (a) bare beam, (b) collimated beam (middle panel) and (c) collimated and laterally-reduced beam width. Spectra from (b) and (c) is amplified by 5 and 10 times, respectively, with respect to spectra shown in (a) for clarity porpoises.

only in an infinitesimally thick vertical line, every photon with the same wavelength would have the same optical path through the prism, exiting throughout the same point and with the same angle. Thus, one would expect an infinitesimally narrow Gaussian peak for each wavelength, perfectly separated from the others. A departure from this ideal situation corresponds, for example, when light, though collimated, enters through a finite thickness slit. The resulting distribution is expected to be a sum of various Gaussian functions corresponding to each infinitesimal slit inside the slit width. In that situation, the different wavelengths overlap at a given position in space. In that case, wavelength resolution improves moving further from the prism. However, we have found that the effect of a poor collimation of the beam is still more critical. For example, if one focuses the beam at the entrance of the double Amici prism, there would be a distribution of incoming angles for photons with the same wavelength, and therefore, even if they enter the double Amici prism from exactly the same point, they would escape the prism with different angles. Therefore, one expects a broadening effect of the Gaussian distribution and a certain

degree of color mixing. In that case, the wavelength resolution does not necessarily improve far from the prism. Both effects are detrimental to the spectral resolution and are mainly dependent on the input light beam: the thinner and the more collimated it is, the better the color separation at the plane of the mask systems, thus improving the wavelength resolution. Nevertheless, the latter comes at the expense of light intensity.

As usual, there is a tradeoff between spectral resolution and the throughput of the SOLS setup. It is clear that if the primary light source is not properly collimated, whatever the optics used for its collimation, there will be a certain penalty in light intensity, which is even higher when a slit is placed in front of the prism. The latter can also be observed in [Figure 3.18](#), wherein the spectra from (b) and (c) were scaled 5 and 10 times, respectively.

The mentioned dependence in spectral resolution is best observed in the cascades of slit spectra shown in [Figure 3.18](#). The Figure displays the spectra resulting from consecutive 2 mm slits masks when the light enters the double Amici prism directly from the Xenon arc lamp (a), when it is collimated in between (b), and when apart from collimated it is also width reduced with a 2 mm width slit at the entrance of the double Amici prism (c). The data clearly shows that the resulting measured spectra are much narrower when collimation and width-reduction are implemented to the light entering the prism, showing a better wavelength resolution for the same slit width.

Each spectrum of [Figure 3.18](#) was normalized and fitted to a Split-Gaussian function. In this case, due to the observed non-symmetry

The Split-Gaussian is a Gaussian that has a different HWHM at each side of the central wavelength.

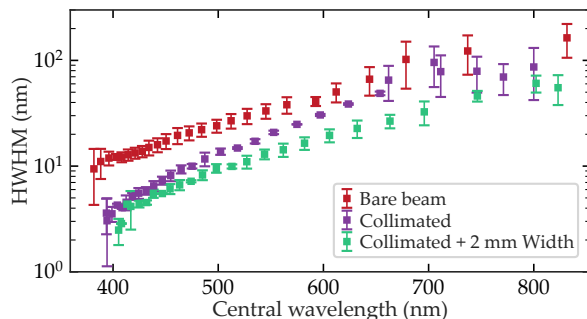


Figure 3.19: Half width at half maximum (HWHM) as a function of the central wavelength for the slit spectra shown in [Figure 3.18](#). The normalized slit spectra were fitted using a Split-Gaussian curve. The figure data squares shows the average of the two HWHM fitted values (which are shown as errorbars) as a function of the central wavelength for the three different light treatments.

of the slits spectra, we obtained a better fit with a Split-Gaussian. [Figure 3.19](#) shows the values of the fitted HWHM Split-Gaussian as a function of the central wavelength from spectra shown in [Figure 3.18](#). [Figure 3.19](#) demonstrates that collimating and width-reducing the light beam before the double Amici prism (green data points) improves up to 5 times the spectral resolution compared with the bare beam case (red data points), where light does not receive any treatment prior to being separated by the prism. When light is only collimated (blue data points), the spectral resolution is in between the other cases, being similar to the bare beam at the infrared region and similar to the collimated and width-reduced beam for the low wavelength region. This means that reducing the width is particularly effective at long wavelengths while collimation improves the resolution at short wavelengths.

3.4.2 External Quantum Efficiency

One of the capabilities of the SOLS setup, as mentioned in [Section 3.1](#), is to measure the photovoltaic external quantum efficiency (EQE_{PV}). Nevertheless, this functionality still needs improvement in terms of automatization, better analysis tools, and improved wavelength resolution in the infrared region in order to become a real part of a future SOLS prototype. Nevertheless, this subsection shows the potential of SOLS for measuring EQE_{PV} with different methodologies. EQE_{PV} is a common and useful characterization in photovoltaics that quantifies the spectral contribution to the short-circuit current density J_{sc} .[\[20\]](#) Mathematically, EQE_{PV} is related to J_{sc} as follows:

$$J_{sc} = \int \frac{\varphi(\lambda)}{E_{ph}(\lambda)} EQE_{PV}(\lambda) q d\lambda \quad (3.7)$$

Here, $\varphi(\lambda)$ is the spectral irradiance (in units of energy/second/area), $E_{ph}(\lambda)$ is the photon energy, and q is the electron charge. By dividing $\varphi(\lambda)$ by $E_{ph}(\lambda)$ we obtain the number of photo-generated electrons per unit time and area, which multiplied by the EQE_{PV} , the charge of an electron, and integrated over the entire spectrum yields the current density J_{sc} . The standard EQE_{PV} characterization involves the measurement of the photocurrent under narrow-band monochromatic wavelength illumination, typically in short-circuit conditions ($J_{sc, \lambda}$), for different central wavelengths in the range between 350 and 1100 nm.[\[20\]](#) Narrow-band illumination is typically obtained by spectrally filtering a broad-band source, for example using a monochromator. In that direction, the EQE_{PV} can be calculated for each narrow-band illumination condition as follows:

$$EQE_{\text{PV}}(\lambda) = \frac{\frac{J_{\text{sc}, \lambda}}{q}}{\frac{P_{\text{in}}}{E_{\text{ph}}}} \quad (3.8)$$

where P_{in} is the power of the monochromatic light reaching the device. [Equation 3.8](#) corresponds to the ratio between the number of collected electrons and the number of incoming photons at a given wavelength. The narrower the light source, i.e. the more monochromatic it is, the better the resolution of the EQE_{PV} . Notice that SOLS also includes a slit system, comprising a set of complementary slits masks of 2 mm each centered at different wavelengths (see [Figure 3.5](#) and [Figure 3.18](#)), with which SOLS transforms into a narrow-band tunable light source. In this case, the power density of the spectrum resulting from each slit (P_{in}) is measured with the thermopile ([Figure 3.15 \(b\)](#)) or by integrating the slit spectrum, and the wavelength is given by the central wavelength of each slit spectrum. [Figure 3.20](#) shows EQE_{PV} measurements made with the slit system of SOLS (slits- EQE_{PV} measurements) compared to those attained with our custom made EQE_{PV} rig, which includes a broad-band laser and a monochromator (blue curves). The results were obtained for OPVs with different E_{bg} . When light is collimated before entering the double Amici prism (purple data crosses in [Figure 3.20](#)), the slits- EQE_{PV} resolution is similar to that of the reference system in the spectral range between 400 and 600 nm approximately. For longer wavelengths, though, the wavelength resolution decreases drastically resulting in a broadening effect of the slits- EQE_{PV} . This can be improved by enhancing the wavelength resolution, for example, by collimating the input light of the double Amici prism and reducing its lateral (green data in [Figure 3.20](#)). Although wavelength resolution can still be improved in the infrared, in our current implementation the agreement between the slits- EQE_{PV} curves and those of the custom-made rig is excellent.

Interestingly, EQE_{PV} can also be extracted from a red or a blue sweep measurement using the motorized guillotines (like [Figure 3.11](#)). In this characterization mode, we can consider that the difference between measurements for two consecutive dividing wavelengths, λ_d , is analogous to a narrow-band measurement using a slit with a width equal to the spatial difference between the positions of the guillotine during the red or the blue sweep. The measurement proceeds as follows: first either a red or blue sweep is performed and the $J - V$ characteristics of the cell are recorded as a function of λ_d . From this set of data, one computes the solar cell figures of merit J_{sc} , V_{oc} , FF , and PCE as a function of λ_d . In analogy to a slit spectrum, $J_{\text{sc}, \lambda}$ of [Equation 3.8](#) is computed by taking the difference of the J_{sc} obtained for two consecutive λ_d . The corresponding (pseudo-slit) power density P_{in}

The tunable narrow-band source can also be achieved automatically with the synchronous movement of the motorized guillotines.

See [Section 3.4.1](#) for more details on spectral resolution of the SOLS

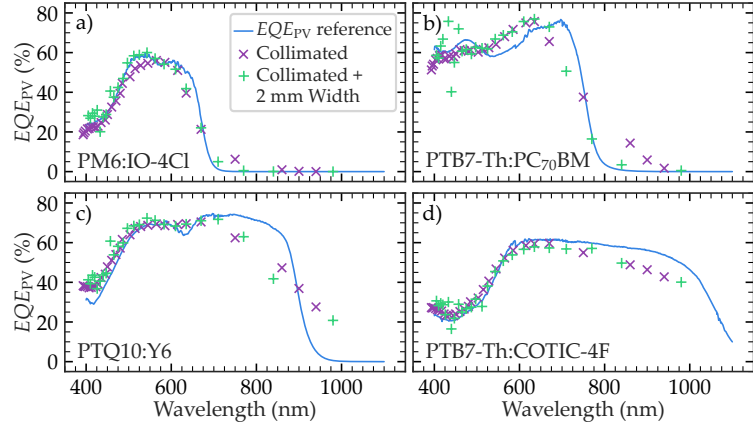


Figure 3.20: Slits-EQE_{PV} measurements with different input light treatments. Slit-EQE measurements with SOLS for collimated input light and collimated with lateral width reduced (purple and green data crosses, respectively) compared with results obtained with a standard white laser coupled to a monochromator (purple solid line).

is then obtained from a previous calibration of the incident spectrum, which consists in separately measuring the spectrum and the power density at each λ_d . This calibration is equipment-dependent and thus only needs to be performed once, saving valuable measurement time. Hereafter, the sweep-EQE_{PV} is computed using [Equation 3.8](#), as in the case of slits-EQE_{PV}. As can be appreciated in [Figure 3.21](#), the agreement between the sweep-EQE_{PV} obtained with the red sweep procedure and the more conventional monochromator-like mode with the slits system (slits-EQE_{PV}) is very good. The sweep-EQE_{PV} could also be obtained from a blue-sweep measurement since the pseudo-slit resulting from both sweeps is analogous.

Notice that, as far as we know, this methodology of measuring EQE from a red (or a blue) sweep is a unique capability of the SOLS setup.

3.4.3 Conclusions and outlook

In summary, we presented a novel spectral shaper illumination device with facile tunability, which can be used to perform standard photovoltaic tests like efficiency and EQE with the same equipment, thus helping to accelerate material screening. This enables the discovery and optimization of novel multi-component materials for emergent PV technologies like organic PV, metal halide perovskites PV, all oxides PV, kesterites, etc. The same equipment can also be used as a light source for more advanced characterizations requiring intensity-dependent PV characterization, which is the case for the study of recombination processes in photovoltaics. The SOLS also enables the development of many photovoltaic applications far from the standard sunlight harvesting, including agrivoltaics, indoor PV, building integrated PV

(windows, sunshades, etc.), semitransparent PV, etc.

One particularly attractive novel application of the SOLS light source is in the field of materials science for the development of multi-junction solar cells, both spectrally split as well as conventional tandem cells, aimed at highly efficient light-to-electricity conversion. This is the application for which the SOLS was initially intended. To the best of our knowledge, there is no other light source capable of addressing the full characterization (multi-junction and single sub-cell characterization) of multi-junction solar cells. In view of the fact that tandem and spectrally split solar cells can increase power conversion efficiency up to two to three times more than that of single-junction cells, this is a very promising implementation area of the SOLS system.[10, 11, 12, 13]

The combination of intensity and spectral tailoring capabilities offered by SOLS leads to novel characterization methodologies that could help to better understand charge generation and loss mechanisms inside solar cells, especially in the case of OPV, where at least two materials (donor and acceptor) are involved in the dynamics of the charge-generation process.

We now consider SOLS to be at TRL4 since we have proved all its capabilities in the lab. Nevertheless, in order to develop a product to transfer to the industry, we still need to improve some important aspects. One of them is the automatization. Currently, custom spectra done with the 3D-printed masks are far from automatic. In order to automatize the spectra tunability, we need to implement some masking elements that can change fast and in a controlled way. One

Technology readiness levels (TRLs) are a method for estimating the maturity of a technology from basic research to commercialization.

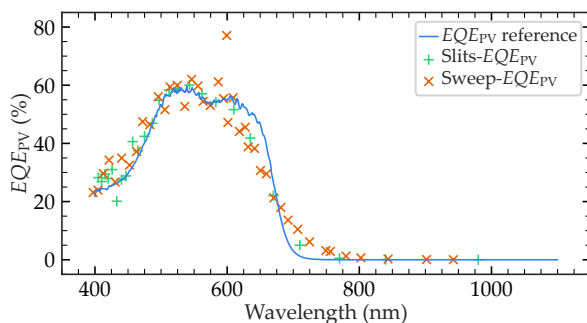


Figure 3.21: Sweep-EQE_{PV} measurement of a PM6:IO4-Cl solar cell. Sweep-EQE_{PV} of a PM6:IO4-Cl cell (same cell as Figure 3.20 (a)) calculated from a red sweep of a RAINBOW measurement (orange data crosses). The agreement with the reference EQE_{PV} measured with a white laser and a monochromator (blue curve) is very good, as well as with the slit-EQE_{PV} measurement with collimated and slit-reduced width (green data crosses).

40 SPECTRUM ON DEMAND LIGHT SOURCE (SOLS)

alternative is the use of liquid crystal displays (LCD). Nevertheless, the transmission of LCDs is typically poor (around 20% in the best scenario) and, therefore, would limit the equipment's intensity. Another option is the use of a digital micro-mirror display (DMD). The spatial resolution of DMD arrays is more than enough for our application (around $10 \times 10 \mu\text{m}^2$). Nevertheless, they are much smaller than the spectrally split beam, and their implementation requires optimizing the dispersive element.

The wavelength resolution is also an essential part of the equipment, and it may need improvement to find a niche in the market. The enormous impact of the input light's characteristics on the wavelength resolution is a bottleneck for the equipment. It implies the equipment's need for a specific light source, increasing its price. Nevertheless, we are working on these improvements. If we can find a solution for them, the commercialization of SOLS can help discover new materials and geometries in the PV field.

4

RAINBOW SOLAR CELLS

While multi-junction geometries have the potential to boost the efficiency of organic solar cells, the experimental gains yet obtained are still very modest. In this chapter we explore an alternative spectral splitting device concept in which various individual semiconducting junctions with cascading band gaps are laid side by side, thus the name RAINBOW. Each lateral sub-cell receives a fraction of the spectrum that closely matches the main absorption band of the given semiconductor. We first show the developed toolkit for the investigation of RAINBOW solar cells. Using the active layer blends PTB7-Th:COTIC-4F, PM6:Y6, and PM6:IO-4Cl as examples we show the agreement between a simple simulation model and two different characterization setups, the SOLS (described in [Chapter 3](#)) and a commercial LEDs solar simulator. With these examples we show that this geometry can lead to a reduction in thermalization losses and an improvement in light harvesting, which results in a relative improvement in efficiency of 46.6% with respect to the best sub-cell. Finally, a working proof of concept monolithic device consisting of two sub-cells deposited from solution on the same substrate is fabricated, thus demonstrating the feasibility and the potential of the RAINBOW solar cell concept.

4.1 INTRODUCTION

Single-junction solar cell efficiencies are limited by absorption and thermalization losses to a maximum theoretical efficiency of around 33%.[\[Ruhle2016TabulatedCells, Shockley1961DetailedCells\]](#) This limit arises from the spectral mismatch between the energy band-gap (E_{bg}) of the semiconducting junction and the solar spectrum; where photons with energies $E_{ph} < E_{bg}$ pass through the material unabsorbed (absorption losses) and photons with energies $E_{ph} > E_{bg}$ dissipate their excess energy as heat (thermalization losses). Both losses limit the theoretical maximum efficiency of a single-junction on a fundamental level.

So far, the most promising strategy to overcome this fundamental limitation consists of combining multiple junctions, with different E_{bg} , that attempt to match the energy of incoming photons, so to minimize thermalization and absorption losses.[\[Vos1980DetailedCells, Green2016CommercialPhotovoltaics\]](#) The latter are known as multi-junction solar cells. Up to date, the most common implementation of such multi-junction solar cells consists of vertically stacked devices. In

this configuration, the topmost junction absorbs the shortest wavelength range, while unabsorbed photons, with $E_{ph} < E_{bg}$, go through to the next sub-cell where this partial spectral absorption is repeated, resulting in a complementary absorption along the entire multi-junction stack (Figure 4.1 (a)).[Vos1980DetailedCells, Ameri2013HighlyReview, Werner2018Perovskite/SiliconAmeri2009OrganicReview, Yamaguchi2018ACells, Chen2017ProgressPerovskites, Biswas2020OrganicIllumination, Hossain2019Perovskite/SiliconManagement] This strategy yields a theoretical maximum efficiency, with infinite junctions, of 68% under AM1.5G illumination, and 86% with solar concentration, resulting in a promising alternative for large scale power generation.[Vos1980DetailedCells, Green2016CommercialPhotovoltaics]

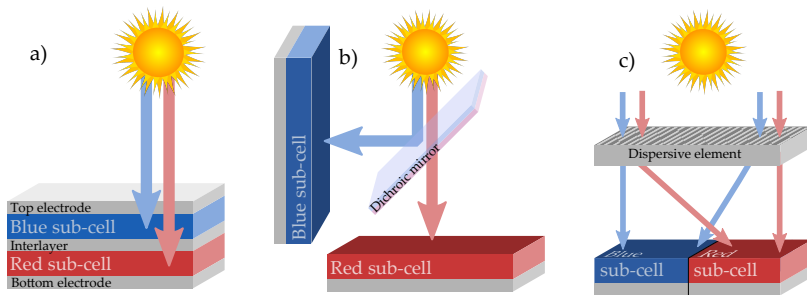


Figure 4.1: Schematics of different multi-junction geometries. Vertical (a), spectral splitting with a dichroic mirror (b), and RAINBOW in-plane configuration (c).

The catalog of organic semiconductors for photovoltaic applications has expanded greatly over the past decade leading to single-junction efficiencies above 19%. [DiCarloRasi2019AdvancesCells, Vos1980DetailedCells, Gao2022AchievingAcceptor, Wei2022BinaryDistribution, Cui2021SingleJunctionEfficiency, NREL2019PhotovoltaicChart] Despite the large material library available, with widely varying band gaps, organic multi-junction geometries have, thus far, shown modest success, not yielding more than a few percentages improvement over the best single-junction efficiency[37]. This is, in part, due to the difficulty to fabricate such geometries from solution[Gu2022OrganicProcess, Chen2020EfficientLayers] and further complicated by the need for current matching between sub-cells in two terminal devices,[Bonnet-Eymard2013OptimizedCells, Meusel2002SpectralCells] as well as the availability and implementation of transparent interconnecting layers (ICLs).

An alternative configuration for multi-junction cells is the spectral beam splitting geometry.[Mojiri2013SpectralReview, Mokri2010Beam-splittingElectricity:] This involves spectrally separating the solar spectrum and redirecting the spectral fractions to different sub-cells,[Lewis1997Multi-bandgapRAINBOW] as shown in Figure 4.1 (b). This approach has yielded promising

results in various systems, such as high efficiency III-V material multi-junctions,[Smith2000SolarConcentrator, Mitchell2011Four-junctionEfficiency] hybrid inorganic perovskite multi-junction solar cells,[Uzu2015HighSystem, Ferhati2021Perovskite/InGaAsStructure] as well as hybrid silicon thermal absorbers[Jiang2010OpticalTechnology, Liang2022AEnergy, Wang2019ThermodynamicTechnology] and thermoelectrics.[Omer2000DesignGeneration, Mahmoudinezhad2022ExperimentalConcentrations, Rockendorf1999PV-HYBRIDCOLLECTORS] Having physically separated cells makes fabrication simple, and sub-cell connection straightforward. The implementation of such systems has, however, proven to be rather cumbersome, as the most common configuration consists in placing each sub-cell at 90° , with a dichroic mirror at 45° spectrally redistributing sunlight, resulting in an awkward form factor that gets significantly more complex when increasing the junction count.[Mojiri2013SpectralReview]

In this work, we devise an alternative beam splitting configuration, consisting of a forward wavelength spreading element located over a horizontal stack multi-junction solar cell, so-called RAINBOW solar cell, as illustrated in [Figure 4.1](#) (c). The RAINBOW approach, being a monolithic in-plane manufacturing solution, can be based on deposition techniques that are considered already advanced.[Raupp2018SlotFluids, Shin2020EffectOLEDs, Parsekian2020ScalableApproach, Lee2020IncreasedOLEDs] On the other hand, the lateral distribution of each sub-cell allows for an easy implementation of electrically independent contacts, eliminating the need for current or voltage matching on a device level.[Mime2021DesignParameter, Etxebarria2015Solution-processable10] Additionally, a RAINBOW cell uses the same amount of material for electrodes, active layer, transport layers and substrate than a single junction cell, without significantly complicating production. Thus, the sustainability and cost of this architecture will be competitive, provided that the dispersive element can be manufactured easily, sustainably and cheaply. Finally, tandem solar cells show current losses due to spectral variations because of the current matching condition.[HaohuiLiu2017, MTHorantner2017, JRipalda2018] The latter is expected to reduce the efficiency limit to approximately 90% of the thermodynamic limit.[\[11\]](#) This restriction is expected to be less important in RAINBOW solar cells. Nevertheless, the need for optical elements introduces other restrictions, such as optical losses and geometry constraints.[\[11\]](#)

4.2 TOOLKIT FOR RAINBOW OPTIMIZATION

4.2.1 RAINBOW *concept*

The RAINBOW solar cell concept consists of two main parts: a light-dispersive element and a horizontal multi-junction array. The first, located above the multi-junction solar cell, spatially redistributes the solar spectrum into all its composing wavelengths. This combination results in a rainbow of colors, as shown in [Figure 4.1](#) (c), where each sub-cell is illuminated with the optimal wavelength range. The main advantage of the RAINBOW configuration relies on its ability to reduce both thermalization and absorption losses while avoiding the limitations of vertical stack manufacturing, such as defect accumulation and optical transparency loss,[[Etxebarria2015](#), [38](#), [11](#)] and the awkward form factor of other beam splitting geometries,[[AMokri2010](#), [13](#)] thanks to its planar lateral deposition configuration. While the RAINBOW geometry is not as simple as a single-junction device, in this novel configuration one can increase the number of sub-cells from two to N junctions without changing the form factor. Nevertheless, Peters et al., have already shown that the optimal number of junctions may be below ten juntcions[[11](#)]

The SOLS setup, shown in [Chapter 3](#), can potentially be the light-dispersive part of a RAINBOW solar cell configuration. Nevertheless, while it can be used for characterization, it is not optimal for this application. This is because an optical element with a big light input area is needed. Additionally, the double Amici prism is too big and heavy and does not have a high enough dispersion. Thus, one needs to consider other options for the light-dispersive optical element. The latter is not in the scope of this thesis, however, such elements have been previously reported, with multiple solutions available. For example, the dispersive lens proposed by Thio et al,[[SThiao2019](#)], the holographic solution proposed by Vorndran et al.[[SBondran2014](#)], or the the diffractive optical element proposed by Lin et. al.[[DFLin2016](#)] These solutions take advantage of a combination of diffraction and refraction of light to physically separate different fractions of the spectrum. The latter is not only applicable to RAINBOW solar cells but also to silicon photovoltaics for avoiding overheating of the modules due to IR radiation.[[SKiyae2021](#), [JXing2017](#), [13](#)]

This thesis focuses on the optimization of the horizontal multi-junction array throughout the choice of materials and the fabrication conditions of each sub-cell as well as the optimization of the spectral split light. We want to point out that the device used to achieve a

certain spectral split light is not in the scope of this thesis.

4.2.2 RAINBOW simulation model

One of the objectives of the thesis is to develop tools to facilitate the development of RAINBOW multi-junction geometries. For this reason, we first developed a simulation model to predict the RAINBOW performance considering the more important parameters:

DIVIDING WAVELENGTH In the simplest scenario, a RAINBOW configuration consists of two sub-cells. Thus, the optical splitting element divides the solar spectrum into two fractions: a “blue fraction” containing the shorter wavelengths, and a “red fraction” containing the longer wavelengths. These spectral fractions are redirected to each of the two sub-cells, which are consequently named “blue sub-cell” and “red sub-cell”, respectively (see Figure XXX). The performance of the RAINBOW device greatly depends on how the solar spectrum is divided. The wavelength at which the spectrum is divided is named "dividing wavelength" (λ_d). The latter defines the fraction of the spectrum that each sub-cell receives. Therefore, λ_d is one of the most important parameters to consider for the optimization of RAINBOW solar cells.

EXTERNAL QUANTUM EFFICIENCY The materials used in each sub-cell are also one of the key parameters. Their spectral photon-electron conversion response (i.e., the photovoltaic external quantum efficiency (EQE_{PV})) is key for the choice of materials. EQE_{PV} is a parameter that summarizes many processes happening in the solar cell such as photon absorption, exciton dissociation or free-charge conductivity to the contacts. Among all of them, the most relevant for the RAINBOW configuration is the photon absorption since it defines at which spectral region the EQE_{PV} will have its maximum. The choice of materials with certain EQE_{PV} spectra is key to reduce absorption losses.

J – V CHARACTERISTICS Finally, the FoM derived from the $J - V$ curve are key to predicting the RAINBOW efficiency. The V_{oc} is crucial because it is directly linked to the energy of the extracted electrons from each sub-cell, and subsequently, to the thermalization losses at the different sub-cells. The FF is important to reach high efficiencies. It has a dependence on active layer thickness and light intensity which is important to consider for the fine-tuning of the RAINBOW device. Finally, J_{sc} considers the number of extracted electrons, and consequently, is directly related to λ_d and EQE_{PV} .

4.2.2.1 Description of the simulation model

The simulation model focuses on the solar cells and their composing materials assuming lossless light redistribution of the spectral splitting optical element, and lossless DC-DC conversion of the electronic component converting the multiple-terminal device into a two-terminal solar cell. We are aware that those two assumptions may be far from reality. The spectral splitting element always has a certain white background (unsplit background light) and the spectral division may not be as sharp as desired. Furthermore, it is important to note that DC-DC converters consume power, with a higher consumption when the input voltages are closer to each other.

With these conditions, the RAINBOW efficiency (PCE_R) is calculated as the sum of the output electric power density of each sub-cell ($P_{out, cell}$) divided by the input power density of the AM1.5G spectrum ($P_{in} = 1000 \text{ W m}^{-2}$). The latter can be interpreted as a sum of the partial contribution of each sub-cell ($PCE_{p,cell}$) to the PCE_R as described by [Equation 4.1](#). Notice that, in this case, $PCE_{p,cell}$ is different from the power conversion efficiency of each sub-cell ($PCE_{p,cell} \neq PCE_{cell}$) since the input power density considered corresponds to the RAINBOW device and not to the power density each sub-cell receives.

$$PCE_R = \frac{\sum P_{out, i}}{P_{in}} = \sum \frac{P_{out, i}}{P_{in}} = \sum PCE_{p, i} \quad (4.1)$$

In the simplest 2-J RAINBOW solar cell scenario with red and blue sub-cells, [Equation 4.1](#) can be rewritten as:

$$\begin{aligned} PCE_R &= \frac{P_{out, red} + P_{out, blue}}{P_{in}} \\ &= \frac{P_{out, red}}{P_{in}} + \frac{P_{out, blue}}{P_{in}} \quad (4.2) \\ &= PCE_{p, red} + PCE_{p, blue} \end{aligned}$$

$P_{out, cell}$ is calculated as the multiplication between V_{oc} , J_{sc} , and FF of each sub-cell. Theoretically, all three parameters will depend on the spectrum that each sub-cell receives (φ_{cell}). Nevertheless, the model considers that the only parameter that depends on φ_{cell} is the J_{sc} . The model considers that the other parameters (V_{oc} and FF) are equal to the values measured under 1-Sun illumination.

$$P_{out, cell} = J_{sc}(\varphi_{cell}) \cdot V_{oc, \text{AM1.5G}} \cdot FF_{\text{AM1.5G}} \quad (4.3)$$

$J_{sc}(\varphi_{cell})$ is calculated following:

$$J_{sc}(\varphi_{cell}) = A \int_0^{\infty} \frac{\varphi_{cell}(\lambda)}{\varepsilon_{ph}(\lambda)} EQE_{PV}(\lambda) q d\lambda \quad (4.4)$$

$\varepsilon_{\text{ph}}(\lambda)$ is the energy of a photon, and $\varphi_{\text{cell}}(\lambda)$ is the spectrum that the sub-cell receives from a certain spectral splitting configuration. A is a normalization factor used to match the measured and calculated J_{sc} at 1-Sun ($A = J_{\text{sc}}^{\text{measured}} / J_{\text{sc}}(\varphi_{\text{AM1.5G}})$). As happens for the moving guillotines of the SOLS (see [Section 3.2.3](#)), one can express φ_{cell} as the product between the full spectrum ($\varphi_{\text{AM1.5G}}$) and an edge function which depends on the dividing wavelength ($H(\lambda_d)$). In the simplest 2-J scenario:

$$\varphi_{\text{red}}(\lambda) = \varphi_{\text{AM1.5G}}(\lambda) H_{\text{red}}(\lambda, \lambda_d) \quad (4.5)$$

$$\varphi_{\text{blue}}(\lambda) = \varphi_{\text{AM1.5G}}(\lambda) H_{\text{blue}}(\lambda, \lambda_d) \quad (4.6)$$

where $H_{\text{red}}(\lambda, \lambda_d)$ and $H_{\text{blue}}(\lambda, \lambda_d)$ are the edge functions for the red and the blue sub-cells, respectively. The only requirement that H_{red} and H_{blue} have to satisfy is complementarity: the sum of both has to be equal to 1 for all wavelengths. In the simplest spectral division scenario (which is the case in all simulations of the thesis except otherwise specified) H_{red} and H_{blue} are sharp edge functions, defined as:

$$H_{\text{red}}(\lambda, \lambda_d) = \begin{cases} 0 & \text{if } \lambda < \lambda_d \\ 1 & \text{if } \lambda \geq \lambda_d \end{cases} \quad (4.7)$$

$$H_{\text{blue}}(\lambda, \lambda_d) = \begin{cases} 1 & \text{if } \lambda < \lambda_d \\ 0 & \text{if } \lambda \geq \lambda_d \end{cases} \quad (4.8)$$

With the presented mathematical expressions, we can calculate the RAINBOW efficiency as well as the partial contribution of each sub-cell for a certain λ_d . The next step is to study the RAINBOW efficiency as a function of the λ_d . The latter is done by repeating the simulation with λ_d values sweeping along the AM1.5G spectrum, typically from 400 to 1000 nm. As a result, a simulation of a 2-J RAINBOW solar cell gives the PCE_R , the $PCE_{p, \text{red}}$, and the $PCE_{p, \text{blue}}$ as a function of λ_d . Additionally, we also get the λ_d dependence of J_{sc} for both sub-cells ($J_{\text{sc},p,\text{red}}$ and $J_{\text{sc},p,\text{blue}}$) which sum gives the RAINBOW short-circuit photocurrent ($J_{\text{sc},R}$, as in [Equation 4.9](#)). The RAINBOW equivalent of V_{oc} and FF is not straightforward to define. A possible interpretation is given later in this chapter.

$$J_{\text{sc},R} = J_{\text{sc},\text{red}} + J_{\text{sc},\text{blue}} \quad (4.9)$$

4.2.2.2 RAINBOW figures-of-merit

Figure xxx shows an example of a RAINBOW simulation wherein we can define three important figures-of-merit of the RAINBOW multi-

junction configuration. The first one is the maximum RAINBOW efficiency ($PCE_{R,\max}$) which corresponds to the maximum efficiency that the RAINBOW device achieves for all possible λ_d values. The latter corresponds to an optimized spectral distribution, defined by $\lambda_{d,opt}$. The last FoM to consider is the increase over the best cell (IoBC) which is defined as the percentual increase of the $PCE_{R,\max}$ with respect to the best single junction (see [Equation 4.10](#)). With these three FoM, we can compare the RAINBOW performance between different sub-cell materials in order to find material candidates suitable for the RAINBOW multi-junction geometry.

$$IoBC = \frac{PCE_{R,\max}(\lambda_d = \lambda_{d,opt}) - PCE_{AM1.5G,best\ sub-cell}}{PCE_{AM1.5G,best\ sub-cell}} \quad (4.10)$$

4.2.2.3 Simulations with ideal EQE_{PV} curves

To establish a basic set of guidelines for material combination selection in RAINBOW solar cells we first employed the simulation model to evaluate the performance of a series of sub-cell material combinations, with idealized top hat EQE_{PV} curves, sigmoid edges and varying widths and heights. The edge of the EQE_{PV} curves was used to calculate E_{bg} , from which the V_{oc} was obtained combining the Shockley-Queisser limit and a polynomial fit from the data published in reference [[SULLBRICH2019](#)]. The FF was assumed to be constant at 65% for all sub-cells. These $J - V$ parameters, along with the EQE_{PV} curves, were fed into the model to evaluate the RAINBOW performance of every possible ideal EQE_{PV} combination. In the following paragraphs, we discuss some of the most relevant simulation cases, which give us an intuitive sense of the parameters that ultimately determine RAINBOW performance and their relative contribution.

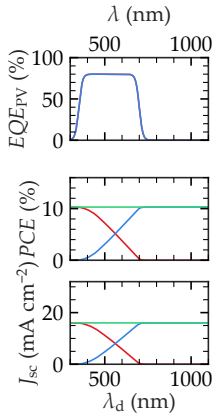


Figure 4.2: Rainbow simulation with equal sub-cells. PCE_R is constant for all λ_d and the resulting IoBC is 0%.

To do so, we begin by the trivial case, where the red and blue sub-cells have exactly equal EQE_{PV} curves, both are effectively the same cell ([Figure 4.2](#)). In this case, as we shift the dividing wavelength, the combined efficiency stays constant, since the changes in the partial efficiencies of each sub-cell are perfectly complementary, resulting in a 0% IoBC. This result is perfectly logical, since, having the same E_g and equal EQE_{PV} curves, each sub-cell is competing for the same light. As a result, they both absorb the same amount of photons in the same spectral range with equal thermalization losses, so there is no benefit in redistributing the light spectrum between the two.

[Figure 4.3](#) (a) shows a RAINBOW combination where the red sub-cell completely outperforms the blue sub-cell. In this case, the combined

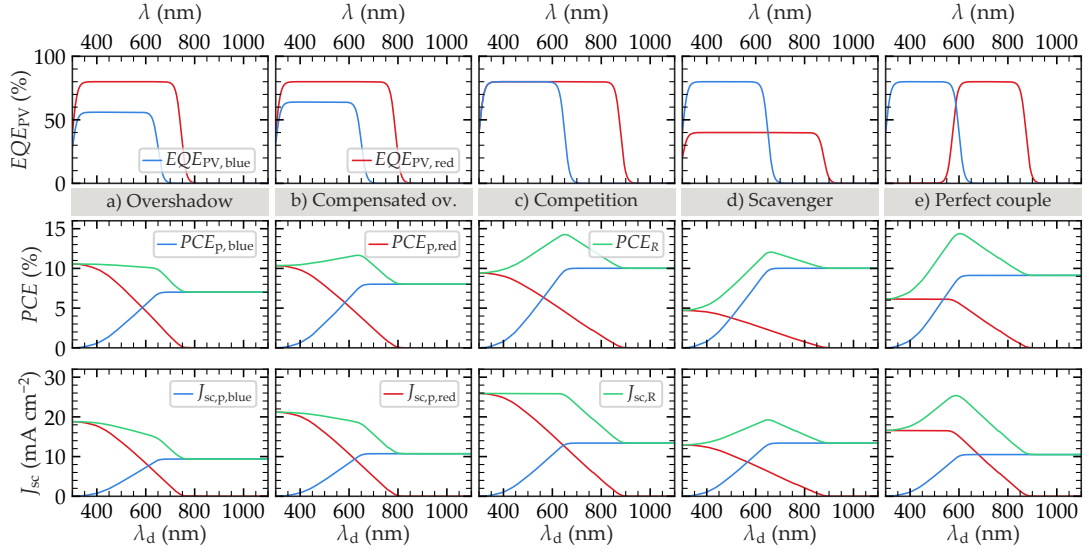


Figure 4.3: Relevant examples of RAINBOW simulations with top-hap EQE_{PV} . Simulation results are shown in columns (EQE_{PV} , PCE , and J_{sc} in top, middle, and bottom panels, respectively) for cases named overshadow (a), compensated overshadow (b), complementary competition (c), photon scavenger (d), and perfect couple (e). The resulting increase over the best cell (IoBC) is 0%, 12%, 42%, 20%, and 58%, respectively.

efficiency never rises above the efficiency of the red sub-cell, resulting in a 0% IoBC. That is because the blue sub-cell's lower thermalization losses cannot compensate for its low EQE_{PV} values (i.e., low J_{sc}). As a result, any photon we take from the red sub-cell to illuminate the blue sub-cell will result in a lower combined efficiency. For this reason, we name this case "overshadow". A variant of the latter can be seen in Figure 4.3 (b), where EQE_{PV} of the red sub-cell is still overshadowing that of the blue sub-cell but because the EQE_{PV} of the latter is a little bit higher than in the previous case, the lower thermalization losses of the blue sub-cell are able to compensate for its lower EQE_{PV} values. As a result, the RAINBOW multi-junction exhibits a positive but moderate IoBC.

The second case, named "complementary competition" (Figure 4.3 (c)), is closer to the ideal combination, with both sub-cells having equal maximum EQE_{PV} values, but with a much wider absorption spectrum for the red sub-cell, arising from a lower E_{bg} . In this scenario, the two sub-cells compete for light in the shorter wavelength range of the spectrum while complementing each other on the longer wavelength range. On the spectral region where they overlap, the blue sub-cell is able to convert light energy more efficiently, having lower thermalization losses and equal EQE_{PV} values. The red sub-cell will efficiently convert the lower energy fraction of the spectrum since the blue sub-cell cannot

absorb those photons below its E_{bg} , resulting in one of the highest IoBC values.

In a variation of this case, named "photon scavenger" ([Figure 4.3 \(d\)](#)), the red sub-cell is set to have a lower maximum EQE_{PV} values compared to the blue sub-cell and a significantly lower E_{bg} . In this case, since the blue sub-cell cannot absorb photons below its E_{bg} , even if the red sub-cell has significantly lower EQE_{PV} values, the IoBC will always be greater than zero because the red sub-cell is "scavenging" the photons that the blue sub-cell cannot make use of.

Finally, the ideal case in terms of IoBC, named "perfect couple" ([Figure 4.3 \(e\)](#)), is the one in which the EQE_{PV} of the red and blue sub-cells do not overlap in any part of the spectrum. This case is similar to the complementary competition ([Figure 4.3 \(c\)](#)), but in this case there is no competition between the two sub-cells, resulting in a greater IoBC. We want to note that even though the IoBC is greater for this case, the maximum theoretical efficiency is equal for the two cases. However, achieving high absorption values along the entire spectrum is generally difficult, especially in OPV,[[MVenzie2016](#)] we considered this case relevant enough to treat it separately.

As a side curiosity, if we have a RAINBOW system with a positive IoBC and we shine the wrong fraction of the spectrum to each sub-cell, the resulting graph will look like the one in ([Figure 4.4 \(b\)](#)), where the combined efficiency goes below that of the lowest-performing cell. This is a clear indication that we have swapped the sub-cells order and that the system is a good RAINBOW combination.

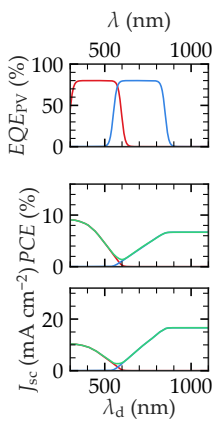


Figure 4.4: Main sentence. Caption

In the examples shown here as ideal EQE_{PV} curves (i.e., lossless sub-cells with top hat-shaped EQE_{PV} curves) the optimal λ_d coincides with the E_{bg} of the blue sub-cell, as one may expect. Nonetheless, in real devices with spectrally irregular EQE_{PV} curves and different total voltage loss (ΔV_{oc}^{total}) values, the optimum light splitting should be determined case by case. This is the reason why simulations are done sweeping λ_d along the spectrum.

4.2.2.4 Material selection criteria

From the examples shown in [Figure 4.3](#), we can identify the following guidelines for material selection in order to maximize PCE_R :

LOW V_{oc} LOSSES To reduce thermalization losses, each sub-cell needs to have inherently low voltage losses, ΔV_{oc}^{total} , particularly the

blue sub-cells. Otherwise, even with higher band gaps, thermalization losses will not be reduced. This is similar to any other multi-junction configuration.

SIMILAR EQE_{PV} VALUES AROUND THEIR RESPECTIVE E_{BG} In a RAINBOW configuration, each sub-cell will likely receive the spectral region closer to its E_{bg} , where most organic materials have their strongest absorption band. If there is a spectral region where red and blue EQE_{PV} s overlap, the EQE_{PV} of the blue sub-cell should be, at least, as high as that of the red sub-cell, otherwise, there will be a compromise between better V_{oc} and worse J_{sc} . Interestingly, in this configuration, materials should be maximum EQE_{PV} matched, a condition easier to achieve than the current matching required in series connected tandem stacks.

HIGH SUB-CELL EFFICIENCIES Generally speaking, the RAINBOW efficiency is directly related to the achievable individual efficiency of each sub-cell, which must be as high as possible. However, the cell parameters for maximum PCE_R can differ from the optimal values of the individual cells. In particular, we expect that in general, optimal RAINBOW sub-cells may be thinner than their single junction counterparts. That is because each sub-cell is only illuminated around its absorption maximum, where thin films are capable of absorbing most light, with the added benefit of thinner cells exhibiting a higher FF . Compared to a tandem stack, the thickness of each sub-cell can be optimized independently, as no filtering effects occur.

Moreover, in order to maximize IoBC, additional selection criteria arise:

HIGH COMPLEMENTARITY To maximize IoBC, it is ideal for the absorption and EQE_{PV} curves of each sub-cell to have minimal overlap while spanning as wide a fraction of the solar spectrum as possible when combined, i.e., to be complementary. The first condition maximizes the ratio between $J_{sc,R}$ and $J_{sc,cell}$, while the second increases $J_{sc,R}$ due to a wider absorption range.

SIMILAR MAXIMUM PCE VALUES To have a large IoBC, each sub-cell within a RAINBOW combination should have similar PCE values. Note that the highest IoBC does not necessarily lead to the highest PCE .

4.2.3 RAINBOW characterization with SOLS

The spectrum on-demand light source (SOLS) presented in the previous chapter ([Chapter 3](#)) was developed for the characterization of

RAINBOW solar cells. It is another tool that enables us to predict RAINBOW efficiency from measurements. It is recommended to the reader to take a look at [Chapter 3](#), especially at [Section 3.2.3](#) where the masking element in charge of RAINBOW characterization (the automatized guillotines) is explained.

4.2.3.1 RAINBOW characterization procedure

In general, the RAINBOW characterization is done for a 2-J device with blue and red sub-cells with higher and lower E_{bg} , respectively. Under AM1.5G illumination and in spectral splitting geometry, the red sub-cell receives the lower energy part of the solar spectrum, i.e., from ≈ 1100 nm up to the dividing wavelength λ_d , whereas the blue sub-cell receives the complementary part, i.e., between λ_d and ≈ 390 nm. The aim of the measurement is to determine the optimum λ_d as well as measure the PCE_R . The measurements are performed with the card mask of 1 Sun AM1.5G spectrum (shown in [Figure 3.8](#) (a) and [Figure 3.9](#) (a)) and then moving the motorized guillotines ([Section 3.2.3](#)). The $J - V$ response of the single-junction cell is measured at each guillotine position (i.e., for each λ_d). Typically, λ_d stepsize is 5 nm.

The measurement procedure is as follows: each sub-cell is subsequently placed at the end of the homogenizing light pipe for homogeneous illumination. Then, the response of the red sub-cell is determined for a so-called “red sweep”, for which the starting position of the guillotine is at $\lambda_d = \lambda_{d,\min}$, where the red sub-cell is illuminated with the full spectrum, and then moves to the red up to $\lambda_d = \lambda_{d,\max}$. On the contrary, for the blue sub-cell, illumination proceeds as a “blue sweep”, in which the opposite guillotine starts at $\lambda_d = \lambda_{d,\max}$, again allowing full spectrum illumination, but moves to the blue toward $\lambda_d = \lambda_{d,\min}$.

The values of $\lambda_{d,\min}$ and $\lambda_{d,\max}$ can vary slightly depending on the position of the beam with respect to the guillotines which is considered in the calibration of the motors. $\lambda_{d,\max}$ is limited by the low color separation in the red and IR regions and corresponds to a spectrum with almost no light for a red sweep and a full spectrum for a blue sweep. On the other hand, the limitation of $\lambda_{d,\min}$ comes from a too large dispersion resulting in some blue light being already blocked by the limits of the guillotines and corresponds to a null spectrum for the blue sweep and the full spectrum for the red sweep. Additionally, the blue and UV region intensity at the output of the homogenizer is weak due to absorption in the different components. In the actual guillotine calibration of the setup, $\lambda_{d,\max}$ is 810 nm while $\lambda_{d,\min}$ is 390 nm.

Additionally, red and blue sweeps have another descriptor regarding the direction of the sweep: "closing" refers to starting the measurement with the full spectrum and ending it in dark; while "opening" refers to starting the measurement in dark and ending it with the full spectrum. We have not seen an important difference between closing or opening sweeps if the devices are stable enough. For this reason, the direction of the sweep is generally not specified in the SOLS measurements.

4.2.3.2 Choice of materials

With the selection rules described in the previous subsection, we searched for possible combinations of materials for the first RAINBOW architecture demonstration. We selected three commercially available active layer blends, covering a broad range of E_{bg} : PM6:IO-4Cl,[39, 40] PM6:Y6[41, 42] and PTB7-Th:COTIC-4F,[JLee2018, NSchopp2022, AAATorimtubun2024]. Their chemical structures are shown in Figure XXX. The wide E_{bg} of 1.8 eV of the PM6:IO-4Cl blend makes it more suitable for the blue sub-cell, as we can see from its EQE_{PV} curve (Figure 4.5 (a) blue curve), whereas the extremely narrow gap of 1.12 eV of PTB7-Th:COTIC-4F is more adequate for the red sub-cell (Figure 4.5 (a) red curve). Conversely, PM6:Y6, which has an intermediate gap value of 1.4 eV, can function either as the blue or the red sub-cell (Figure 4.5 (a) green line), depending on which of the other two blends is used in the 2-J RAINBOW combination. We note that even if the reported efficiencies of PM6:IO-4Cl and PTB7-Th:COTIC-4F are not amongst the highest in OPV, these materials exhibit extreme E_{bg} on opposite sides of the spectrum, with relatively low voltage losses within organic materials ($\Delta V_{oc}^{\text{total}} \approx 0.6$ V, Table 4.1), which makes them ideal for testing the feasibility of the RAINBOW solar cell concept.[JLee2018, JLee2019, 39, 42]

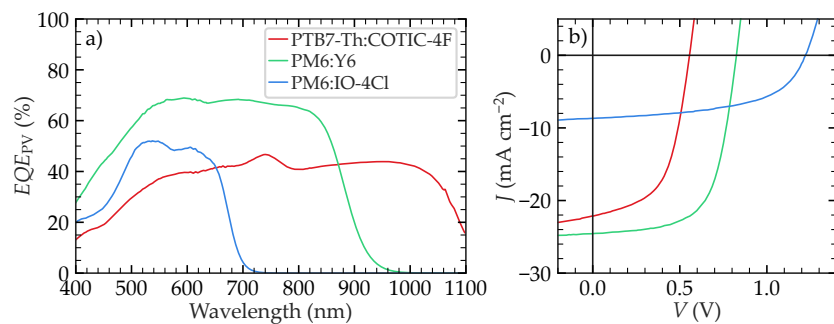


Figure 4.5: EQE_{PV} (a) and $J - V$ curves (b) of the selected materials used for the simulation model.

	PTB7-Th:COTIC-4F	PM6:Y6	PM6:IO-4Cl
E_{bg} (eV)	1.15	1.41	1.85
V_{oc} (V)	0.56	0.82	1.22
$\Delta V_{oc}^{\text{total}}$ (V)	0.59	0.59	0.63

Table 4.1: V_{oc} losses of the blends studied. E_{bg} was measured with the inflection point of the EQE_{PV} edge.

Active layer blend	V_{oc} (V)	J_{sc} (mA cm^{-2})	FF (%)	PCE (%)
PTB7-Th:COTIC-4F	0.56	22.14	55.65	6.84
PM6:Y6	0.82	24.55	63.99	12.93
PM6:IO-4Cl	1.22	8.67	54.94	5.83

Table 4.2: Figures-of-merit of the active layer materials selected for the RAINBOW study. The FoM corresponds to the $J - V$ curves shown in Figure 4.5 (b).

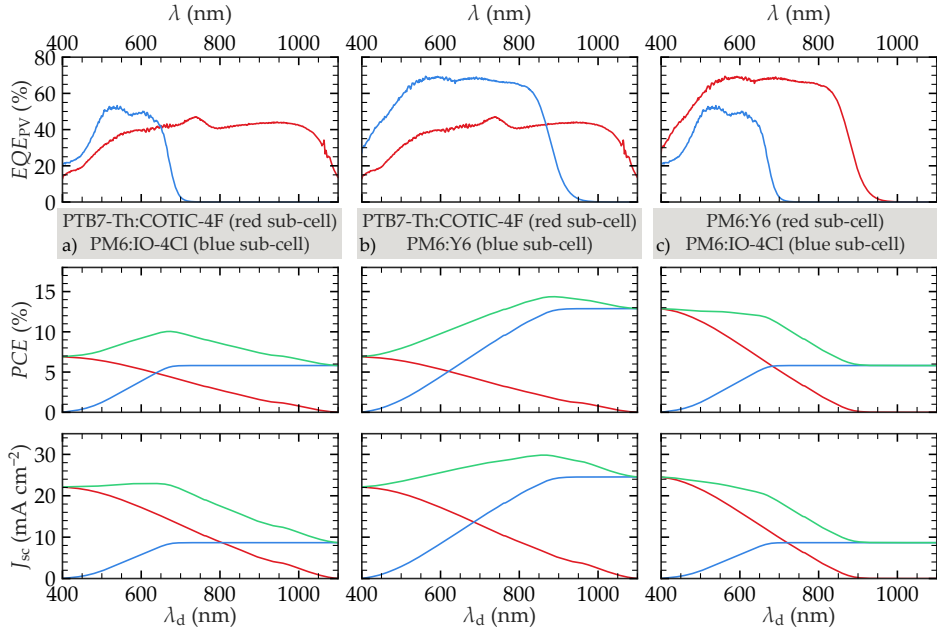


Figure 4.6: RAINBOW simulations with solar cells fabricated with the selected materials. Simulation results are shown in columns (EQE_{PV} , PCE , and J_{sc} in top, middle, and bottom panels, respectively) for 2-J RAINBOW geometries with PTB7-Th:COTIC-4F as red sub-cell and PM6:IO-4Cl as blue sub-cell (a), PTB7-Th:COTIC-4F as red sub-cell and PM6:Y6 as blue sub-cell (b), and PM6:Y6 as red sub-cell and PM6:IO-4Cl as blue sub-cell (c). The RAINBOW figures-of-merit are summarized in table Table 4.3

Using these materials, we manufactured and characterized well-performing solar cells, from which we obtained the $J - V$ and EQE_{PV} curves (Figure 4.5 (a) and (b), respectively) that were fed into the simulation model. In this case, the cells were prepared by spin-coating instead of blade coating. The spin-coating substrates used are smaller and each one contains eighth cells with an area of $2 \text{ mm} \times 2 \text{ mm}$. Since the deposition technique used for ETL and AL is spin-coating, the devices are homogeneous in thickness. In this case, different thicknesses were tested by spin-coating at different velocities, and the best-performing cells were selected. In this way, the theoretical PCE_R was calculated for the three 2-J RAINBOW combinations between the materials blends.

Simulation in Figure 4.6	Active layer materials		RAINBOW figures of merit		
	Red sub-cell	Blue sub-cell	PCE_{\max} (%)	IoBC (%)	$\lambda_{d,\text{opt}}$ (nm)
a)	PTB7-Th:COTIC-4F	PM6:IO-4Cl	10.05	45.71	670
b)	PTB7-Th:COTIC-4F	PM6:Y6	14.37	11.54	885
c)	PM6:Y6	PM6:IO-4Cl	12.88	0.00	-*

Table 4.3: RAINBOW FoM for materials simulations shown in [Figure 4.6](#). *The third combination c), do not show any RAINBOW efficiency increase. For this reason, IoBC is 0, and $\lambda_{d,\text{opt}}$ do not has a value.

We first consider the wide-narrow gap combination, using PM6:IO-4Cl as the blue cell and PTB7-Th:COTIC-4F as the red cell ([Figure 4.6](#) (a)). This combination yields the best results in terms of increase over the best cell, with a value of 41% (see [Table 4.3](#)). with a maximum PCE_R of 10.1%. The latter happens at a $\lambda_{d,\text{opt}} = 570$ nm, slightly below the band gap of the blue sub-cell. Even if the resulting combined efficiency is not amongst the highest in OPV, this combination is a remarkable example of a better final PCE_R due to a reduction in thermalization and absorption losses. For this combination, the complementary competition example shown in [Figure 4.3](#) (c) is the closest case.

The other functional RAINBOW cell is the intermediate-narrow gap combination, using PM6:Y6 as the blue sub-cell and PTB7-Th:COTIC-4F as the red sub-cell ([Figure 4.6](#) (b)). The latter yields a positive IoBC of 10.5% and a maximum combined efficiency of 13.7% (see [Table 4.3](#)). In this combination, the optimal λ_d , $\lambda_{d,\text{opt}}$, is located just below the band gap of the blue sub-cell, most likely because of its high performance when compared with the red sub-cell. In this case, the red sub-cell (PTB7-Th:COTIC-4F), even with its significantly lower EQE_{PV} values, is able to capture the lower energy photons that the blue sub-cell (PM6:Y6) cannot absorb, resulting in a higher photocurrent for the RAINBOW combination. This material combination behaves similarly to the photon scavenging example presented in [Figure 4.3](#) (d).

On the opposite, the wide-intermediate gap combination between PM6:IO-4Cl as the blue sub-cell and PM6:Y6 as the red sub-cell ([Figure 4.6](#) (c)) exhibits null IoBC (see [Table 4.3](#)). This is because the EQE_{PV} curve of the blue sub-cell (PM6:IO-4Cl) is entirely overshadowed by that of the red sub-cell (PM6:Y6). As a result, the lower thermalization losses of the blue sub-cell cannot compensate its lower photocurrent, resulting in a non-functional RAINBOW combination, where the maximum combined efficiency is equal to that of the best-performing sub-cell (the red). This is a case similar to the overshadowing presented in [Figure 4.3](#).

(a).

4.2.3.3 Model validation via RAINBOW characterization with SOLS

To validate the model we have chosen to perform SOLS RAINBOW measurements on the two successful RAINBOW combinations. First of all we focus on the wide-narrow band combination, because of its high calculated IoBC, and its optimal dividing wavelength range that falls well within the SOLS spectral shaping capabilities. The individual SOLS characterization of the red and blue sub-cells (shown in [Figure 4.7](#)) provides us with insights to assess the validity of the model assumptions. For the red sub-cell (PTB7-Th:COTIC-4F) we notice that *PCE* behaviour is mainly driven by the J_{sc} component, where the V_{oc} and FF rapidly saturate, with minor variations throughout the entire λ_d range ([Figure 4.7](#)). This behavior is consistent with the model initial assumptions (constant V_{oc} and FF), where the rapid saturation can be attributed to the relation of V_{oc} and FF with increasing illumination intensity, a phenomenon well reported in the literature.[\[Cui20191Efficiency, Stein2011OrganicApplications, Schilinsky2004SimulationCells, Koster2005LightCells\]](#) Notice that this saturation behavior observed with the SOLS is likely to begin at λ_d closer to the extremes in a real RAINBOW device since, due to spectral redistribution, light power density is higher (spectrally concentrated) for each sub-cell than it is in the SOLS measurement. The latter is because, in the SOLS setup, the varying spectrum is achieved by masking the unwanted half of the spectra but not by spectral reconcentration. We see that, above a certain light intensity threshold, the λ_d dependence of these two parameters seems to play a minor role in determining the final partial efficiency of each sub-cell, being eclipsed by the λ_d dependence of J_{sc} .

Intuitively, we can see that the J_{sc} of each sub-cell is proportional to the fraction width of the illuminating spectrum, as wider spectral fractions will encompass a higher amount of photons. However, we notice that for the blue sub-cell (PM6:IO-4Cl), the J_{sc} slope changes suddenly after the dividing wavelength sweep surpasses 700 nm, bringing the current increase almost to a halt ([Figure 4.7](#) (a)). This sudden slope change can be attributed to the lack of photon absorption below 700 nm, which corresponds to the E_{bg} of PM6:IO-4Cl. Meanwhile, with a E_{bg} well below the measuring range of the SOLS setup, the PTB7-Th:COTIC-4F red sub-cell has a J_{sc} component that constantly increases with wider spectral fractions.

By merging these two measurements as a function of the dividing wavelength, we can calculate the RAINBOW performance of the

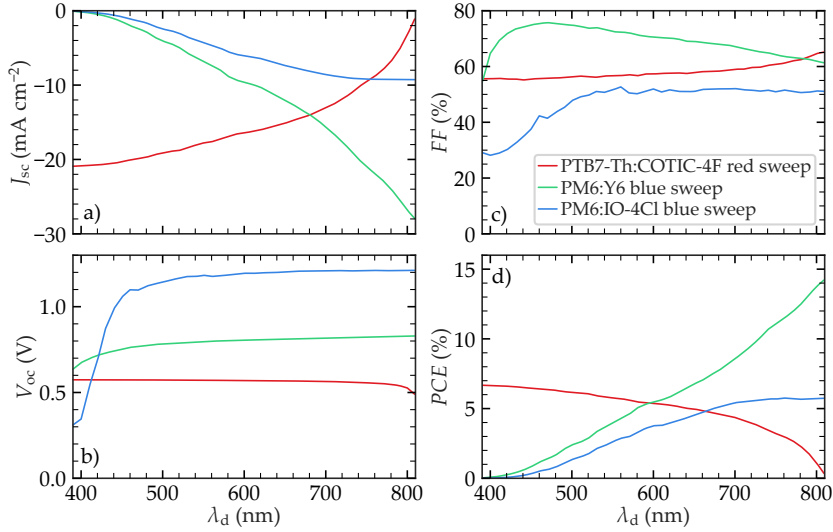


Figure 4.7: Results of RAINBOW characterization with SOLS. V_{oc} , J_{sc} , FF and PCE are plotted in panels a), b), c), and d), respectively as a function of λ_d . The red line corresponds to a red sweep performed on the PTB7-Th:COTIC-4F device, the green line corresponds to a blue sweep performed on the PM6:Y6 cell, and the blue line corresponds to a blue sweep performed on the PM6:Y6 cell.

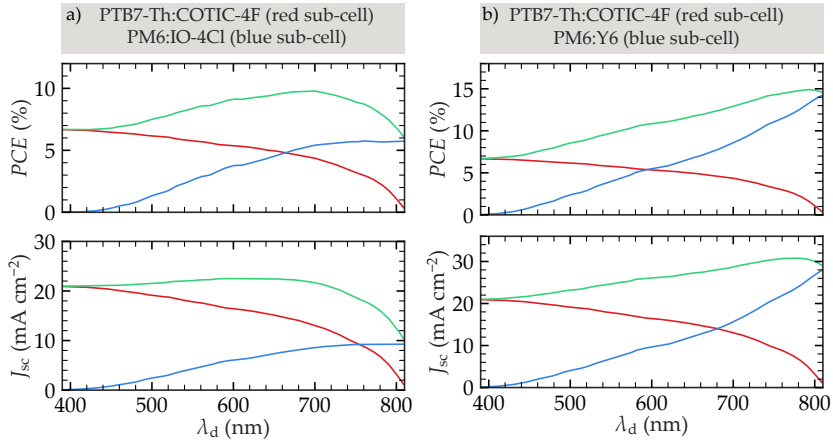


Figure 4.8: RAINBOW analysis with SOLS characterization. PTB7-Th:COTC-4F // PM6:IO-4Cl (a) and for PTB7-Th:COTIC-4F // PM6:Y6 (b) 2-J RAINBOW systems are evaluated by merging the RAINBOW characterization of each sub-cell shown in Figure 4.7. Table 4.4 shows the RAINBOW FoM.

wide-narrow gap combination (PM6:IO-4Cl and PTB7-Th:COTIC-4F, respectively) resulting in a high IoBC of 46.6% (Figure 4.8 (a)) and a $\lambda_{d,\text{opt}} = 700 \text{ nm}$. This high IoBC agrees with previous simulations and calculations, where the significant reduction of thermalization

Measruement in Figure 4.8	Active layer materials		RAINBOW figures of merit		
	Red sub-cell	Blue sub-cell	PCE_{\max} (%)	IoBC (%)	$\lambda_{d,\text{opt}}$ (nm)
a)	PTB7-Th:COTIC-4F	PM6:IO-4Cl	9.78	46.6	700
b)	PTB7-Th:COTIC-4F	PM6:Y6	14.93	5.0	790

Table 4.4: RAINBOW FoM of the SOLS characterization of Figure 4.8.

and absorption losses results in a functional RAINBOW combination. Moreover, in these measurements, we also see that the optimal wavelength range is wider than predicted by the simulations. This could be partly due to the SOLS setup's lack of sufficient spectral resolution. As seen in [Figure 3.12](#) (a) and (b) of the previous chapter, the edge of the red and the blue spectra have a full width at half maximum (FWHM) at λ_d of approximately 30 nm. Therefore, there is a certain wavelength range where light is not fully redirected to its best photovoltaic converter. The latter is also seen in [Figure 4.9](#) where we simulate the effect of increasing the FWHM from 0 to 80 nm. As a result, the IoBC decreases, and the RAINBOW peak becomes wider. In turn, this has important implications for the design of the optical element, where a clear separation of the wavelengths around the optimum λ_d is desirable.

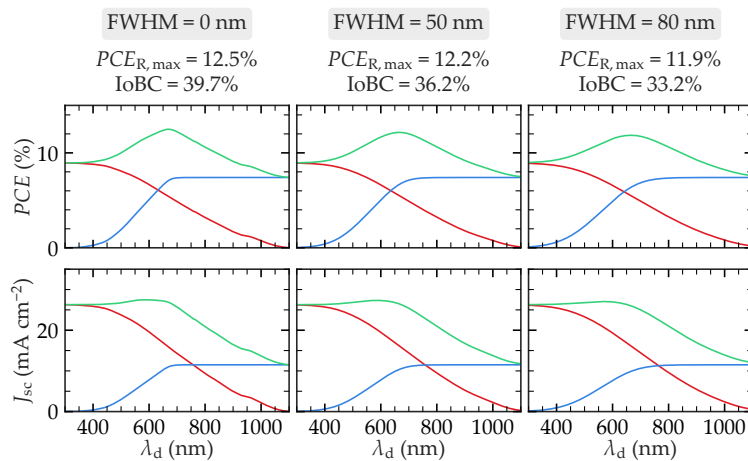


Figure 4.9: Simulations to determine the effect of the spectral resolution of the SOLS setup on RAINBOW performance. The spectral division is calculated using a Fermi-Dirac distribution function with full width at half maximum (FWHM) of 0, 50 and 80 nm. The broadening effect of the RAINBOW device is appreciable. It explains the small differences between the simulations and the measurements using the SOLS setup and the need for a dispersion element with sharp light separation for the real application of RAINBOW solar cells.

The intermediate-narrow gap combination between PM6:Y6 as the blue sub-cell and PTB7-Th:COTIC-4F as the red sub-cell was also characterized with the SOLS. Since we already have the measurement of the red sub-cell we only need to add the characterization of the PM6:Y6 device with a blue sweep ([Figure 4.7](#) green line). In this case, since PM6:Y6 has a flat EQE_{PV} between 900 and 500 nm, as seen in [Figure 4.5](#) (a), the slope of the J_{sc} dependence on λ_d is almost constant. The latter dependence is also reflected on PCE . According to the simulation results ([Table 4.3](#)) the intermediate-narrow gap combination shows the maximum IoBC at a $\lambda_{d,opt} = 885$ nm with a value of 11.50%. The RAINBOW measurement analysis ([Figure 4.8](#) (b)) shows a maximum IoBC of 5.0% at $\lambda_{d,opt} = 790$ nm. The significant differences can be explained by considering the limitations of the SOLS setup. First of all, the theoretical $\lambda_{d,opt}$ is outside the λ_d range of the equipment, which can measure up to $\lambda_{d,max} \approx 805$ nm. Additionally, the commented low spectral separation at high λ_d also introduces some differences as in the previous case.

4.2.4 Monolithic proof-of-concept device

Having validated our simulation model with the SOLS measurements, we proceeded to manufacture a monolithic proof-of-concept device that includes two junctions deposited side by side, representing the simplest embodiment of a RAINBOW solar cell.

To manufacture the monolithic proof-of-concept device, we selected the same two combinations as in the characterization with SOLS, i.e. the wide-narrow and the intermediate-narrow gap combinations. To fabricate such a device on a small scale we developed a technique called partial coverage radial (PCR) spin coating, which results in a partial deposition with a well defined border within a small substrate. This technique is easy to reproduce without specialized equipment and allows us to sequentially deposit multiple junctions in a single substrate with clearly defined boundaries, making it a useful technique in RAINBOW solar cell lab scale optimization. [Section 2.2.1](#) shows more details on the technique as well as evidence of a clean and straight boundary between the two materials deposited side by side.

The EQE_{PV} and $J - V$ curves of the monolithic devices were measured and fed into the numerical model to calculate the optimal dividing wavelength ($\lambda_{d,opt}$) and the expected $PCE_{R,max}$ and IoBC. As we can see in [Figure 4.10](#), both combinations exhibit a positive IoBC and relatively good combined efficiencies. In the case of PM6:Y6 as the blue sub-cell and PTB7-Th:COTIC-4F as the red sub-cell ([Figure 4.10](#) (a)),

we see that the EQE_{PV} curves are highly complementary, resulting in a great calculated $PCE_{R,max}$ of 13.25% with an IoBC of 11.39% at a $\lambda_{d,opt}$ of 885 nm. On the other hand, we see that the RAINBOW combination with PM6:IO-4Cl as the blue sub-cell and PTB7-Th:COTIC-4F as the red sub-cell (Figure 4.10 (b)) is expected to exhibit an excellent performance with a calculated IoBC of 47.64% and a $PCE_{R,max}$ of 9.91% at a $\lambda_{d,opt}$ of 670 nm. This is a consequence of the highly complementary EQE_{PV} curves of each sub-cell.

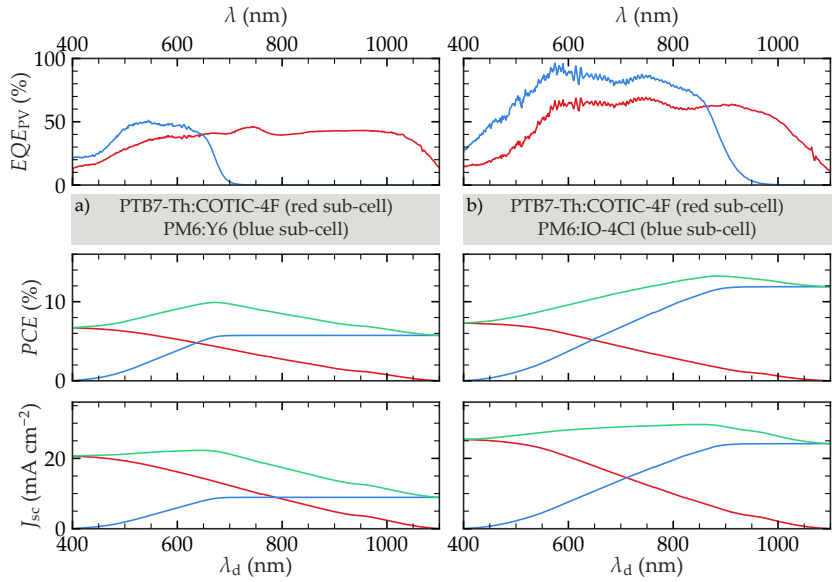


Figure 4.10: First monolithic RAINBOW device combined performance calculations, using the EQE and JV curves as input data. (left) PM6:Y6 as the “blue cell” and PTB7-Th:COTIC-4F as the “red cell”, (right) PM6:IO-4Cl as the “blue cell” and PTB7-Th:COTIC-4F as the “red cell”.

In this case, instead of using the SOLS setup, to further validate the simulation results we used a more accessible solution to characterize the sub-cells: an LED-based solar simulator, which consists of an array of 21 individually addressable LEDs. This setup is capable of providing homogeneous illumination with discrete fractions of the solar spectrum by varying each LED intensity. We used our simulations to set the dividing wavelength on the LED solar simulator to be as close as possible to the optimal simulated $\lambda_{d,opt}$ for each RAINBOW combination, namely at ~ 860 nm and ~ 690 nm for the intermediate-narrow and wide-narrow gap cell combinations respectively. Figure 4.11 shows the red and blue spectra used for the characterization of the wide-narrow (a) and the intermediate-narrow (b) band gap RAINBOW

combinations.

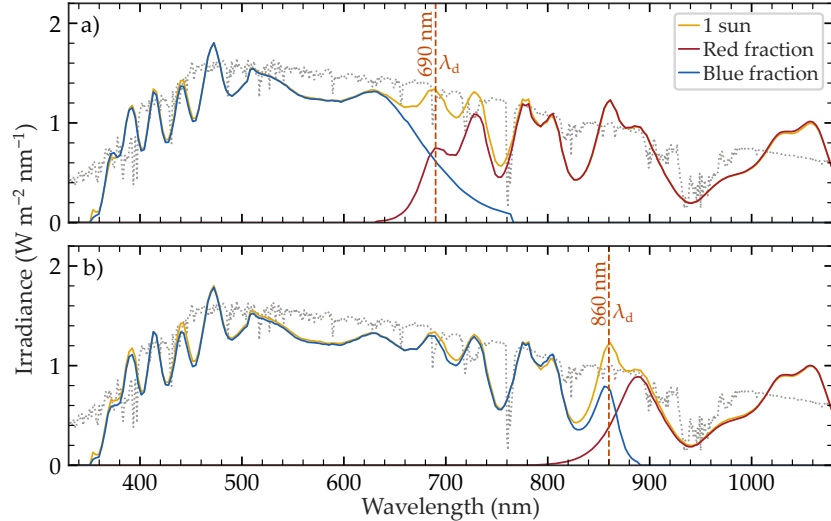


Figure 4.11: LED solar simulator spectra used for the characterization of monolithic RAINBOW devices, with the two fixed dividing wavelengths and their respective spectral fractions. Further analysis can be found to the manuscript.

Material	spectral fraction	V_{oc} (V)	FF (%)	J_{sc} (mA cm $^{-2}$)	PCE (%)
PM6:IO-4Cl (blue sub-cell)	1 Sun	1.20	53.6	8.92	5.75
	Blue fraction	1.20	51.8	8.60	5.32
PTB7-Th:COTIC-4F (red sub-cell)	1 Sun	0.58	55.96	20.68	6.71
	Red fraction	0.56	60.66	11.97	4.04
RAINBOW	Combined	0.83	-	20.57	9.36
	RCoBC (%)	42.69	-	-0.53	39.50*

Table 4.5: Monolithic RAINBOW device performance, with PM6:IO-4Cl as the blue sub-cell and PTB7-Th:COTIC-4F as the red sub-cell. The RAINBOW characterization is measured with the LED solar simulator with various spectra, simulating the behavior of the SOLS setup for a single dividing wavelength of approximately 690 nm. The result is a PCE_R of 9.36% corresponding to 39.50% increase over the best cell (IoBC) marked with *. RCoBC refers to the combined RAINBOW values compared to the best-performing single junction device.

[Table 4.5](#) and [Table 4.6](#) summarize the monolithic RAINBOW cell characterization results. The upper table section shows the $J - V$ parameters obtained for each sub-cell under full sun illumination and using only the corresponding fraction of the solar spectrum, red or blue. For the RAINBOW device (bottom table section), the rainbow PCE (PCE_R) and the increase over the best cell (IoBC) are calculated from the measurements of the sub-cells following [Equation 4.2](#) and

Material	spectral fraction	V_{oc} (V)	FF (%)	J_{sc} (mA cm^{-2})	PCE (%)
PM6:Y6 (blue sub-cell)	1 Sun	0.81	60.8	24.18	11.94
	Blue fraction	0.81	61.0	22.31	11.05
PTB7-Th:COTIC-4F (red sub-cell)	1 Sun	0.57	50.7	25.39	7.35
	Red fraction	0.54	58.6	7.09	2.26
RAINBOW	Combined	0.74	-	29.40	13.31
	RCoBC (%)	-8.04	-	21.59	11.47*

Table 4.6: Monolithic RAINBOW device performance, with PM6:Y6 as the blue sub-cell and PTB7-Th:COTIC-4F as the red sub-cell. The RAINBOW characterization is measured with the LED solar simulator with various spectra, simulating the behavior of the SOLS setup for a single dividing wavelength of approximately 860 nm. The result is a PCE_R of 13.31% corresponding to 11.47% increase over the best cell (IoBC) marked with *. RCoBC refers to the combined RAINBOW values compared to the best-performing single junction device.

[4.10](#), respectively.

The first observation is that all of the sub-cells at 1 Sun operate with efficiencies similar to those of single-junction devices made by conventional deposition, i.e., without monolithic integration (see [Table 4.2](#), [Table 4.5](#), and [Table 4.6](#)). The latter suggest that the PCR spin-coating technique does not significantly affect the performance of the devices. For the wide-narrow gap combination (PM6:IO-4Cl as the blue sub-cell and PTB7-Th:COTIC-4F as the red sub-cell), we have obtained an IoBC of 39.50% with a PCE_R of 9.36% ([Table 4.5](#)), in good agreement with the simulations in [Figure 4.10](#) (a), which predicted an IoBC of 46.34% with a PCE_R of 9.82% at $\lambda_d = 690$ nm (see [Table 4.7](#)).

For the intermediate-narrow gap combination (PM6:Y6 as the blue sub-cell and PTB7-Th:COTIC-4F as the red sub-cell), we have obtained an IoBC of 11.41% with a PCE_R of 13.31% ([Table 4.6](#)), in very good agreement with the simulations of [Figure 4.10](#) (b), with values of 10.49% and 13.14%, respectively, at a λ_d of 860 nm (see [Table 4.7](#)). [Table 4.7](#) summarizes the comparison between the simulations and the characterization of the two studied monolithic RAINBOW solar cells.

We next try to estimate the importance on these RAINBOW cells of the two main mechanisms that operate in multi-junction solar cells, i.e., the reduction in the thermalization losses and the increase in absorption. In all cases, comparisons are made with respect to the best-performing single junction amongst sub-cells for a given monolithic device. To address the changes in absorption, we use as proxy the photocurrent density. In particular, we compare the J_{sc} of the best sub-cell with that of the RAINBOW device following [Equation 4.9](#). Clearly, this is only an approximation, since, besides being proportional to the absorption,

Blue sub-cell	Red sub-cell	Kind	Reference	PCE_R (%)	IoBC (%)	λ_d (nm)
PM6:IO-4Cl	PTB7-Th:COTIC-4F	Simulation	Figure 4.10 (a)	9.91	47.64	670
				9.82	46.38	690
		Measurement	Table 4.5	9.36	39.50	~ 690
PM6:Y6	PTB7-Th:COTIC-4F	Simulation	Figure 4.10 (b)	13.25	11.39	885
				13.14	10.49	860
		Measurement	Table 4.6	13.31	11.47	~ 860

Table 4.7: Comparison between the RAINBOW characterization with LEDs solar simulator and the simulations for the two RAINBOW systems studied.

charge transport and collection also affect the J_{sc} . In any case, as the materials and device stack being compared are the same, we use as a first approximation the changes in J_{sc} as being mainly related to changes in absorption.

On the other hand, thermalization of charges is often reflected in the energy of the extracted charges, and thus we use, again as proxy, the difference in V_{oc} between the best-performing single junction cell and that of the RAINBOW devices. Being an N-terminal device, the V_{oc} of the latter is not well-defined. To approximate an effective (or averaged) V_{oc} for the combined cells, we take into account that a fraction of the charges will be collected at the V_{oc} of the blue sub-cell, and the rest with the V_{oc} of the red sub-cell. A simple way of factoring this in, is by calculating the RAINBOW V_{oc} ($V_{oc,R}$) through the J_{sc} -weighted average of the corresponding sub-cell values (following [Equation 4.11](#)). This expression uses the photocurrent fraction as an approximation of the P_{in} average that each sub-cell receives, and it assumes that the FF of both sub-cells is approximately equal.

$$V_{oc,R} = \frac{V_{oc,red} \cdot J_{sc,red} + V_{oc,blue} \cdot J_{sc,blue}}{J_{sc,R}} \quad (4.11)$$

The last two rows in [Table 4.5](#) and [Table 4.6](#) show the parameters of the corresponding RAINBOW cells following [Equation 4.11](#), [Equation 4.9](#) and [Equation 4.2](#), as well as the relative change of the combined V_{oc} , J_{sc} and PCE ($V_{oc,R}$, $J_{sc,R}$ and PCE_R , respectively) concerning the best-performing single junction cell (RCoBC). Note that the RCoBC for the PCE corresponds to the aforementioned overall figure of merit IoBC (%). While being only estimates, the RCoBC can be used to give an idea of the origin of the IoBC or, in other words, whether thermalization and/or absorption losses are reduced.

For the wide-narrow gap combination (Table 4.5), the RCoBC analysis shows that this improvement basically comes from the V_{oc} RCoBC (42.69%), so in this case, the RAINBOW device does minimize thermalization losses. This is simply due to the high V_{oc} of the blue sub-cell, which is more than twice that of the red sub-cell.

On the other hand, for the intermediate-narrow gap combination (Table 4.6) the increase in efficiency is mainly related to an improvement in J_{sc} from the contribution of the red sub-cell (21.59% of RCoBC), which absorbs photons well below the E_{bg} of the blue sub-cell, showing a reduction on absorption losses. In fact, this even overcompensates the lower V_{oc} of the electrons extracted from the red sub-cell, which yields a worsening of the open-circuit seen as a negative V_{oc} RCoBC of -8.04% (notice that the best-performing cell is the blue sub-cell). Hence, this is an example of a RAINBOW combination that minimizes optical absorption losses.

4.3 RAINBOW SIMULATIONS WITH MULTIPLE MATERIALS

The work enclosed in the previous section showed the potential of the RAINBOW geometry. Nevertheless, the achieved RAINBOW efficiencies are much below the state-of-the-art single-junction and multi-junction of OPV. As discussed before, in order to achieve high PCE_R , one needs efficient sub-cells with E_{bg} spread along the spectrum. Our research group (NANOPTO) is not characterized as achieving efficiencies close to state-of-the-art. The latter is partly because we deposit the active layer by blade-coating, while most OPV works use spin-coating. TO BE CONTINUED

4.3.1 Effect of active layer thickness

One important parameter to consider in the optimization of RAINBOW solar cells is the active layer thickness. The latter has an impact on different properties of organic solar cells such as J_{sc} , FF or EQE_{PV} . Imagine an organic solar cell with a thin active layer (i.e., 50 nm thick). The EQE_{PV} curve is expected to have a profile similar to the absorption of the active layer material. The latter is generally shown as a high peak at the first absorption band of the donor and acceptor components. Due to the low amount of material, the amount of absorbed photons is small; therefore, J_{sc} is low. Conversely, FF generally shows its maximum at thin layers because the generated free charges have a smaller percolation path than thicker layers. Thus, the free-charge transport to the contacts is more efficient. As active layer thickness increases, J_{sc} will get higher

due to more photons absorbed in the active layer. Nevertheless, the free-charge transport to the contacts gets longer, decreasing FF .

Nevertheless, considering that sub-cells in the RAINBOW geometry are likely to receive only photons in the spectral region near its E_{bg} , some parameters are more important than others.

5

WIDE BAND-GAP ORGANIC PHOTOVOLTAICS

As seen in [Chapter 4](#), having a good-performing wide band gap sub-cell in a RAINBOW configuration is crucial for achieving higher efficiencies. Nevertheless, the field lacks studies on active layer materials that are able to achieve efficiencies as close to the theoretical limit as those exhibited by mid- and low-band-gap cells. In this chapter, we have explored different donor:acceptor combinations in a combinatorial screening manner. The donors used are PM6, PTQ10, and D18, while the acceptors used are IO-4Cl, PMI-FF-PMI, and O-IDFBR. The latter led to 9 different donor:acceptor combinations processed from 2 solvents, chloroform (CF) and chlorobenzene (CB). These combinations achieved remarkably high V_{oc} with values between 1.1 and 1.4 V, and in most cases being higher than 1.25 V. The novel blend PTQ10:O-IDFBR is the most promising active layer because of its high V_{oc} (1.35 V) is accompanied by one of the highest efficiency achieved in the combinatorial study (6.87 %). Selected devices were also studied regarding voltage loss characterization during a two-month stay at Prof. Thomas Kirchartz's labs in Forschungszentrum Jülich. Additionally, the chapter includes an indoor light harvesting study for the novel promising PTQ10:O-IDFBR blend.

5.1 INTRODUCTION

Organic photovoltaics (OPVs) have recently surpassed 20% efficiency, mainly thanks to the development of non-fullerene acceptors (NFAs) during the last years.[\[43, 37, 44, 45, 46, 47\]](#) These molecules exhibit stronger absorption and broader energy level tunability compared to the fullerene acceptors used since the early days of OPV technology.[\[48\]](#) The increased color tunability, as a result of the development of NFAs, together with the advantages of organic solar cells, such as their light weight, flexibility, and up-scalability, have expanded the range of applications of organic photovoltaics.

In this context, wide energy band-gap (E_{bg}) OPV (here meaning cells with photo-active layer energy band-gaps $E_{bg} > 1.8$ eV) are promising for harvesting light whose spectrum and conditions differ from the AM1.5G solar spectrum. This is the case, for example, for underwater light harvesting. Depending on water depth, sunlight becomes increasingly filtered in color.[\[6, 40\]](#) In general, this results in a blue-shift of the Shockley-Queisser optimum band-gap as a

An example of the spectrum dependence on water depth is shown in Figure 3.1 (c)

Few examples of the LED spectra are shown in Figure 3.1 (b).

function of depth, from the well-known 1.34 eV to values higher than 2 eV, depending on water depth and geographical area.[6, 49] Yang et al. have already shown 23.11% efficiency with the wide E_{bg} blend PM6:IO-4Cl at a depth of 5 m.[40] Another relevant application of wide E_{bg} OPV is the harvesting of indoor light, in which the benchmark efficiency reached 36%. [50] Other works also achieve high efficiencies with different materials and strategies, therefore showing the potential of OPV for indoor light harvesting.[7, 51, 52, 39, 53, 54, 55] For this application, wide E_{bg} cells are needed since the light source to be harvested is typically a light-emitting diode (LED), emitting between 400 and 700 nm with a variable spectrum depending on the LED bulb.[56, 21] Therefore, devices with $E_{bg} < 1.8$ eV are expected to suffer from unnecessarily high thermalization losses.

In this thesis, the application that motivated the study of wide E_{bg} OPV are RAINBOW multi-junction solar cells. During the previous chapters, we have demonstrated the importance of the wide E_{bg} sub-cell in multi-junction devices as well as the need for an efficient sub-cell with low voltage losses to reduce thermalization losses. Wide E_{bg} sub-cells are essential not only for RAINBOW devices but also for tandem multi-junction, where the current matching condition imposes J_{sc} to be similar to the other sub-cells.[38, 57, 58, 59, 44, 43] Therefore, for wide E_{bg} sub-cells need special attention due to the fewer investigations performed on wide E_{bg} sub-cells as compared to the narrow E_{bg} sub-cells.[46, 20]

As demonstrated in the literature, organic solar cells exhibit higher voltage losses compared to other photovoltaic technologies such as perovskites or silicon solar cells, resulting in a lower open-circuit voltage (V_{oc}).[20, 57, 60] The latter is understood as one of the main factors limiting the efficiency of organic solar cells. Precisely, non-radiative voltage losses (ΔV_{oc}^{nr}) due to the low emissivity nature of the charge-transfer state, are responsible for the high voltage loss compared with other technologies.[61, 62] Nevertheless, literature also shows that as charge-transfer state energy increases, non-radiative voltage losses decrease.[63, 64] Therefore, wide E_{bg} organic solar cells, prone to having higher charge-transfer state energies, a lower ΔV_{oc}^{nr} should be expected. Nonetheless, their efficiency is still far from the thermodynamic limit. In this case, the photo-generated current seems to be the bottleneck.[63, 20] Due to the different methodologies used for characterizing voltage losses, the field lacks of a systematic comparison of voltage losses to understand better the efficiency limitation of wide E_{bg} solar cells.[65, 63, 66, 61]

Additionally, the fast development of NFAs is generating a vast library of materials, thus opening enormous possibilities for active layer blends. Although efforts have been invested in developing a material selection and efficiency prediction algorithm, this is still an unsolved question for organic photovoltaics.[67, 68, 69] In this scenario, high-throughput and combinatorial screening approaches are needed to discover efficient donor:acceptor blends faster.

5.2 COMBINATORIAL SCREENING

5.2.1 Active layer materials

5.2.1.1 Materials selection and benchmarking

Figure XXX (figura que estarà a la part de material and methods. Com la figura 1 (a) del paper) shows the chemical structure of the materials serving as electron-donors (D18[70, 71] PTQ10[72, 73] and PM6[41, 40]) and electron-acceptors (O-IDFBR,[74, 75, 76] PMI-FF-PMI[57], and IO-4Cl[10, 70, 39]) used as components in the different active layers. The chosen materials are all wide band-gap materials, with E_{bg} between 1.78 and 2.07 eV (\approx 700 and 600 nm, respectively) as discussed in Section 5.2.1.3.

The reader is referred to Section 5.2.1.3 for the optical properties of the selected materials.

The main goal of this combinatorial screening study was to test novel donor:acceptor materials combinations in order to find promising wide E_{bg} candidates. D18 was chosen as a donor with relatively wide E_{bg} , which has shown a high efficiency of nearly 18% when blended with the benchmark non-fullerene acceptor Y6.[71, 77] Hofinger et al. also demonstrated that D18:Y6 cells exhibit a low $\Delta V_{oc}^{\text{total}}$ of 0.51 V with especially low $\Delta V_{oc}^{\text{nr}}$ of 0.20 V.[70] The donor polymer PTQ10 is a promising donor due to its low synthetic complexity and high efficiency, surpassing 16% when blended with Y6.[72, 78] The other donor material is PM6, whose efficiency when blended with Y6 can surpass 17%. [41, 42] It is the donor exhibiting the lowest band-gap, but it has already demonstrated very high efficiencies also for indoor applications, surpassing 26% when blended with IO-4Cl,[39] and reaching up to 36% in combination with Y6 and 2PACz.[50] PM6:IO-4Cl blend is used in this work as a reference therefore IO-4Cl is also included as NFA. PMI-FF-PMI is an NFA synthesized by J. Hofinger et al. which has shown V_{oc} over 1.4 V when blended with D18 and deposited by spin-coating. Therefore, this blend possesses one of the highest V_{oc} reported in organic solar cells, with an efficiency of 5.34%. [57] The third NFA used is O-IDFBR, first synthesized by Baran et al. in 2017, achieving an efficiency of 11% in a ternary blend with PCE10 and O-IDTBR.[75] Afterwards, few studies address this

The donor PCE10 is also known as PTB7-Th or PBTTT-EFT

NFA.[79, 74, 76] To the best of our knowledge, most of the tested donor:acceptor combinations have not been explored in literature. The only two exceptions are PM6:IO-4Cl and D18:PMI-FF-PMI, as shown in [Table 5.1](#).

	PTQ10	D18	PM6
IO-4Cl	*	*	[39, 40]
O-IDFBR	*	*	*
PMI-FF-PMI	*	[57]	*

Table 5.1: State of the art of the wide E_{bg} blends explored. To the best of our knowledge, * denotes donor:acceptor combinations which are not explored in literature

5.2.1.2 Fabrication

The materials and methods section (??) presents the solar cell fabrication process within the NANOPTO group. Nevertheless, we describe the active layer composition and fabrication which are essential for this chapter because of the number of conditions tested.

Each donor:acceptor combination was prepared from chlorobenzene (CB) and chloroform (CF) solutions separately, therefore giving a total of $3 \times 3 \times 2 = 18$ different solutions and active layers. The solutions were prepared in a 1:1.5 donor:acceptor ratio except for the case of PMI-FF-PMI solutions, where the donor:acceptor ratio was 1:1 according to [57]. Almost all active layer materials were dissolved attaining the same concentration of 20 mg/mL, irrespective of the solvent. D18-based solutions were diluted down to 10 mg/mL due to their observed high viscosity at 20 mg/mL. The solutions were maintained in continuous stirring at 40°C and 80°C for CF and CB, respectively, for a minimum of 4 h to ensure proper dissolution of the solutes. The active layers were deposited via blade-coating with a velocity varying from 90 mm/s to 10 mm/s along the substrate, achieving a thickness gradient from 200 to 50 nm, approximately.[74]

[Figure 5.1](#) contains images of all 18 substrates prepared, showing the thickness gradient along the samples. It is interesting to see the variety of colors of the active layers even though all its components have similar E_{bg} . The color perceived by the human eye is mainly affected by the spectrum reaching the eye between 400 and 700 nm.[80] Therefore, we attribute the different colors to the fact that the E_{bg} of the materials is in between 600 and 700 nm, where small differences in E_{bg} and absorption spectrum shape strongly impact the perceived color. These color differences are also interesting to consider for applications

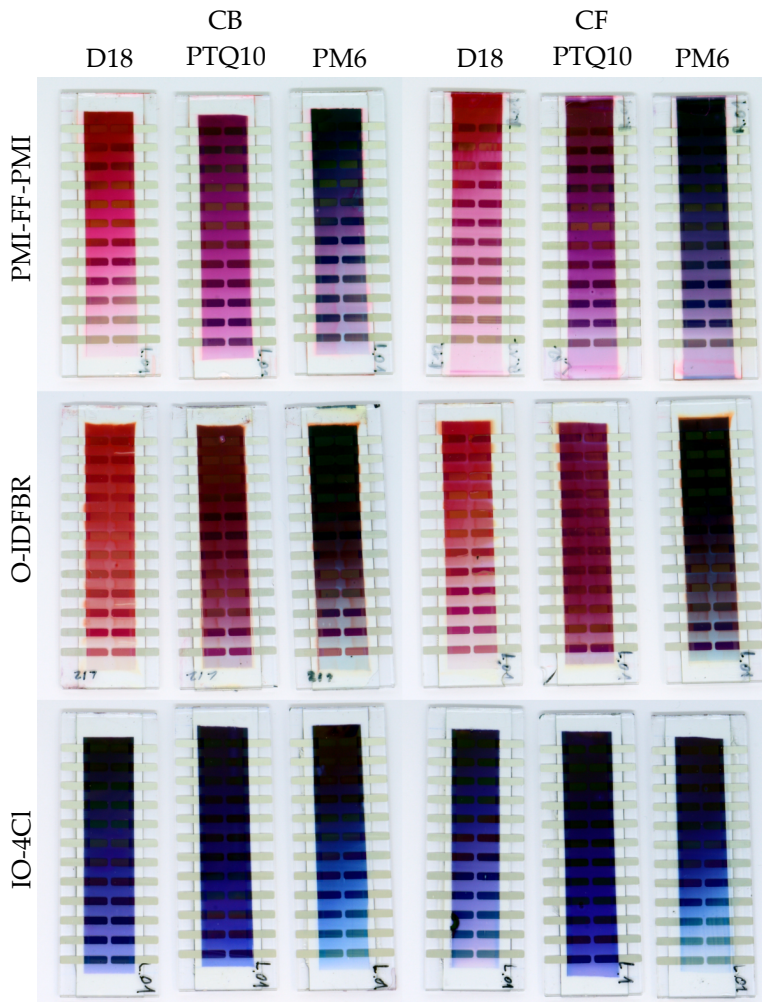


Figure 5.1: Photographs of all 18 samples prepared in the wide E_{bg} combinatorial screening. The color gradient in each sample corresponds to the thickness gradient of the active layer. The different colors of different active layers denote the different band-gaps and absorption profiles of donors and acceptors used.

like semi-transparent OPV, where color is meaningful.

5.2.1.3 Optical properties

Figure 5.2 shows the HOMO and LUMO energy levels for the active layer materials. The values correspond to cyclic voltammetry (CV) measurements taken from literature [39, 72, 75, 77] except for the case of PMI-FF-PMI, whose literature energetic levels were measured using electrochemical voltage spectroscopy (EVS).[57] According to

the HOMO and LUMO levels, all donor-acceptor combinations form staggered (type-2) hetero-junctions (i.e. $\text{LUMO}_{\text{donor}} > \text{LUMO}_{\text{acceptor}} > \text{HOMO}_{\text{donor}} > \text{HOMO}_{\text{acceptor}}$) meaning that they could work as organic solar cells. Additionally, due to the similar E_{bg} between all materials, the difference between $\text{HOMO}_{\text{donor}}$ and $\text{HOMO}_{\text{acceptor}}$ (ΔHOMO) as well as the difference between $\text{LUMO}_{\text{donor}}$ and $\text{LUMO}_{\text{acceptor}}$ (ΔLUMO) lay between 0.2 and 0.4 eV, being similar offsets compared to the standard value of 0.3 eV for efficient exciton dissociation.[63] Note that, some materials have, however, shown high efficiencies (and therefore efficient enough exciton dissociation) with ΔHOMO or ΔLUMO lower than 0.3 eV.[45, 41, 81] It is worth mentioning that since we have both donor and acceptor materials with similar E_{bg} , a low ΔHOMO implies a low ΔLUMO (and vice-versa). This is not the case for most of the literature works that study small ΔHOMO or ΔLUMO , for which, to achieve a broad absorption spectrum, the materials composing the active layer are chosen to absorb in different regions of the solar spectrum (i.e., significantly different E_{bg}).

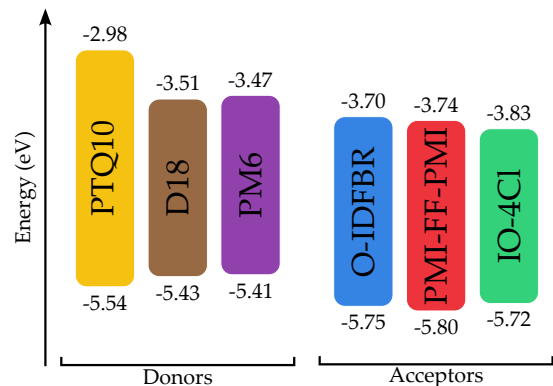


Figure 5.2: HOMO and LUMO energy levels of the materials selected for the wide E_{bg} combinatorial screening. The energetic levels values are taken from references [39, 72, 75, 77, 57] and are measured by cyclic voltammetry except for the acceptor PMI-FF-PMI that was measured by electrochemical voltage spectroscopy.

Additionally, all six materials were characterized with ellipsometry in order to assess their refractive index, n , and extinction coefficient, k , (Figure 5.3). From the measured k , we have inferred the band-gap energy (E_{bg}) of each material as the inflection point of the extinction coefficient edge. Table 5.2 shows the resulting E_{bg} . Additionally, E_{bg} can also be calculated from the difference between the HOMO and LUMO values shown in Figure 5.2. Table 5.2 shows a comparison between both methodologies to measure E_{bg} . In that comparison, one can see that the PTQ10 has an exceptionally high HOMO-LUMO difference

compared to the E_{bg} value calculated from k . The latter suggests that the reported LUMO for PTQ10 may be overestimated or that PTQ10 aggregation in the solid film significantly affects its LUMO energy (through the gas-to-solid shift). The same comparison for the other materials yields percentage differences lower than 7.5%, indicating a better agreement between the reported HOMO and LUMO energy levels and the measured extinction coefficient, k .

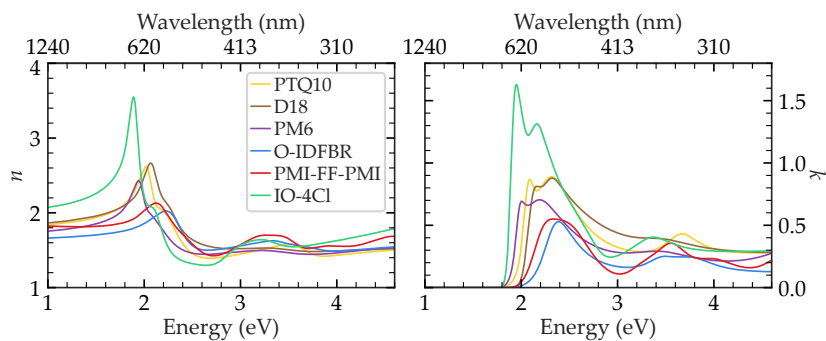


Figure 5.3: Refractive index n and extinction coefficient k of the wide E_{bg} donors and acceptors. n and k measured via ellipsometry by Ms. Arianna Quesada-Ramírez are plotted against energy in the bottom axis, and the corresponding wavelengths are shown in the top axis.

Material	E_{bg} (eV)		Difference	
	Ellipsometry	HOMO-LUMO	(eV)	(%)
D18	2.064	1.92	-0.144	-6.977
PTQ10	2.010	2.56	0.550	27.363
PM6	1.935	1.94	0.005	0.258
O-IDFBR	2.221	2.05	-0.170	-7.699
PMI-FF-PMI	2.127	2.06	-0.067	-3.150
IO-4Cl	1.888	1.89	0.002	0.106

Table 5.2: Comparison of E_{bg} of materials measured with different methods. Energy band gap of active layer materials calculated as the inflection point of the extinction coefficient (k) measured with ellipsometry (E_{bg}^k) compared to the difference between LUMO and HOMO found in literature (Figure 5.2). The last two columns correspond to the difference between the two E_{bg} values in absolute and percentual values concerning the ellipsometric measurement.

5.2.1.4 Morphology-related aspects

The morphology of the active layer is a key parameter to achieve the best possible performance for any blend. There are many parameters

related to device fabrication that can affect the active layer morphology: deposition technique, deposition temperature, or annealing conditions are just a few examples. Among them, the solvent is one of the most important because it directly affects the drying dynamics of the film during deposition. For example, a solvent with a higher boiling point, such as chlorobenzene (CB), will give more time to donor and acceptor molecules to reorder before drying, typically resulting in more ordered films. On the contrary, a solvent with a lower boiling point, such as chloroform (CF), will tend to evaporate faster, quenching the disordered wet film and typically resulting in more amorphous domains. The different solubility of active layer components with the solvent is also an important factor during the formation of the thin film, which directly relates to the final morphology.

In order to evaluate the effect of the solvent on the morphology of PTQ10:O-IDFBR active layer we measured grazing incidence wide angle X-ray scattering (GIWAXS) with the help of Dr. Matteo Sanviti and Dr. Jaime Martín from Universidade da Coruña. We blade-coated O-IDFBR, PTQ10, and PTQ10:O-IDFBR films from CF and CB on silicon substrates. The results of the GIWAXS measurements performed by our collaborators are shown in [Figure 5.4](#). PTQ10 exhibits a stronger crystalline signal when deposited from CB, due to the higher boiling point of the solvent. For O-IDFBR, there is no significant difference between CF and CB GIWAXS patterns. For the blend film, CB processing leads to higher long-range order than CF. This agrees with the previously discussed role of solvent evaporation during the drying of the film. As we will show below, for PTQ10:O-IDFBR, the best performance is achieved with CB, which shows higher structural order than CF in its GIWAXS data. The latter is also in agreement with the previous assumption that the ideal morphology for any organic solar cell active layer is closer to the crystalline donor and acceptor domains rather than amorphous.

The same characterization was done for the blend PTQ10:IO-4Cl. The GIWAXS patterns ([Figure 5.5](#)) suggest packing motifs where NFA molecules pack into 1D-chain or multidimensional mesh-like structures.[\[82, 83\]](#) Because 1D- or mesh-like packing motifs feature continuous aromatic structures that are separated by aliphatic domains, many large d-spacing symmetry planes exist, which are expected to give rise to multiple diffraction peaks in the low-q region, as found in our patterns.[\[82, 83, 84\]](#) Nevertheless, when IO-4Cl is blended with PTQ10, these reflections vanish and only the reflection from the lamellar-like packing of PTQ10 is observed. On the other hand, IO-4Cl deposited from CF shows a less defined (broader) GIWAXS signal, indicating less ordered crystalline domains. Nevertheless, the

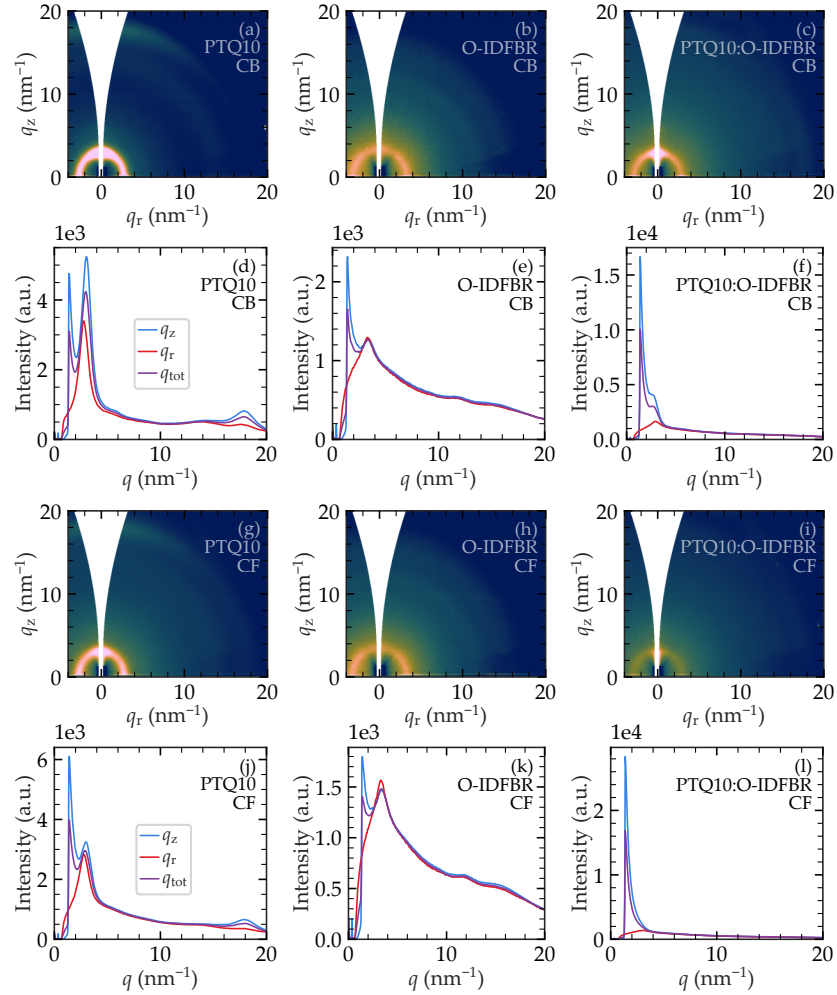


Figure 5.4: GIWAXS results for PTQ10:O-IDFBR material system deposited from CB and CF. (a)-(c) and (g)-(h) are the diffractograms for the neat materials and the blends. (d)-(f) and (i)-(k) are their corresponding in-plane (q_r , red), out of plane (q_z , blue), and total (q_{tot} , purple) integrated intensities.

blend shows a GIWAXS signal preserving both donor and acceptor separately, indicating that both PTQ10 and IO-4Cl have a certain degree of crystallinity. Therefore, the assumption is also true since the blend with higher structural order (in this case deposited from CF) shows higher efficiency (see below).

The d-spacing, d , and the coherence length, L_c , were collected for all the samples from the 1D integrations of the GIWAXS diffractograms shown in Figure 5.4 and Figure 5.5. Table 5.3 summarizes lamellar

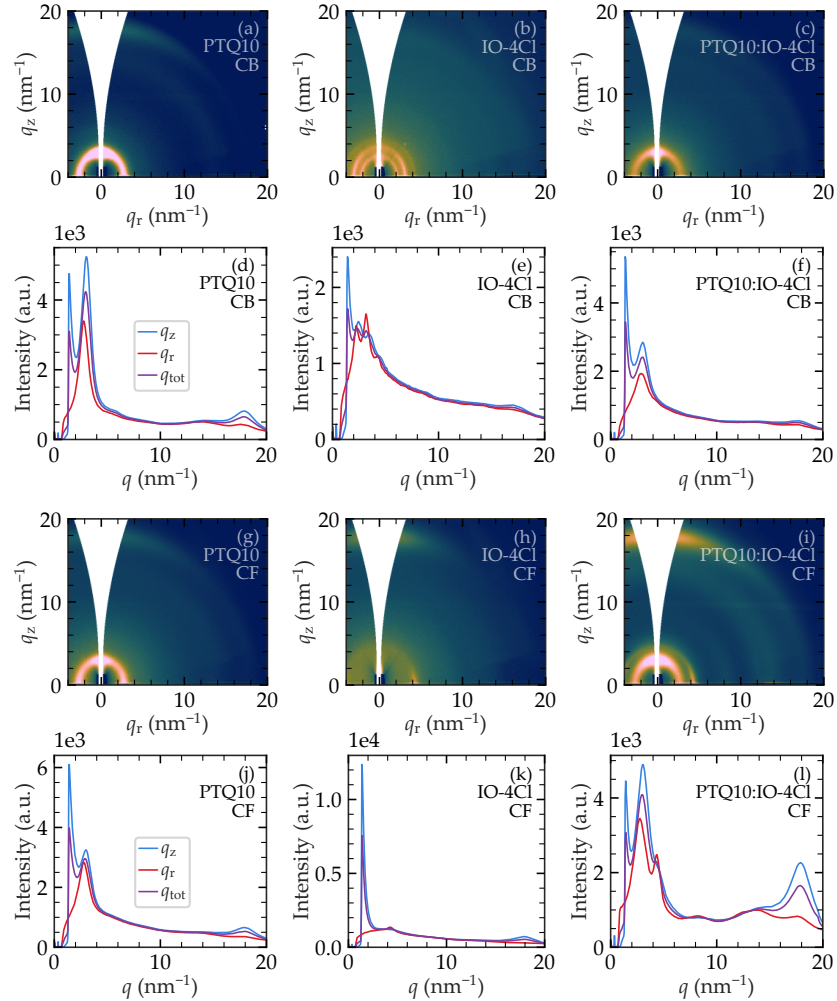


Figure 5.5: GIWAXS results for PTQ10:IO-4Cl material system deposited from CB and CF. (a)-(c) and (g)-(h) are the diffractograms for the neat materials and the blends. (d)-(f) and (i)-(k) are their correspondings in-plane (q_r , red), out of plane (q_z , blue), and total (q_{tot} , purple) integrated intensities.

stacking of the polymer donor, (100) planes, and other contributions, such as $\pi - \pi$ stacking (010) as well as characteristic peaks from the acceptors at lower q values. Compared to the pure donor, the (100) planes of the blends seem to shift towards lower d values. Nevertheless, no direct correlation of such information with structural changes can be directly pointed out since the contribution from the acceptor at lower q can alter the peak position. Thus, it is hard to give reliable assessments of structural changes of donor domains in the blend compared to the

pure donor film.

Sample	Solvent	(100)		(010)		low q					
		d (nm)	L_c (nm)								
PTQ10	CB	2.25	5.79	0.35	2.46						
	CF	2.24	5.48	0.35	2.49						
O-IDFBR	CB					1.90	6.44				
	CF					1.89	6.45				
PTQ10:O-IDFBR	CB	2.13	5.76	0.36	1.99						
	CF	2.09	4.46	-	-						
IO-4Cl	CB			0.38	6.13	2.78	20.44	1.99	8.87	1.49	4.88
	CF			0.35	3.25					1.49	10.91
PTQ10:IO-4Cl	CB	2.15	5.15	0.36	4.78						
	CF	2.07	5.76	0.35	3.07					1.46	14.82

Table 5.3: d-spacing (d) and coherence length (L_c) analysis for (100), (010) planes, and low q region. Data was calculated from GIWAXS diffractograms shown in Figure 5.4 and Figure 5.5.

In conclusion, the performance differences between CF- and CB-processed blends arise from their different microstructures. Additionally, the results show that the optimization of the latter cannot be predicted from the solvent choice because there is no clear tendency of one solvent to achieve better performance devices than the other for specific materials. This suggests that the boiling point is not the only parameter playing a role and other properties like solubility are also important.[PTroshin2009, DCorzo2023]

5.2.2 $J - V$ characterization

All cells (24) for each of the 18 samples shown in Figure 5.1 were characterized by measuring their $J - V$ curve under a Xenon arc-lamp solar simulator. The latter can be done easily and rapidly thanks to the Pika demultiplexer developed by Dr. Martí Gibert-Roca and shown previously in ???. In this section, we discuss these results by analyzing the dependence of V_{oc} , J_{sc} , FF , and PCE on active layer composition. Figure 5.6 shows an example of the power conversion efficiency (PCE) dependence on thickness from the described measurement on the sample of PTQ10:O-IDFBR deposited from the CB solution. Not all 24 devices were completely operative. In this case, there were discrepancies in the two replicas (right and left) of cells number 1, 3, 11, and 12. Nevertheless, it is easy to recognize thickness-dependent tendencies. In all cases, the best cell considered for each material and solvent

The Pika demultiplexer reduces up to 90% the time spent in characterization.[36]

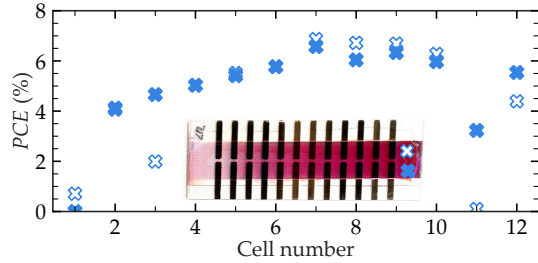


Figure 5.6: Dependence of PCE on active layer thickness. Power conversion efficiency (PCE) as a function of the cell pixel number (i.e., thickness) for a PTQ10:O-IDFBR cell deposited from chlorobenzene solution. The inset shows the substrate with a thickness gradient achieved by varying blade-coater speed. In the plot, thickness is increasing from cell number 1 to 12.

combination was the one with the highest PCE within the thickness range, with its replica having a similar efficiency value. Therefore, we can say that the thickness is an optimized parameter. Table 5.4 shows the figures-of-merit (FoM) of the best-performing devices. Additionally, Figure 5.7 shows the $J - V$ curves from the best-performing cells of each material (donors and acceptors) as an example of some of the best-performing cells of the combinatorial screening study.

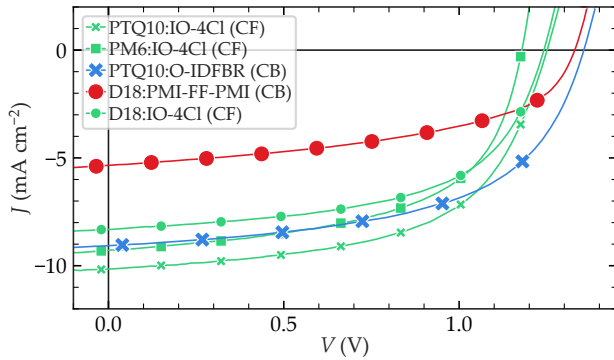


Figure 5.7: $J - V$ curves of the best performing cells for each of the six materials tested (donors and acceptors). The corresponding figures of merits of the measurements can be found at Table 5.4 marked with *.

Donor	Acceptor	Solvent	V_{oc} (V)	J_{sc} (mA/cm ²)	FF (%)	PCE (%)
PTQ10	O-IDFBR	CF	1.33	8.05	50.85	5.44
PTQ10	O-IDFBR*	CB	1.35	9.06	56.05	6.87
PTQ10	PMI-FF-PMI	CF	1.38	3.63	39.52	1.98
PTQ10	PMI-FF-PMI	CB	1.36	1.70	37.80	0.87
PTQ10*	IO-4Cl*	CF	1.25	10.16	57.51	7.31
PTQ10	IO-4Cl	CB	1.22	8.09	56.37	5.55
D18	O-IDFBR	CF	1.29	5.16	47.08	3.15
D18	O-IDFBR	CB	1.33	3.92	50.49	2.62
D18	PMI-FF-PMI	CF	1.28	5.81	42.26	3.14
D18	PMI-FF-PMI*	CB	1.33	5.35	49.49	3.53
D18*	IO-4Cl	CF	1.24	8.32	57.13	5.91
D18	IO-4Cl	CB	1.21	8.13	51.85	5.10
PM6	O-IDFBR	CF	1.23	5.93	41.02	2.99
PM6	O-IDFBR	CB	1.24	4.91	48.95	2.98
PM6	PMI-FF-PMI	CF	1.26	2.20	43.07	1.19
PM6	PMI-FF-PMI	CB	1.26	2.48	52.49	1.64
PM6*	IO-4Cl	CF	1.18	9.29	57.03	6.23
PM6	IO-4Cl	CB	1.15	9.00	58.18	6.02

Table 5.4: Figures-of-merit from $J - V$ measurements. $J - V$ curves results of the best-performing devices for each combination tested. The * indicates the best-performing device for each of the tested active layer materials, which $J - V$ curves are shown in [Figure 5.7](#).

5.2.2.1 V_{oc} and PCE

The results of the best-performing devices shown in [Table 5.4](#) are summarized in [Figure 5.8](#), where the PCE for each donor-acceptor combination deposited from CB and CF solvents is plotted against their V_{oc} . The different colors (red, blue, and green) indicate the acceptor used (PMI-FF-PMI, O-IDFBR, and IO-4Cl, respectively). The colored ellipses are the central regions where the points of each cell with the same acceptor are located within a one standard deviation confidence range (σ). From these regions, it is clear that devices containing IO-4Cl achieve higher efficiencies but lower V_{oc} compared to O-IDFBR- and PMI-FF-PMI-based devices because the confidence ellipse is located more in the upper left part. Nevertheless, the PTQ10:O-IDFBR cells (both deposited from CF and CB) are an exception and, apart from being the only O-IDFBR devices with efficiencies comparable to those of IO-4Cl-based cells, its V_{oc} is among the highest measured in all combinations.

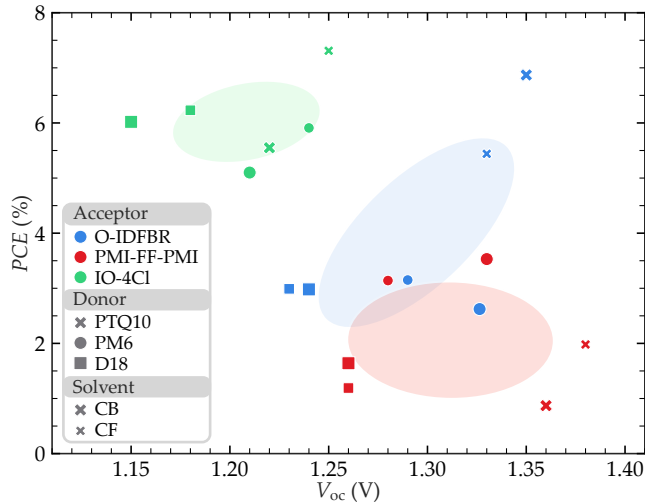


Figure 5.8: Best power conversion efficiency (PCE) values as a function of the corresponding V_{oc} achieved for each donor-acceptor-solvent combination. The 18 points are taken from a total of 432 devices where the thickness is optimized for each combination due to the thickness gradient. The colored ellipses represent confidence regions for the cells containing each acceptor with a σ confidence.

In Figure 5.8, another important tendency is that devices containing PTQ10 as the donor (cross-shaped points) achieve the highest V_{oc} observed for each acceptor. The latter is also shown in Figure 5.9, where V_{oc} is plotted as a heatmap for CF (a) and CB (b) processed blends. In Figure 5.9, all rows are darker in the PTQ10 column, indicating that PTQ10-based devices achieve always the highest V_{oc} regardless of acceptor material or solvent processing. That is the case for PTQ10:PMI-FF-PMI deposited from CF where the V_{oc} of 1.38 V is the highest achieved; for PTQ10:O-IDFBR blend deposited from CB with a V_{oc} of 1.35 V; as well as for the IO-4Cl:PTQ10 blend deposited from CF with a V_{oc} of 1.25 V. On the contrary, the lowest V_{oc} for each acceptor occurs always for devices containing PM6 (square shape points), with V_{oc} of 1.15 V, 1.23 V and 1.26 V when blended with IO-4Cl, O-IDFBR, and PMI-FF-PMI from CB, CF, and CF, respectively. Devices based on D18 as the donor show V_{oc} values in between those of PTQ10 and PM6-based solar cells.

The V_{oc} is directly related to the energetic difference between the $LUMO_{\text{acceptor}}$ and the $HOMO_{\text{donor}}$, therefore, when comparing blends with the same acceptor, the deeper the $HOMO_{\text{donor}}$, the higher the V_{oc} expected. This behavior agrees with the energy levels of the three donors shown in Figure 5.2, where the $HOMO$ level of PTQ10 and PM6 are the deepest and the shallowest, respectively. Notice that,

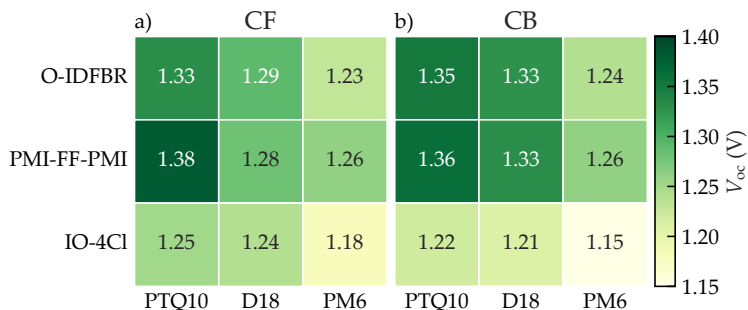


Figure 5.9: V_{oc} heatmap of all donor-acceptor-solvent combinations. The open circuit voltage of the best-performing devices deposited from CF (a) and the CB (b) is shown as a heatmap for each donor:acceptor combination.

in this simplified scenario, we are assuming that $\text{LUMO}_{\text{acceptor}}$ and $\text{HOMO}_{\text{donor}}$ do not depend on the materials blended, which may not be valid due to differences in morphology of donor and acceptor regions in the blend compared to pure material films as well as compared to the conditions where energetic levels were measured (typically in solution). We also assume that V_{oc} losses are equal for all blends, which may not be the case. When plotting the $\text{HOMO}_{\text{donor}}-\text{LUMO}_{\text{acceptor}}$ difference versus V_{oc} (Figure 5.10), we observe a strong linear correlation between both parameters with a slope near 1 and a high Pearson's correlation parameter ($r = 0.84$) indicating that this simplified scenario is valid, at least, for this study. Nevertheless, the difference in V_{oc} between CF and CB processing of the same blend material cannot be explained by this simple model.

For most of the donor:acceptor combinations, there is no literature to benchmark our results, highlighting the novelty of the tested donor:acceptor combinations. Nonetheless, we obtained somewhat lower efficiencies for the few cases where data are available (see Table 5.5). For example, Y. Cui et al. reached 9.80% efficiency for PM6:IO-4Cl cells deposited from CB, with a V_{oc} of 1.24 V;[39] and Y. Yang et al. achieved 7.80% with a V_{oc} of 1.22 V for the same active layer material.[40] Nevertheless, when comparing these results to ours (PCE of 6.20% and V_{oc} of 1.15 V for PM6:IO-4Cl deposited from CB), it is important to consider that we are using the inverted architecture and depositing the active layer from blade-coating. The latter is compatible with industrial roll-to-roll fabrication needed for up-scaling organic solar cells. On the other hand, the benchmark works use spin-coating instead of blade-coating, which is not a roll-to-roll-compatible coating technique. Additionally, the benchmark works use the standard architecture differing from our inverted devices (i.e.,

different ETL, HTL and top electrode materials)

Ref.	Active layer		Device geometry	Deposition technique	V_{oc} (V)	J_{sc} (mA/cm ²)	FF (%)	PCE (%)	Area (cm ²)
	Donor	Acceptor							
[39]	PM6	IO-4Cl	Normal	Spin-coating	1.24	11.6	68.10	9.80	1
[40]	PM6	IO-4Cl	Normal	Spin-coating	1.22	10.42	61.56	7.80	0.04
*	PM6	IO-4Cl	Inverted	Blade-coating	1.15	9.00	58.18	6.02	0.08
[57]	D18	PMI-FF-PMI	Normal	Spin-coating	1.41	6.09	60.9	5.34	0.1
*	D18	PMI-FF-PMI	Inverted	Blade-coating	1.33	5.35	49.49	3.53	0.08

Table 5.5: Benchmark of PM6:IO-4Cl and D18:PMI-FF-PMI active layer systems. Benchmark with literature for solar cells made with PM6:IO-4Cl and D18:PMI-FF-PMI deposited from CB as active layer materials. * in the reference column indicate the devices in this work.

At this point, we want to comment on the IO-4Cl devices, which are the more efficient cells in the combinatorial screening study. We tested two different batches of IO-4Cl material bought from the same provider. The results for the first tested batch of IO-4Cl are shown in Figure 5.11. In that case, the efficiency of the best devices did not exceed 5%. Furthermore, these results correspond to the best cells of a long optimization process where different processing conditions, such as donor:acceptor ratio, co-solvent addition, or ETL materials were optimized. In contrast, the second IO-4Cl batch tested improved all

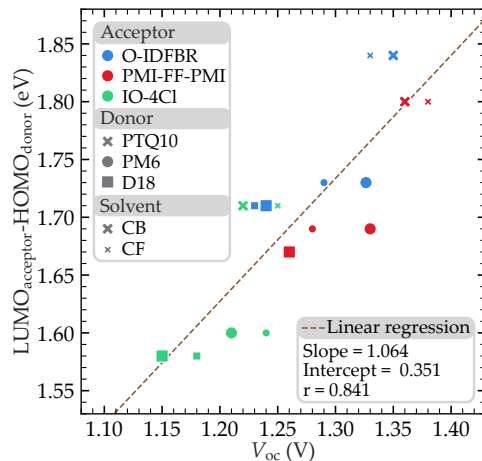


Figure 5.10: Energy difference between LUMO_{acceptor} and the HOMO_{donor} as a function of V_{oc} . The data points fit a linear regression with a slope of 1.06, suggesting the direct relation between the LUMO_{acceptor} – HOMO_{donor} difference and the V_{oc} . The high Pearson’s correlation coefficient ($r = 0.84$) is also a sign of the strong correlation between the two parameters.

the previous cells on the first try with the conditions described in the experimental section (i.e., without further optimization), exceeding 5% when blended with all three donors regardless of the CB or CF solvent. With this insight, we want to highlight the importance of repeatable material fabrication processes for improved batch-to-batch repeatability. Furthermore, this is highly relevant for the commercialization of organic solar cell technologies.

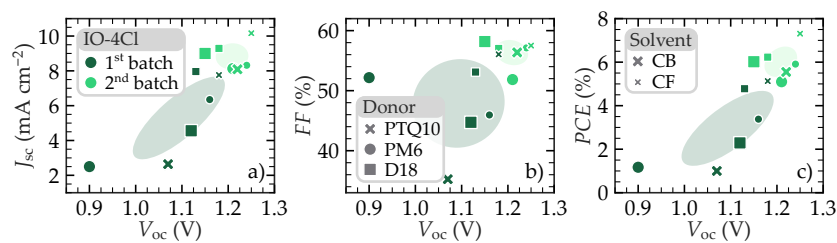


Figure 5.11: $J - V$ measurements results for the two IO-4Cl batches used. PCE (a), J_{sc} (b), and FF (c) as a function of V_{oc} for two different IO-4Cl batches. The performance of the 2nd batch (light green) is much better than the first although both are bought from the same provider. The 2nd batch corresponds to the IO-4Cl used in the combinatorial screening study.

The other combination found in the literature is D18:PMI-FF-PMI. J. Hofinger et al. achieved a PCE of 5.34% with a V_{oc} of 1.41 V.[57] These values are considerably higher than our results ($PCE = 3.53\%$ and $V_{oc} = 1.33\text{ V}$). In this case, the reference work also used the standard architecture and deposited the active layer by spin-coating compared to our blade-coated inverted devices. Table 5.5 shows a comparison of our devices with the benchmark works, where it can be seen that all the $J - V$ FoM are responsible for the efficiency difference between our devices and the literature.

Owing to the important differences in device architecture between this study and the benchmark results, it is also worth comparing with the typical values obtained in our group. For example, FF is typically the weaker point of our cells, with typical values between 50 and 60%. J_{sc} is also a weak point, usually approximately 10% lower than that of the state-of-the-art. In contrast, the V_{oc} that we obtain is generally in better concordance with the reported state-of-the-art cells. Considering this and looking at Table 5.5, we can say that FF and J_{sc} are inside the expected values according to our experience. Nevertheless, V_{oc} is lower than what we would expect, which suggests that there is still room for improvement in all combinations to achieve higher PCE by improving the V_{oc} .

5.2.2.2 FF and J_{sc}

The PCE values are spread in a large range of almost one order of magnitude, from 0.82% for PTQ10:O-IDFBR in CB to 7.31% for PTQ10:IO-4Cl in CF. Nevertheless, not all figures of merit exhibit such large variations. For example, the fill factor (FF), shown as a function of V_{oc} in Figure 5.12, varies between 40 and 60% without a clear correlation with V_{oc} . IO-4Cl-based devices show a FF which is independent of the V_{oc} while O-IDFBR and PMI-FF-PMI show a positive and a negative correlation, respectively.

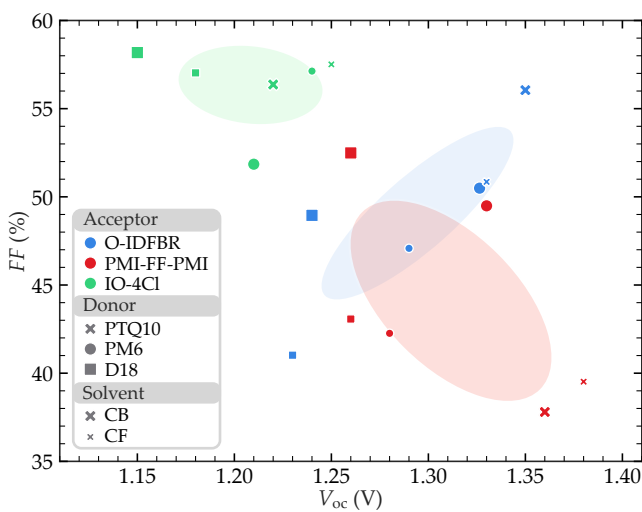


Figure 5.12: FF vs. V_{oc} for the 18 best-performing devices of the combinatorial screening. The coloured ellipses represent confidence regions for the cells containing each acceptor with a σ confidence.

The parameter which has the highest change and therefore affects more the PCE is the J_{sc} . Figure 5.13 (a) shows that J_{sc} varies almost one order of magnitude, between 1.35 mA/cm^2 and 10.16 mA/cm^2 (Figure 4 (a)). Similar to the PCE s, the cells based on IO-4Cl as acceptor have the highest J_{sc} compared to PMI-FF-PMI and O-IDFBR devices. In other words, for every donor (different data-point shape in Figure 5.13 (a)) the cell containing IO-4Cl has the highest J_{sc} . The latter is in agreement with the extinction coefficients Figure 5.3, which show that IO-4Cl is the acceptor with the highest k at its absorption peak and, at the same time, the acceptor with the lowest energy band-gap (E_{bg}), being about 0.4 eV lower than O-IDFBR and PMI-FF-PMI. The latter is also highlighted in Figure 5.13 (b), where EQE_{PV} from IO-4Cl devices with the different donors (green lines) show a similar optical E_{bg} , while the others containing O-IDFBR (blue) and PMI-FF-PMI (red) have a higher

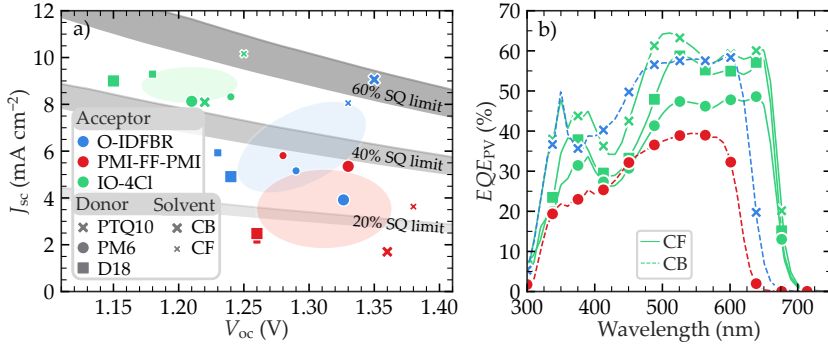


Figure 5.13: J_{sc} results. (a) J_{sc} as a function of V_{oc} for the best-performing cells of each donor-acceptor-solvent combination. The colored ellipses represent confidence regions for the cells containing each acceptor with a 1σ confidence. Fractions (60, 40, and 20%) of the Shockley-Queisser are plotted considering a E_{bg} of $V_{oc} + \Delta V_{oc}^{\text{total}}$ with $0.6 < \Delta V_{oc}^{\text{total}} < 0.7$ eV. (b) External quantum efficiency (EQE_{PV}) for some of the best-performing cells.

E_{bg} than the IO-4Cl devices containing the same donor.

Although small, the E_{bg} difference between acceptors is in the spectral region where the flux of photons is the highest in all solar spectrum. Therefore, a small E_{bg} difference can make an important impact on the overall J_{sc} . This effect is clearly demonstrated by the Shockley-Queisser (SQ) limit, in which the EQE_{SQ} is considered to be zero for photons with energy lower than the E_{bg} and 100% for energies equal or higher than E_{bg} . However, the SQ limit assumes ideal, perfect absorption, exciton separation, and free-charge carrier transport to the contacts within the solar cells. The latter results in a J_{sc} decrease when increasing E_{bg} . For comparison, Figure 5.13 (a) also shows different fractions (60, 40, and 20%) of the SQ limit (grey areas) considering a total voltage loss of $\Delta V_{oc}^{\text{total}} = 0.6$ V (upper limit) and $\Delta V_{oc}^{\text{total}} = 0.7$ V (lower limit), with $E_{bg} = qV_{oc} + \Delta V_{oc}^{\text{total}}$. The IO-4Cl devices lay between 60 and 40% of the SQ limit, while O-IDFBR and PMI-FF-PMI devices (except for the PTQ10:O-IDFBR) have a J_{sc} between 40 and 20% of the SQ limit, in some cases even lower. This indicates that the decrease in J_{sc} is not only related to an increase in the E_{bg} , which would be related to absorption losses as described by the SQ limit, but also to a worse exciton separation and/or free-charge carrier extraction. Only PTQ10:O-IDFBR cells have a SQ limit J_{sc} percentage similar to PTQ10:IO-4Cl in CF, which indicates that the J_{sc} difference between those two cells is the expected from its E_{bg} difference. Nevertheless, the J_{sc} of the best devices being inside the 60% range shows that there is still room for improvement.

5.2.3 V_{oc} loss analysis

In general, the total voltage loss ($\Delta V_{\text{oc}}^{\text{total}}$) is defined as the energy difference between the E_{bg} of the solar cell and the measured open-circuit voltage (V_{oc}) under AM1.5G illumination, therefore given by $\Delta V_{\text{oc}}^{\text{total}} = E_{\text{bg}}/q - V_{\text{oc}}$. E_{bg} is the optical band-gap of the cell, which can be defined in different ways, but typically, it is calculated as the inflection point of the EQE_{PV} edge. The V_{oc} is proportional to the natural logarithm of the ratio between the short-circuit current (J_{sc}) and the dark current (J_0). The latter can be further divided into four quotients to give:[61]

$$V_{\text{oc}} = \frac{k_{\text{B}}T}{q} \ln \left(\frac{J_{\text{sc}}}{J_0} \right) = \frac{k_{\text{B}}T}{q} \ln \left(\frac{J_{\text{sc}}^{\text{SQ}}}{J_0^{\text{SQ}}} \frac{J_{\text{sc}}}{J_{\text{sc}}^{\text{SQ}}} \frac{J_0^{\text{rad}}}{J_0} \right) \quad (5.1)$$

Here $J_{\text{sc}}^{\text{SQ}}$ and J_0^{SQ} correspond to the short-circuit and the saturation current density in the Shockley-Queisser limit, respectively, and J_0^{rad} corresponds to the saturation current density in the radiative limit. [Equation 5.1](#) can be rewritten as a sum of four terms:

$$V_{\text{oc}} = V_{\text{oc}}^{\text{SQ}} - \Delta V_{\text{oc}}^{\text{sc}} - \Delta V_{\text{oc}}^{\text{r}} - \Delta V_{\text{oc}}^{\text{nr}} \quad (5.2)$$

Each term on the right side of [Equation 5.2](#) has a different physical meaning.[61] The first term corresponds to the V_{oc} at the SQ limit ($V_{\text{oc}}^{\text{SQ}}$). The difference between E_{bg} and $V_{\text{oc}}^{\text{SQ}}$ is understood as a thermodynamical loss due to the difference in solid angles between the incoming light and the radiation emitted by the cell as a black body, also known as *étiende* expansion.[85] The latter can be mitigated theoretically by equalizing both solid angle values, which can be done by sunlight concentration or by forcing the radiative emission to be at the same angle as the incoming light. We expect this difference to be constant in our cells since they have similar E_{bg} and we took all the measurements at the same temperature and light concentration conditions.

The short-circuit loss term ($\Delta V_{\text{oc}}^{\text{sc}}$) in [Equation 5.2](#) corresponds to the difference between the measured J_{sc} and the SQ value, $J_{\text{sc}}^{\text{SQ}}$. The main origin of this difference is the fact that the EQE_{SQ} is considered 100% for photons with energy higher than the E_{bg} , i.e., each photo-generated electron-hole pair is collected at the cell contacts. Nevertheless, this is never the case in a real cell, and the maximum EQE_{PV} is below 100%. Since J_{sc} is rarely lower than 10% of the $J_{\text{sc}}^{\text{SQ}}$, this loss is typically low. On the other hand, the radiative voltage loss ($\Delta V_{\text{oc}}^{\text{r}}$) in [Equation 5.2](#) can be more important. The latter is related to the energy difference between the emission peak and the E_{bg} of the cell. Even a small energy difference can result in a value of hundreds of millivolts. This is due to the exponential energy dependence of the spectrum emitted by the

solar cell. The last term in [Equation 5.2](#) is the non-radiative voltage loss ($\Delta V_{\text{oc}}^{\text{nr}}$) which is the difference between the measured V_{oc} and the V_{oc} at the radiative limit, V_{oc}^{r} . $\Delta V_{\text{oc}}^{\text{nr}}$ considers all losses due to non-radiative recombination mechanisms such as trap-assisted (Shockley-Read-Hall) recombination.

For the V_{oc} losses analysis, $V_{\text{oc}}^{\text{SQ}}$, $\Delta V_{\text{oc}}^{\text{sc}}$, and $\Delta V_{\text{oc}}^{\text{r}}$ were calculated using the current densities calculated as follows:

$$J_{\text{sc}}^{\text{SQ}} = q \int EQE_{\text{SQ}}(E) \varphi_{\text{AM1.5G}}(E) dE \quad (5.3)$$

$$J_{\text{sc}} = q \int EQE_{\text{PV}}(E) \varphi_{\text{AM1.5G}}(E) dE \quad (5.4)$$

$$J_0^{\text{SQ}} = q \int EQE_{\text{SQ}}(E) \varphi_{\text{BB}}(E) dE \quad (5.5)$$

$$J_0^{\text{rad}} = q \int EQE_{\text{PV}}(E) \varphi_{\text{BB}}(E) dE \quad (5.6)$$

Here $\varphi_{\text{AM1.5G}}$ and φ_{BB} are the 1-sun and black-body spectrum respectively. In the definition of φ_{BB} , we are considering the geometry of our solar cells, i.e., the active layer only emits to its front side due to the Ag electrode acting as a back reflector.[\[86\]](#) The Shockley-Queisser limit is well-known and studied, with values ($V_{\text{oc}}^{\text{SQ}}$, $J_{\text{sc}}^{\text{SQ}}$, FF^{SQ} , and PCE^{SQ}) being tabulated elsewhere.[\[86\]](#) Therefore, the calculation of $V_{\text{oc}}^{\text{SQ}}$ is a good opportunity to double-check the methodology used for calculating the different current density terms.

The Shockley-Queisser EQE (EQE_{SQ}) is a step-function that is 1 and 0 above and below E_{bg}

The integral for the determination of J_0^{rad} ([Equation 5.6](#)) is dominated by the lower energy tail of the EQE_{PV} spectrum due to the exponential nature of the black-body spectrum (φ_{BB}).[\[70, 87, 64\]](#) Therefore, to achieve a reliable J_0^{rad} value, one needs a highly sensitive EQE_{PV} with several orders of magnitude. The standard EQE_{PV} characterization (used in the cells of this section of the thesis) comprising an arc-lamp light source and a monochromator is not enough for the proper characterization of V_{oc} losses. For this reason, we need to improve the dynamic and spectral range of the measured EQE_{PV} . According to Rau,[\[87\]](#) the EQE_{PV} of a solar cell is equivalent to the quotient between the electroluminescence quantum efficiency (EQE_{EL}) and the black-body spectrum (φ_{BB}). EQE_{EL} is understood as the spectral distribution of the photons emitted by the cell when a current is applied to it. Its integral over the spectrum has to account for the total number of emitted photons per injected electron (expressed in %). This measurement is difficult to perform due to the challenge of collecting all emitted photons because their emission is generally omnidirectional. Nevertheless, assuming that the spectral shape is homogeneous in all directions and taking advantage of the relation between EQE_{EL} and

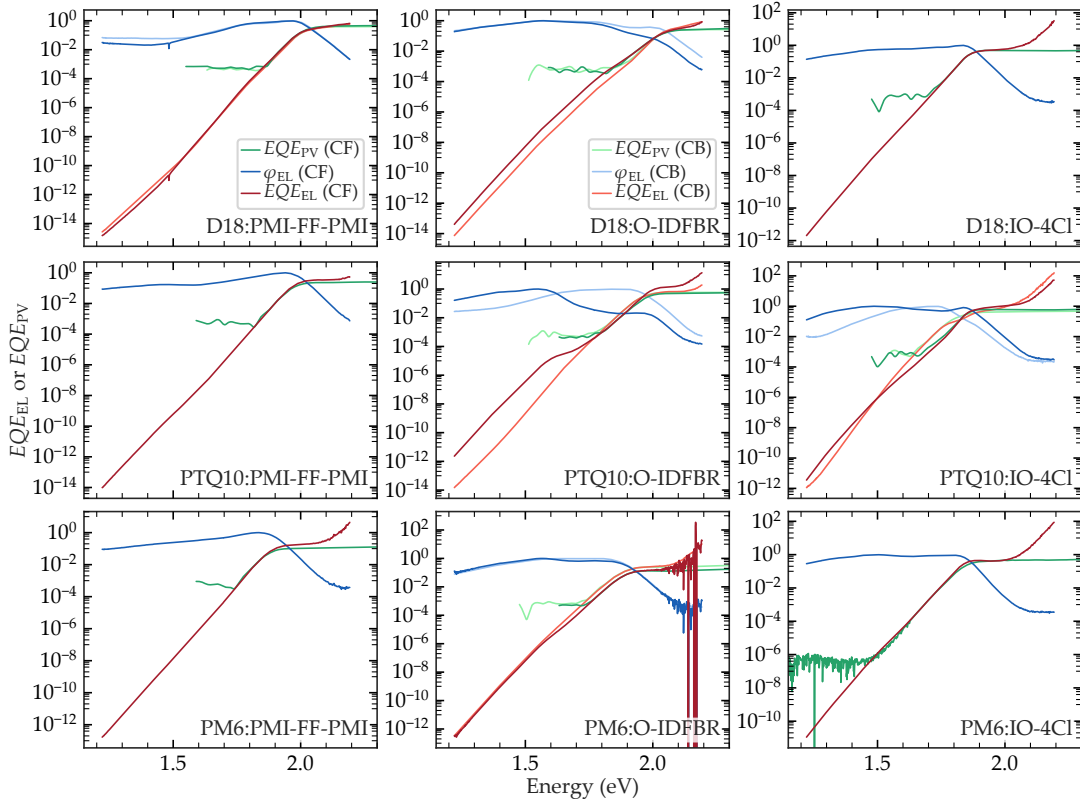


Figure 5.14: EL fits for extend the EQE_{PV} for V_{oc} losses calculations. The φ_{EL} divided by the φ_{BB} (red) is fitted to the EQE_{PV} (green) in low energy EQE_{PV} region where its edge shows a linear behaviour in the logarithmic scale. The plots also show the EL resulting from the fitted spectrum (blue). The light and dark colors stand for CF and CB processed devices respectively. The data from the blends D18:IO-4Cl, PTQ10:PMI-FF-PMI, PM6:PMI-FF-PMI and PM6:IO-4Cl prepared by CB is missing because they were not measured.

EQE_{PV} , we can assess EQE_{EL} by measuring the EL spectrum (φ_{EL}) and the EQE_{PV} . This is done by assuming that $EQE_{EL} = a \cdot \varphi_{BB}$, where a is a factor that is fitted to the relation between EQE_{PV} and EQE_{EL} :

$$EQE_{PV} = \frac{EQE_{EL}}{\varphi_{BB}} = \frac{a \cdot \varphi_{EL}}{\varphi_{BB}} \quad (5.7)$$

Figure 5.14 shows the EQE_{EL} (in blue) as well as the EQE_{PV} and the EQE_{EL}/φ_{BB} . The fitting of the factor a is done in the range where EQE_{PV} and φ_{EL} overlap. The latter occurs around the energy band gap of the material. The final extended EQE_{PV} used for the V_{oc} loss analysis is taken as EQE_{EL}/φ_{BB} for energies below the fit range, the measured EQE_{PV} for energies above the fit range and the average between EQE_{EL}/φ_{BB} and EQE_{PV} inside the fit range.

The non-radiative voltage loss term ($\Delta V_{\text{oc}}^{\text{nr}}$) was calculated as the difference between the radiative open-circuit voltage, V_{oc}^{r} , and the measured V_{oc} . V_{oc}^{r} is the sum of the first three terms on the right side of [Equation 5.1](#), which results in:

$$V_{\text{oc}}^{\text{r}} = \frac{k_{\text{B}}T}{q} \ln \left(\frac{J_{\text{sc}}}{J_0^{\text{rad}}} \right) \quad (5.8)$$

[Table 5.6](#) shows the J_{sc} and the J_0^{rad} resulting from the extended EQE_{PV} using [Equation 5.5](#) and [Equation 5.6](#). It is interesting to compare the measured and the calculated J_{sc} to see the accuracy of the EQE_{PV} measurement. The theoretical and the measured values are close in all cases except for the PM6:O-IDFBR blend processed from CF, where EQE_{PV} is lower than expected (see also the corresponding plot in [Figure 5.14](#)). This could be due to a bad measurement of that device or due to device degradation. [Table 5.6](#) also shows the calculated V_{oc}^{r} .

All values resulting from the V_{oc} loss analysis can be found at [Table 5.7](#), while [Figure 5.15](#) shows them in a bar plot manner. The overall voltage loss is around 0.6 to 0.7 V. Considering that voltage loss in literature lies between 0.5 and 0.8 V,[63] our results are in the middle range, without being especially low or high. The difference between $V_{\text{oc}}^{\text{SQ}}$ and E_{bg}/q is maintained constant around 0.3 V. This is the value one may expect from the Shockley-Queisser limit,[49] especially considering that with the same illumination conditions, the only parameter that can affect this difference is the E_{bg} , which is similar for all devices.

In general, the largest voltage loss is $\Delta V_{\text{oc}}^{\text{nr}}$ (yellow boxes in [Figure 5.15](#)), which varies from 0.17 V for PTQ10:O-IDFBR in CF, up to 0.38 V for D18:PMI-FF-PMI in CB. The $\Delta V_{\text{oc}}^{\text{nr}}$ is especially interesting since, a priori, it is the parameter that can be more affected by the engineering of materials and processing conditions. This is the case, for example, of the PTQ10:O-IDFBR blend. When the blend is processed from CB, the cell has a higher V_{oc} showing lower $\Delta V_{\text{oc}}^{\text{total}}$. Nevertheless, the blend processed from CF shows the lowest $\Delta V_{\text{oc}}^{\text{nr}}$ of 0.17 V at expenses of the highest $\Delta V_{\text{oc}}^{\text{r}}$ of 0.15 V, which are significantly different from the values measured with the same blend processed from CB (0.24 and 0.04 V, respectively). This is directly related to the measured EL spectrum shown in the central panel of [Figure 5.14](#) where it can be seen that the highest EL peak of the PTQ10:O-IDFBR blend processed from CB is centered at 1.95 eV while for the blend deposited from CF is approximately at 1.55 eV. The latter results in a difference of two orders of magnitude in the EQE_{PV} tail, yielding a J_0^{rad} ten times larger for the CF-processed device. Following [Equation 5.8](#), the difference

Active layer materials			$J_{sc}^{calculated}$ (mA/cm ²)	V_{oc}^r calculations		
Donor	Acceptor	Solvent		J_{sc} (mA/cm ²)	J_0 (mA/cm ²)	V_{oc}^r (V)
D18	PMI-FF-PMI	CB	4.95	4.94	$7.60 \cdot 10^{-28}$	1.66
D18	PMI-FF-PMI	CF	5.05	5.59	$8.92 \cdot 10^{-28}$	1.65
D18	O-IDFBR	CB	3.85	3.34	$1.25 \cdot 10^{-27}$	1.63
D18	O-IDFBR	CF	4.48	3.76	$6.46 \cdot 10^{-27}$	1.59
D18	IO-4Cl	CF	8.32	7.65	$3.95 \cdot 10^{-25}$	1.51
PTQ10	PMI-FF-PMI	CF	3.44	3.12	$2.14 \cdot 10^{-27}$	1.62
PTQ10	O-IDFBR	CB	9.06	8.31	$1.37 \cdot 10^{-26}$	1.59
PTQ10	O-IDFBR	CF	7.97	7.27	$2.68 \cdot 10^{-25}$	1.51
PTQ10	IO-4Cl	CB	7.47	7.62	$2.01 \cdot 10^{-24}$	1.46
PTQ10	IO-4Cl	CF	10.53	10.16	$8.80 \cdot 10^{-25}$	1.49
PM6	PMI-FF-PMI	CF	2.16	1.94	$3.63 \cdot 10^{-26}$	1.53
PM6	O-IDFBR	CB	5.00	4.43	$1.35 \cdot 10^{-25}$	1.52
PM6	O-IDFBR	CF	5.93	2.38	$7.37 \cdot 10^{-26}$	1.52
PM6	IO-4Cl	CF	9.83	7.05	$1.32 \cdot 10^{-24}$	1.47

Table 5.6: Results of V_{oc}^r calculation. The good agreement between the measured J_{sc} and the calculated $J_{sc}^{calculated}$ denotes that the measured EQE_{PV} is correct.

Active layer materials			V_{oc} values (V)				V_{oc} losses (V)			
Donor	Acceptor	Solvent	V_{oc}	V_{oc}^r	V_{oc}^{SQ}	$q E_{bg}$	ΔV_{oc}^{nr}	ΔV_{oc}^r	ΔV_{oc}^{sc}	ΔV_{oc}^{total}
D18	PMI-FF-PMI	CB	1.28	1.66	1.71	2.01	0.38	0.03	0.02	0.73
D18	PMI-FF-PMI	CF	1.36	1.65	1.71	2.01	0.29	0.02	0.03	0.65
D18	O-IDFBR	CB	1.33	1.63	1.72	2.02	0.30	0.04	0.05	0.69
D18	O-IDFBR	CF	1.31	1.59	1.74	2.04	0.28	0.03	0.11	0.73
D18	IO-4Cl	CF	1.24	1.51	1.57	1.86	0.27	0.02	0.04	0.62
PTQ10	PMI-FF-PMI	CF	1.38	1.62	1.68	1.98	0.24	0.04	0.02	0.60
PTQ10	O-IDFBR	CB	1.35	1.59	1.65	1.95	0.24	0.02	0.04	0.60
PTQ10	O-IDFBR	CF	1.34	1.51	1.68	1.98	0.17	0.02	0.15	0.64
PTQ10	IO-4Cl	CB	1.19	1.46	1.54	1.83	0.27	0.02	0.05	0.64
PTQ10	IO-4Cl	CF	1.25	1.49	1.55	1.84	0.24	0.02	0.04	0.59
PM6	PMI-FF-PMI	CF	1.25	1.53	1.60	1.89	0.28	0.06	0.01	0.64
PM6	O-IDFBR	CB	1.19	1.52	1.60	1.89	0.33	0.04	0.04	0.70
PM6	O-IDFBR	CF	1.22	1.52	1.60	1.89	0.30	0.05	0.03	0.67
PM6	IO-4Cl	CF	1.16	1.47	1.55	1.84	0.31	0.02	0.05	0.68

Table 5.7: Tabulated values of V_{oc} losses analysis. The V_{oc} values are the different V_{oc} calculated following the procedure described in this section. The difference between them (ΔV_{oc}) correspond to the different voltage losses associated to non-radiative (ΔV_{oc}^{nr}), radiative (ΔV_{oc}^r), and due to J_{sc} difference (ΔV_{oc}^{sc}). The total voltage loss is also shown (ΔV_{oc}^{total}).

between both blends is approximately $k_B T / q \ln(10) = 0.06$ V which is roughly the difference between the V_{oc}^r of the CF and the CB-processed solar cells (1.51 and 1.59 V respectively). We attribute this considerable difference in EL spectrum to the different microstructure, as suggested by GIWAXS data discussed in [Section 5.2.1.4](#). The increased intensity of the lower energy EL peak of the CF-processed cell indicates a higher recombination of injected electron-hole pairs through the charge-transfer state. On the other hand, the CB-processed cell shows a stronger emission of the singlet state of the donor and/or the acceptor materials (it is difficult to discern due to the overlap of both materials EL emission). The latter, together with GIWAXS data, suggests that the CF-processed blend has more donor-acceptor interfaces due to a more intermixed blend, while the CB-processed blend has larger domains of pure donor and acceptor.

[Figure 5.16](#) shows the ΔV_{oc}^{nr} as a function of the V_{oc}^r . We observe that, even for a systematic study like the case of this work, there is a big dispersion of values. The latter is also seen in the literature values ([Figure 5.16](#), brown points), indicating the difficulty of predicting ΔV_{oc}^{nr} .[\[63\]](#) This study adds data points to the existing literature, especially in the high V_{oc}^r region. The ΔV_{oc}^{nr} lay between 0.25 and 0.35 V, similar to the literature values trend.

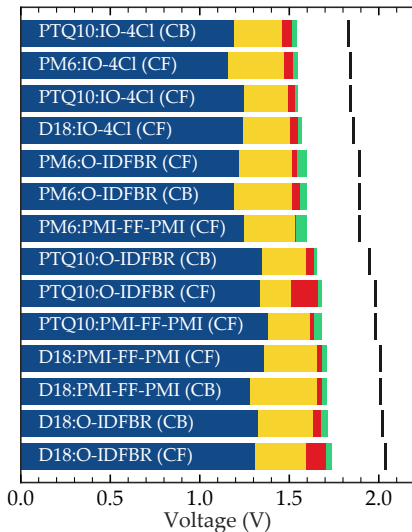


Figure 5.15: ΔV_{oc} loss analysis. Open-circuit voltage losses due to a nonideal short-circuit current density (ΔV_{oc}^{sc} , green), due to radiative recombination (ΔV_{oc}^r , red), and due to non-radiative recombination (ΔV_{oc}^{nr} , yellow) for the different solar cells studied. The cells are ordered in ascending order (from top to bottom) in E_{bg} / q , which corresponds to the black line.

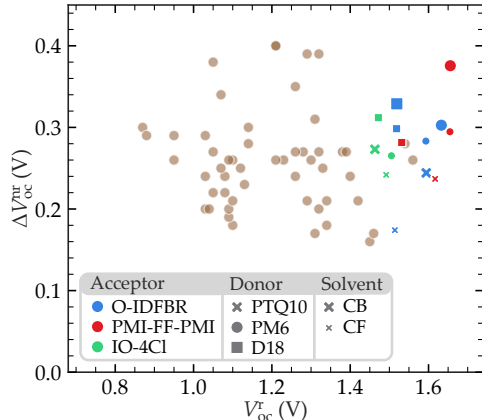


Figure 5.16: ΔV_{oc}^{nr} as a function of V_{oc}^r compared with literature from reference [63].

5.2.4 FCC-Cl as a promising wide band-gap NFA

We have recently explored an interesting acceptor material, motivated by the various applications of wide band-gap photovoltaics such as indoor light harvesting or RAINBOW solar cells. In the work by Bai et al., they design and synthesize a non-fullerene acceptor (NFA) named FCC-Cl.[FBai2021] The HOMO and LUMO levels that they report are similar to the O-IDFBR energy levels. Nevertheless, they show a red shift of about 50 nm in the absorption spectrum of the FCC-Cl in film compared to solution. The latter is attributed to the high crystallinity of the NFA, a feature not present in O-IDFBR. Therefore, optical properties show that FCC-Cl blends are a good candidate for wide band-gap applications. They report blends of FCC-Cl with D18 and PM6 donors. As mentioned before, these donors are interesting candidates for wide band-gap photovoltaics. The D18:FCC-Cl devices were fabricated with the normal geometry with ITO/PEDOT:PSS/AL/PDI-NO/Al while PM6:FCC-Cl were fabricated with the normal geometry (and the same ETL and HTL materials used in our labs). In both cases, the cells were prepared by spin-coating. Under 1 Sun illumination the D16:FCC-Cl blend achieves a *PCE* of 31.1% with a V_{oc} of 1.08 V, a J_{sc} of 16.04 mA cm^{-2} and a *FF* of 76.0%. [FBai2021] The PM6:FCC-Cl blend achieved similar values with a *PCE* of 13.0% with a V_{oc} of 1.02 V, a J_{sc} of 16.22 mA cm^{-2} and a *FF* of 78.1%. [FBai2021]

These results motivated us to do a first trial with the FCC-Cl. We choose to use PTQ10 as the donor since we have seen that it showed higher V_{oc} due to its deeper HOMO level compared to D18 and PM6. Only two substrates with the PTQ10:FCC-Cl were prepared from a solution of 1:1.5 PTQ10:FCC-Cl in chlorobenzene. The results of the

$J - V$ characterization at 1-Sun of one of the best-performing substrate are presented in Figure 5.17. The other substrate showed similar results. The best cell exhibited a PCE of 10.98% with a V_{oc} of 1.07 V, a J_{sc} of 14.49 mA cm⁻² and a FF of 70.63%. The thickness dependence of the different parameters is the expected, with FF its maximum at a thinner active layer than the maximum of J_{sc} . Nevertheless, in this case, the effect of FF on device performance is more important than the effect of J_{sc} since FF decreases almost half its peak value (from ~70% to ~40%). The decrease in FF is due to an increase of series resistance, R_s , as expected from thicker devices at 1 Sun illumination.

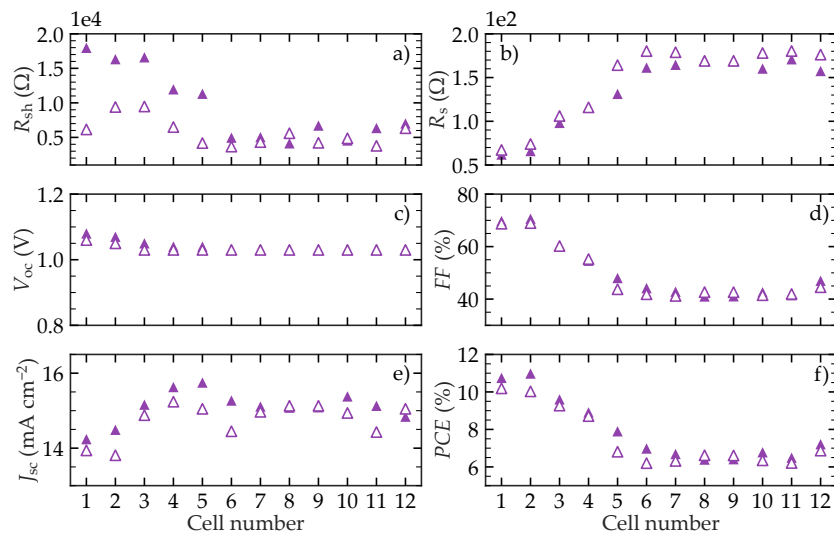


Figure 5.17: Thickness dependence FoM of PTQ10:FCC-Cl sample. Thickness increases with cell number. The different FoM are plotted against cell number. There is a good concordance between the right and the left side of the substrate (filled and empty triangle data points, respectively).

5.3 APPLICATION EXAMPLES OF WIDE BAND-GAP OPV

5.3.1 Indoor light harvesting

For indoor applications, wide band-gap active layer materials are especially interesting due to their E_{bg} matching indoor spectrum, which is especially true for the actual LEDs used in most modern indoor lighting. For the real application of OPV in indoor lighting, it is also worth mentioning the role of having a high V_{oc} , even if maintaining the efficiency results in lower J_{sc} . Imagine the case of two solar cells with the same efficiency and FF but different V_{oc} and J_{sc} values under

AM1.5G illumination. Now, these cells are exposed to indoor light, which proportionally decreases J_{sc} by the same value (for example, three orders of magnitude). In this situation, the drop in efficiency due to the decrease in J_{sc} will be proportionally the same in both cells. Nevertheless, due to V_{oc} being proportional to the logarithm of J_{sc} , the 3 orders of magnitude drop in J_{sc} due to the reduced input light represents the same V_{oc} drop in absolute value regardless of the V_{oc} of the cell at AM1.5G. Therefore, a solar cell with a higher V_{oc} would benefit from a lower drop in efficiency percentage-wise, thus having a lower drop on the $V_{oc}J_{sc}$ product.

Due to its high E_{bg} , V_{oc} , and PCE , the PTQ10:O-IDFBR cells deposited from CB are good candidates for indoor light harvesting. This sample was measured under LED indoor light conditions, using a Wavelabs SINUS-70 LED solar simulator to generate a 560 Lux LED source with a correlated color temperature (CCT) of 12.200 K. The spectrum is shown in Figure 5.18 (a), and its color is plotted in the CIE 1960 uniform chromaticity space in Figure 5.18 (b). In the latter, we can see that the human eye sees the color of the tested spectrum as blueish, which is far from the D standard illuminants used as standards for commercial indoor lighting. Nevertheless, the closer point of the Planckian locus, which characterizes the CCT of the spectrum (Δ_{uv}), is lower than 0.05, $|\Delta_{uv}| < 0.05$. According to the CIE standards, the latter indicates that the calculated CCT is meaningful.

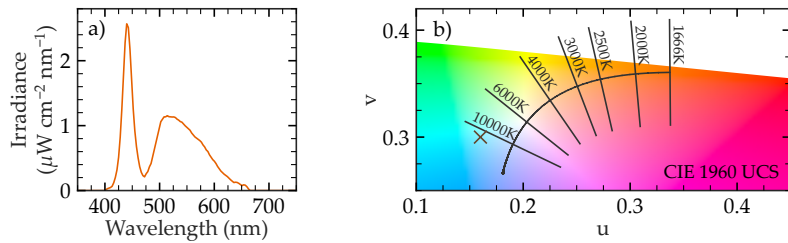


Figure 5.18: Characteristics of LED light source for indoor measurements Figure 5.19. (a) Irradiance spectrum of the LED light source used. (b) The corresponding color of the indoor spectrum in the in the CIE 1960 uniform chromaticity space (brown cross) at coordinates ($u=0.16$, $v=0.30$). The correlated colour temperature of the spectrum is 12,200 K and the intensity is 560 Lux.

Figure 5.19 (a) shows the thickness dependence of the measured efficiency under indoor lighting. The best-performing device corresponds to 4th pixel for both sides of the samples, achieving 22.6% on the right side (see the $J - V$ curve shown in Figure 5.19 (b)). The latter slightly differs from the measurement of the same sample under 1-sun illumination, which in that case corresponds to the 6th pixel. Thus, the

optimum thickness for indoor is thicker than for AM1.5G illumination. This is due to different factors limiting efficiency at different light-intensity conditions.[23] For light intensities similar to the solar light, the main limiting factor is the series resistance, R_s .[23] The latter is proportional to J_{sc} , therefore, a thicker active layer, generally exhibiting higher J_{sc} due to an increased light absorption, will exhibit higher R_s . The latter results in the maximum FF happening at a thinner active layer than the maximum J_{sc} . Thus, the optimal thickness is generally in-between. On the contrary, When the light intensity is a few orders of magnitude lower, i.e. similar to indoor conditions, R_s becomes negligible and the shunt resistance R_{sh} is the limiting factor. The latter depends on the leakage current of the device, which is mainly produced by active layer defects such as pinholes. The latter is reduced in thick films compared to thin. Therefore, the optimum FF generally moves to thicker active layers at low illumination. When the light power is reduced even more, the $J - V$ curve becomes a line without rectifying. The latter happens when R_{sh} is approaching the dark shunt resistance ($R_{sh,d}$). Therefore, a cell with a higher $R_{sh,d}$ can still work at lower light intensities.

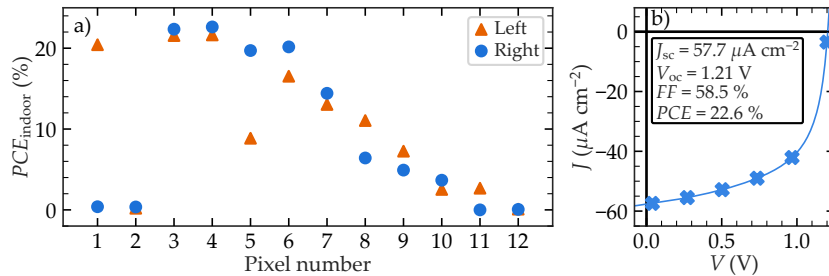


Figure 5.19: Indoor characterization of PTQ10:O-IDFBR deposited from CB sample. (a) efficiency dependence on pixel (i.e., thickness) of the measured sample. (b) $J - V$ curve of the best performing device corresponding to the pixel number 4 of the right side.

In order to study the FF dependence on light intensity for the PTQ10:O-IDFBR system we have measured $J - V$ curves of two PTQ10:O-IDFBR devices at different light intensities in a wide dynamic range. The latter was done with the spectrum on demand light source (SOLS) explained in Chapter 3. The data points are the result of a red sweep measurement, as shown in Figure 3.11 (c). It means that different light intensities were achieved by blocking the blue part of the solar spectrum maintaining the red fraction constant. This implies that the spectrum at each data point does not have the same shape. Nevertheless, assuming that the generated charges thermalize before they are extracted, the shape variance of the spectrum is not an issue. As a first approximation, J_{sc} is the parameter analogous to the light intensity when the latter is

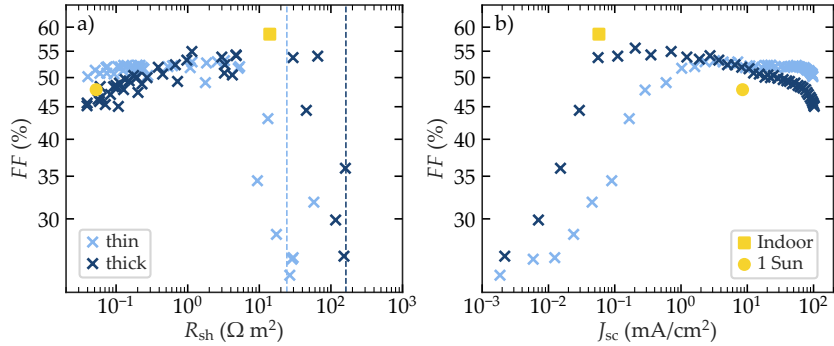


Figure 5.20: Evaluation PTQ10:O-IDFBR leakage with light-intensity dependent measurements. (a) Fill factor (FF) plotted against shunt resistance (R_{sh}) for a thin (light blue crosses) and a thick (dark blue crosses) measured at different light intensities during a red sweep using the custom Spectrum On Demand Light Source (SOLS). Dashed vertical lines correspond to the R_{sh} of both cells measured in dark $R_{sh,d}$. (b) FF vs. J_{sc} for the same data set. yellow square in (a) and (b) corresponds to the data point of the solar cell measured under indoor conditions shown in ???. The yellow circle in (a) and (b) corresponds to the same cell measured under 1 Sun.

maintained with a constant spectral shape. Figure 5.20 (a) shows the FF vs. R_{sh} for the red sweep of two PTQ10:O-IDFBR cells with different thicknesses (blue data crosses). The vertical lines show the $R_{sh,d}$ for both devices. As expected, the thicker device (dark blue) has a higher $R_{sh,d}$ due to lower leakage current. The latter results in a FF higher than the thin device (light blue) at lower intensities. On the opposite, at high intensities, the thin cell exhibits a higher FF due to its lower series resistance produced by a thinner active layer. The yellow squared and rounded data points correspond to the solar cell under indoor conditions for indoor illumination and 1-sun illumination, respectively. This cell at 1-sun has a FF in between the other two cells. Therefore, under indoor conditions, we expect this cell to behave between the blue data points, with a $R_{sh,d}$ in the middle. The corresponding square yellow data point is inside the expected trend, exhibiting a high FF at R_{sh} just below the $R_{sh,d}$ of the thinner device.

Similarly, Figure 5.20 (b) shows the FF vs. J_{sc} for the same red-sweep measurements. The tendency is expected since the thicker device (dark blue) exhibits a higher FF at low J_{sc} (i.e., low luminosity) while the thinner (light blue) shows higher FF at the J_{sc} region near 1-sun illumination. The yellow data points, corresponding to the cell characterized under indoor conditions for indoor illumination (yellow square) and 1-sun illumination (yellow circle), are also in between the behavior of the other two cells.

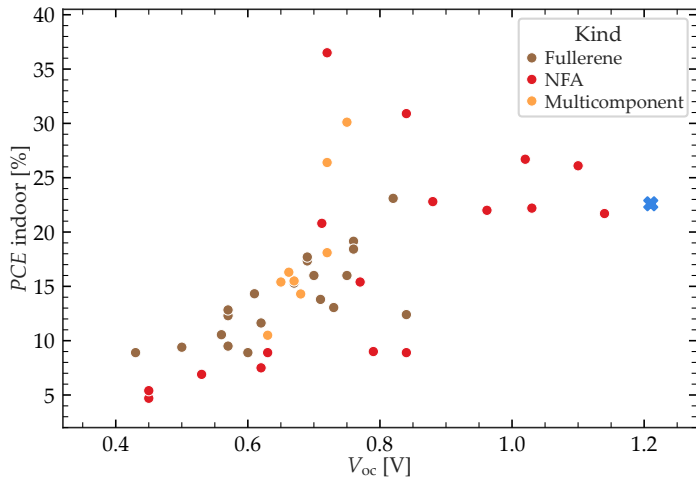


Figure 5.21: Comparison with the state-of-the-art indoor organic solar cell efficiency. The state-of-the-art data points are extracted from references [51, 53, 50, 54]. The record PTQ10:O-IDFBR cell has a V_{oc} of 1.21 V which is the highest reported for indoor cells, to the best of our knowledge.

Figure 5.21 shows a comparison of the state-of-the-art indoor organic photovoltaic devices in the literature according to references with LED-type light sources. To the best of our knowledge, the cell measured in this work made of PTQ10:O-IDFBR deposited from CB exhibits the highest V_{oc} achieved for indoor organic photovoltaics ($V_{oc} = 1.21$ V), and its indoor efficiency is among the best reported in the literature ($PCE = 22.6\%$).

5.3.2 RAINBOW solar cells

As discussed previously, another application of wide E_{bg} solar cells is in multi-junction devices. The development and improvement of solar cells with E_{bg} higher than 1.8 eV directly impacts the efficiency of multi-junction PV. This is the case of the RAINBOW geometry studied in this thesis. In this chapter, we used the simulation model explained in Chapter 4 to study the potential of the materials tested in the combinatorial screening as blue sub-cells in RAINBOW configuration of two and three junctions. The other mate

This sub-section is still under construction. New things will be added after the RAINBOW chapter is finished. But the idea is what the latter paragraph says: put into context the WBG materials in the RAINBOW configuration with simulations with Alfonsina's and Xavi's cells.

Additionally, if I have time I would like to add some more examples (which i guess it will be mainly simulations) taking advantage of the

SOLS vustom hability of producing spectra. But I have to think more about what can go in an additional subsection.

5.4 UPSCALING OF PTQ10:O-IDFBR OPV

During the last stages of my PhD thesis, I had the opportunity to visit EURECAT's labs in Mataró. EURECAT is one of the most important technological centers in Catalunya. There I joined Dr. Igasi Burgues Ceballos and Ms. Paula Pinyol. They are working on up-scaling organic photovoltaics. The latter is done by transitioning from lab-scale cells to industrial production of modules. My stay at EURECAT mainly aimed to investigate the up-scaling of PTQ10:O-IDFBR blend as the active layer for organic PV modules. The latter can be interesting for the industrial application of OPV as indoor light harvesters. For this reason, part of the challenge was to use techniques compatible with industrialization (i.e., preferably roll-to-roll (R2R) compatible). We did not change the methodology for preparing the electron transport layer (ETL) and the active layer, which were prepared by blade coating. Nevertheless, active layer (AL) deposition was done outside the glovebox, aiming for a more industry-compatible solution for the already R2R-compatible technique. On the other hand, the hole transport layer (HTL) and the top electrode were deposited by physical vapor deposition, as we do in our labs. The compatibility with solution-processable HTL and top electrodes for the PTQ10:O-IDFBR blend was not studied to avoid more unknown variables and sources of errors. Nevertheless, it is important to highlight that the physical vapor deposition technique is undesirable for industrialization, and using R2R-compatible inks like PEDOT:PSS or Ag nanowires is a better choice. The latter is a topic under study at EURECAT, and at this point, they are trying to find suitable candidates for other systems.

5.4.1 Depositing the active layer at ambient air

A typical difference when moving from lab-scale processing to R2R schemes is the processing atmosphere. At the lab scale, the use of inert atmospheres achieved by working inside a glovebox is common, at least for steps like the deposition and thermal annealing of the active layer. Conversely, up-scale production aims to operate in the air, thus reducing the process cost.[88, 89, 90, 91, 92] This may induce some degree of degradation in the corresponding layers, mainly those composed of organic molecules, like the active layer. The latter can affect their electrical properties. Therefore, when depositing the active layer outside the glovebox, one may expect a decrease in the efficiency

of the solar cell. The latter can be more or less critical depending on different factors like the materials composing the active layer, the deposition temperature, or the time exposed to air.

In this case, we want to see the effect of depositing the active layer outside the glovebox, i.e., in a different atmosphere. With this scope, we have fabricated two samples with the standard NANOPTO procedure described in [Chapter 2](#), and two samples with identical conditions except that the AL was deposited outside the glovebox. Since the solvent used in both cases was chlorobenzene (CB), the deposition temperature was 80°C. The efficiency of all devices under 1-Sun light was measured to assess the effect of the atmosphere on device performance. Ideally, we would compare the *PCE* of pixels between the different substrates. Nevertheless, reproducing the thickness profile is challenging, and every substrate may have a slightly different thickness profile. For this reason, we selected the eight highest-performing pixels of the two samples deposited inside and the two samples deposited outside as the datasets to compare.

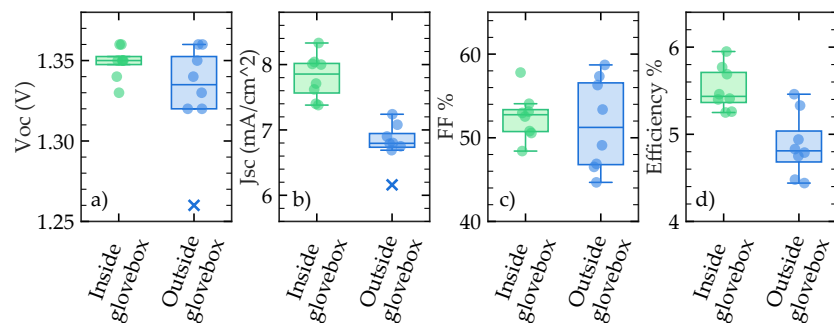


Figure 5.22: Comparison between solar cells of PTQ10:O-IDFBR prepared inside and outside the glovebox. Two samples for each atmospheric condition (inside the glovebox (green) and outside the glovebox (blue)) were prepared and the 8 best-performing cells were selected as datasets. Their different FoM are plotted as boxplots with data points shown as dots for points inside the boxplot limits and crosses for outliers.

[Figure 5.22](#) shows the boxplot of the FoM of those datasets to compare the effect of the atmospheric conditions during blade coating of the active layer. First, we must notice that the *PCE* mean of the samples prepared inside the glovebox is below the previous efficiency with the same system. Explaining the latter is not in the scope of this experiment. Nevertheless, one possible explanation could be that the batch of PTQ10 used was different from that of the previous cells. As shown by Riera-Galindo et al., PTQ10-based cells have a strong dependence on molecular weight.[\[SRieraGalindo2024\]](#) On average, samples prepared outside the glovebox have lower *PCE* than those prepared inside, as

expected by a possible degradation due to oxygen and moisture present only outside the glovebox. The decrease in the mean performance is 0.65% in absolute value. To find statistical evidence that the sample sets are different, we performed the t-test analysis.[Student1908] Our alternative hypothesis is that devices prepared outside the glovebox have lower efficiency than devices prepared inside. Therefore, we consider a one-tail t-test with a typical confidence interval of 0.05%. In our case, the threshold value for $t_{0.95}$ is 1.782, and the calculated t value is 4.131. Thus, the samples prepared outside the glovebox statistically have lower performance than those prepared inside. Therefore, we confirm the expected detrimental effect of depositing the active layer in the air. Nevertheless, this effect does not dramatically decrease device performance and only affects the efficiency by 11%. The comparison of the FoM between the two data sets (Figure 5.22) shows that the difference in PCE between devices fabricated in different atmospheres is mainly due to J_{sc} . The latter is the parameter that has a higher decrease due to blade coating outside the glovebox. V_{oc} and FF means are similar regardless of the atmospheric conditions but they exhibit higher standard deviation outside the glovebox. The latter might be an indication of poorer stability. Nevertheless, no more experiments were carried out in that direction.

5.4.2 Effect of cell width on modules performance

In lab-scale, we typically study solar cells, i.e., a single photovoltaic device. Nevertheless, single solar cells are not suitable for the commercial application of PV, and the connection of multiple solar cells is needed. The devices resulting from connecting multiple solar cells are known as modules. Within OPV modules, solar cells are typically connected in series. It is important to make this difference because different challenges appear when fabricating modules besides the efficiency of each single cell itself, with the interconnection between cells being one of the most critical aspects. This is mainly due to the fact that solution-processing methodologies (R2R) produce thin films that need to be patterned in order to construct a geometry with multiple cells placed along the thin-film plane. There are different ways to achieve this lateral patterning. For example, slot die coating can produce stripes of material, thus defining the different cells. Nevertheless, the need for patterning multiple layers (ETL, HTL, and electrical contacts) introduces the challenge of aligning the patterns. Additionally, border effects can introduce thickness gradients along each strip, reducing homogeneity between cells. A more promising approach is using laser patterning to define the individual cells in an initially fully coated substrate. Investigators from EURECAT are developing this method in their labs. In this case, one of the most critical aspects is the interconnections

between cells. One must have a reliable interconnection with low series resistance and avoid short-circuiting the cell, for which patterning must be very specific to certain layers.

5.4.2.1 Laser patterning of modules



Figure 5.23: Schematics of laser patterning used to fabricate PTQ10:O-IDFBR modules. (a) Cross-section view of the laser patterning. P1, P2, and P3 refer to the different laser patterning steps to define the four cells connected in series. Each cell has a width (W_{cell}) composed by an active area (highlighted with a dashed line) and the interconnection with the next cell with a width of W_i . (b) Top-view of the laser patterning. P1 final is done after P3 and defines a cell height of $h_{cell}=2$ cm.

Figure 5.23 shows a scheme of the laser patterning used for the fabrication of modules. The process comprises four laser patterning steps named P1, P2, P3, and P1 final. The first patterning step (P1) aims to define the bottom electrode of the cells, defining its width (W_{cell}). In our case, we are using ITO-covered glass substrates. Therefore, P1 has to blaze the ITO film. The latter is achieved because the laser emits at a wavelength of 1064 nm, the ITO absorbs that radiation and heats up quickly, and gets ablated in that region. After P1, substrates are cleaned with the standard procedure described in Chapter 2. Then, ETL (ZnO) and the active layer are prepared as described in Chapter 2, with the only difference being that the active layer is deposited outside the glovebox. After the active layer deposition, samples are entered inside the glovebox, and a 10 nm thin film of MoO₃ is physically evaporated. Afterward, the second laser patterning step (P2) is performed. The investigators at EURECAT found in previous studies that performing P2 (which is done in air atmosphere) after deposition of MoO₃ gave better results than performing it before the deposition of the HTL. They attribute it to the fact that the thin HTL can protect from oxygen and moisture degradation of the active layer interface with the HTL. In this P2 step, we want to create a vertical trench so that the top electrode deposited afterward creates the electrical interconnection between the top electrode of one cell and the next cell's bottom (ITO) electrode. Therefore, we need to set conditions for the laser patterning that ablaze the ETL/AL/HTL stack with the minimum possible impact on ITO conductivity. Subsequently, substrates are entered again inside the glovebox to evaporate 100 nm of silver as the top electrode. Due to

the formed trenches, the evaporation will create the interconnections between cells. Nevertheless, a final patterning step (P3) needs to be done in order to isolate the top electrodes of the different cells. The latter has to be done by adapting the laser conditions to affect only the silver top electrode and minimizing the ablation of all other layers. The vertical trench created by the P2 and the silver evaporation must also remain intact. Last but not least, a final patterning step is done in the direction perpendicular to P1, P2, and P3. This final patterning aims to define a known module height ($h_{\text{cell}}=2 \text{ cm}$) and isolate the central part of the substrate (where the module is built) from its edges (where some unwanted edge effects could introduce extra shunt resistance to the device due to unwanted contacts between non-adjacent layers). For this reason, this last step (P1 final) has to be done with laser parameters that are more extreme than P1 to ensure that the trench created by the laser ablates all layers.

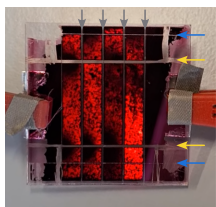


Figure 5.24: Electroluminescence of a module where P1 final laser patterning is not done correctly. The gray arrows are the P1, P2, and P3 lines and the blue arrows are the P1 final. The yellow arrows correspond to scratching the module with a toothpick.

As a curiosity, in the first modules fabricated, the P1 final laser patterning was not done correctly because the laser conditions were too soft. The resulting modules had no rectifying behavior and did not work as PV modules. I discovered that the problem was the P1 final because, during a $J - V$ measurement of a module, I observed electroluminescence inside and outside the module area defined by the laser patterning.

5.4.3 Studying cell width dependence

One of the most important parameters to optimize in the fabrication of modules is the cell width (w_{cell}). From the perspective of a single cell, cells with larger areas tend to suffer from low FF due to parasitic losses and a higher effect of the series resistance. The first is due to more pinholes and active layer defects in larger areas while the second is related to a higher photocurrent (not photocurrent density) due to increased area. Notice that, as discussed before, for indoor applications the parasitic resistance has a more important role because of the low light intensity. Therefore, different active layer and selective transport layer materials would have different properties that may result in a different optimal w_{cell} . Nevertheless, there is an opposite trend when cells are incorporated into modules. Consider the total area of each cell in a device as the active area of the cell plus the interconnection area (like that depicted in Figure 5.23 (a)). The interconnection area is a constant that depends on the laser patterning but not on the cell width. The resolution of the laser and the separation between P1 and P3 (w_i in Figure 5.23 (a)) define this area. The ratio between the module's active area (the sum of individual cells active areas) and the module's total area is known as the geometrical fill factor (GFF). The GFF represents

which percentage of the total area of the module is active area, therefore high *GFF* values are desired. Considering a constant interconnection area, the wider the cell width, the higher the *GFF*. Nevertheless, *GFF* can never be equal to 100% because interconnections are always needed in a module. Thus, *GFF* dependence on cell width is the opposite of the *FF*. In this case, *GFF* is mainly dependent on the equipment used for laser patterning but can also be influenced by the materials composing the device since different materials may behave differently to laser patterning and produce, for example, wider or narrower P2 trenches. Figure 5.25 shows the *GFF* dependence on cell width for our devices. The interconnection distance (w_i in Figure 5.23) was obtained by measuring the distance between P1 and P3 with an optical microscope of a few samples and taking the average. Figure 5.26 shows two examples of this measurement. The average w_i obtained is 180 μm .

We fabricated modules of four cells with cell widths varying from 2 to 3.6 mm in 0.4 mm steps. The height of the cells defined by the P1 final patterning was maintained constant with a value of 2 cm. The modules were fabricated for three different active layer thicknesses achieved by depositing at 40, 60 and 80 mm s^{-1} . Figure 5.27 shows the FoM of all modules measured under 1-Sun conditions. We can see a strong V_{oc} dependence on cell width (Figure 5.27 (a)). Considering that all modules were made of four cells, one may expect a V_{oc} similar for all modules. The value should approach the V_{oc} of a single cell ($V_{\text{oc}}^{\text{cell}}$) multiplied by four because cells are connected in series. Nevertheless, the module achieving the highest V_{oc} shows a $V_{\text{oc}}^{\text{cell}} = V_{\text{oc}}/4$ of 5.16 V/4=1.29 V. The latter is close to the $V_{\text{oc}}^{\text{cell}} = 1.33$ V expected from the devices fabricated outside the glovebox shown in Figure 5.22 (a). Nevertheless, the V_{oc} still shows room for improvement since some of the cells showed $V_{\text{oc}}^{\text{cell}} \geq 1.35$ V. On the opposite, the modules with $V_{\text{oc}} \leq 2$ V exhibit a $V_{\text{oc}}^{\text{cell}} \leq 0.5$ V which is clearly below the expected value. The decrease in V_{oc} as cell width increases, observed from 2.8 to 3.6 mm cell width, can be explained as an increase in the series resistance of the electrodes in a single cell. The latter also affects the *FF*, which also decreases with cell width. Nevertheless, we did not find any explanation for the opposite trend of V_{oc} for lower cell widths, and further studying this behavior may be needed to understand its nature. On the other hand, a decrease in *FF* as cell width decreases can be explained by the reduction of the geometrical fill factor (*GFF*) as the fraction of area used as interconnection increases when decreasing cell width.

J_{sc} shown in Figure 5.27 (c) is calculated considering only the active area of the device (i.e., without considering the interconnection between cells). In this case, since cells are connected in series, the J_{sc} value of the single cell device ($J_{\text{sc}}^{\text{cell}}$) has to be compared with the J_{sc} of the

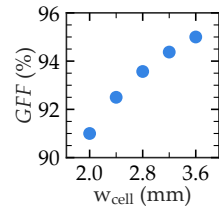


Figure 5.25: *GFF* vs. w_{cell} for the modules fabricated. The measured w_i of 180 μm was considered for the calculation of *GFF*.

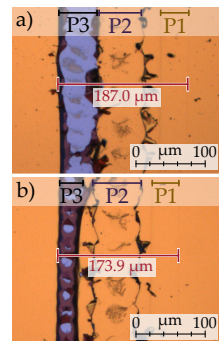


Figure 5.26: Optical microscopy images of the interconnection between cells. P1, P2 and P3 laser patterning lines are marked in the top part as a reference.

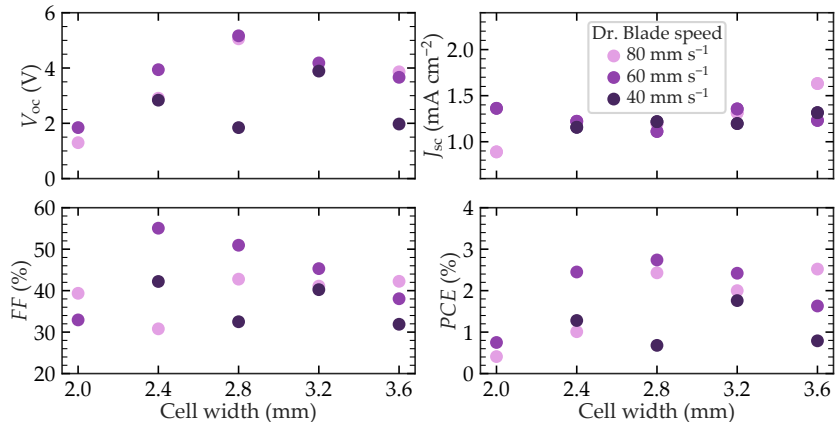


Figure 5.27: Cell width study of PTQ10:O-IDFBR modules. FoM of PTQ10:O-IDFBR modules fabricated with different w_{cell} measured under 1-Sun illumination.

module multiplied by four. The values of Figure 5.27 (c) lay between 1.1 and 1.4 mA cm⁻² which corresponds to a J_{sc}^{cell} in between 4.4 and 5.6 mA cm⁻². The latter is lower than expected considering that the J_{sc}^{cell} of the reference devices fabricated outside is 6.8 mA cm⁻² (see Figure 5.22). This represents a loss of approximately 25% of the J_{sc} achieved in the reference devices. The latter suggests that the interconnections do not offer a good connection and may decrease the shunt resistance of the device.

It seems clear that for the modules deposited at 60 mm s⁻¹, the optimum cell width is 2.8 mm since in these conditions we have measured the maximum PCE of 2.74% of a module in this study. The latter could be also the case for thinner modules (deposited at 40 mm s⁻¹), because the low efficiency of the module with $w_{cell}=2.8$ mm could be an outlier. Nevertheless, for the thicker modules (deposited at 80 mm s⁻¹), the tendency seems to be that higher cell widths could give better performance. Therefore, the optimum cell width for this active layer system may lay around 2.8 mm although higher cell widths may also achieve good performance for thick active layers.

The best modules were also tested under indoor illumination with a professional photograph LED setup at 6500K with an intensity of 500 and 1000 Lux. We do not show any results because the modules showed almost no rectifying behavior, with efficiency values below 0.2%. We attribute the latter to the low shunt resistance (R_{sh}) of the modules compared with the devices prepared in the first instance. One possible origin of the decrease in R_{sh} may be the module fabrication itself. The latter could be improved by further optimizing the laser patterning conditions and the fabrication of the modules. Additionally,

one can also think on strategies to improve the R_{sh} of each cell. For example, by introducing a vertical stratification in the active layer one should be able to avoid the percolation of charges to unwanted contacts as well as direct percolation paths from one contact to the other. One way to achieve this vertical stratification is by depositing an active layer with a bilayer morphology. The latter is achieved by sequentially depositing solutions of pure donor and acceptor materials. The need of thin layers for a proper exciton dissociation and charge extraction is generally a problem for cells aiming to harvest 1 Sun spectra due to a low J_{sc} . Nevertheless, for harvesting indoor light this problem may be less important and the theoretically improved R_{sh} may play a crucial role.

5.5 CONCLUSIONS AND OUTLOOK

This chapter is motivated for the need of novel wide band-gap materials to use as blue sub-cell for RAINBOW geometries. We performed a combinatorial study between 3 donors (D18, PTQ10, and PM6), 3 acceptors (O-IDFBR, PMI-FF-PMI, IO-4Cl), and 2 solvents (chloroform and chlorobenzene). Owing to the variation in the blade-coating velocity used during active layer deposition, 12 different thicknesses (with duplicates for each layer) were tested for each combination, thus giving a total of 432 devices. From this combinatorial screening study, we found that IO-4Cl cells have the highest efficiency under AM1.5G illumination, mainly because IO-4Cl is the material with the lowest E_{bg} , which is closer to the optimal Shockley-Queiser limit. PMI-FF-PMI-based devices showed the lowest efficiencies, mainly due to low J_{sc} , attributed not only to the lower absorption due to the higher E_{bg} of the blends, but also to a worse exciton dissociation and/or charge carrier extraction. The O-IDFBR-based devices are in-between both cases, similar to PMI-FF-PMI for the case where D18 was used as the donor and similar to IO-4Cl when PTQ10 was used as the donor.

We also studied the V_{oc} losses for selected blends. The analysis showed a $\Delta V_{oc}^{\text{total}}$ between 0.6 and 0.7 V, with cells containing PTQ10 always exhibiting the lowest $\Delta V_{oc}^{\text{total}}$ compared to their counterparts. The latter, together with PTQ10 being the donor with the deepest HOMO level, leads PTQ10-based devices to exhibit a higher V_{oc} . Based on these results, we suggest PTQ10 as a suitable donor for wide band-gap organic solar cells. Specially interesting was the PTQ10:O-IDFBR blend due to its low $\Delta V_{oc}^{\text{nr}}$, relatively high efficiency (6.87%) and remarkably high V_{oc} (1.35 V). These cells were also tested under indoor light conditions showing an efficiency of 22.6% with a V_{oc} of 1.21 V. This blend efficiency under indoor lightning is among the best in the OPV and the achieved V_{oc} is, as far as we know, the highest reported

value of indoor OPV.

These interesting results were crossed with narrow band-gap materials developed in the group by Dr. Alfonsina Abat Amelenan Torim-tubun which reached an efficiency of XXXX for the blend XXX with a band gap of XXX. The RAINBOW simulations show that the system with XXX as the blue sub-cell and XXX as the red sub-cell is showing the highest blablabla.

Additionally, I carried out a stay at EURECAT Mataró in order to investigate on the up-scaling of PTQ10:O-IDFBR cells for applications in indoor light harvesting. The study on cell width led to a first indication of the optimal cell width being at 2.8 mm. Nevertheless, the modules efficiencies were not as good as single cells. The latter is attributed to the geometry of the modules and the poor performance of the contacts between cells. The latter affects to all parameters measured in the $J - V$ curve. Specially critical is the decrease of the shunt resistance, R_{sh} , which led to useless modules under 6500K indoor light. Thus, more optimization is needed in this area in order to achieve useful modules, specially focusing on increasing the R_{sh} .

BIBLIOGRAPHY

1. Casademont-Viñas, M., Gibert-Roca, M., Campoy-Quiles, M. & Goñi, A. R. Spectrum on demand light source (SOLS) for advanced photovoltaic characterization. *Review of Scientific Instruments* **94**, 103907. ISSN: 0034-6748. <https://pubs.aip.org/rsi/article/94/10/103907/2917787/Spectrum-on-demand-light-source-SOLS-for-advanced> (10 Oct. 2023).
2. Gibert-Roca, M., Casademont-Viñas, M., Goñi, A. R. & Campoy-Quiles, M. *Spectral shaper illumination device* 2023. <https://patents.google.com/patent/WO2023227290A1/en?oq=WO2023227290A1>.
3. Li, D. H., Chau, N. T. & Wan, K. K. Predicting daylight illuminance and solar irradiance on vertical surfaces based on classified standard skies. *Energy* **53**, 252–258. ISSN: 03605442. <https://linkinghub.elsevier.com/retrieve/pii/S0360544213001631> (May 2013).
4. Blumthaler, M., Ambach, W. & Ellinger, R. Increase in solar UV radiation with altitude. *Journal of Photochemistry and Photobiology B: Biology* **39**, 130–134. ISSN: 10111344. <https://linkinghub.elsevier.com/retrieve/pii/S1011134496000188> (2 June 1997).
5. Faine, P., Kurtz, S. R., Riordan, C. & Olson, J. The influence of spectral solar irradiance variations on the performance of selected single-junction and multijunction solar cells. *Solar Cells* **31**, 259–278. ISSN: 03796787. <https://linkinghub.elsevier.com/retrieve/pii/037967879190027M> (3 June 1991).
6. Röhr, J. A., Lipton, J., Kong, J., Maclean, S. A. & Taylor, A. D. Efficiency Limits of Underwater Solar Cells. *Joule* **4**, 840–849. ISSN: 25424351. <https://linkinghub.elsevier.com/retrieve/pii/S2542435120300830> (4 Apr. 2020).
7. Ryu, H. S., Park, S. Y., Lee, T. H., Kim, J. Y. & Woo, H. Y. Recent progress in indoor organic photovoltaics. *Nanoscale* **12**, 5792–5804. ISSN: 2040-3364. <https://xlink.rsc.org/?DOI=D0NR00816H> (10 Mar. 2020).
8. Kumar, G. & Chen, F.-C. A review on recent progress in organic photovoltaic devices for indoor applications. *Journal of Physics D: Applied Physics* **56**, 353001. ISSN: 0022-3727. <https://iopscience.iop.org/article/10.1088/1361-6463/acd2e5> (35 Aug. 2023).

9. Minnaert, B. & Veelaert, P. A Proposal for Typical Artificial Light Sources for the Characterization of Indoor Photovoltaic Applications. *Energies* **7**, 1500–1516. ISSN: 1996-1073. <http://www.mdpi.com/1996-1073/7/3/1500> (3 Mar. 2014).
10. Gibert-Roca, M., Casademont-Viñas, M., Liu, Q., Vandewal, K., Goñi, A. R. & Campoy-Quiles, M. RAINBOW Organic Solar Cells: Implementing Spectral Splitting in Lateral Multi-Junction Architectures. *Advanced Materials*, 2212226. ISSN: 0935-9648. <https://onlinelibrary.wiley.com/doi/10.1002/adma.202212226> (Apr. 2023).
11. Peters, I. M., Gallegos, C. D. R., Lüer, L., Hauch, J. A. & Brabec, C. J. Practical limits of multijunction solar cells. *Progress in Photovoltaics: Research and Applications* **31**, 1006–1015. ISSN: 1062-7995. <https://onlinelibrary.wiley.com/doi/10.1002/pip.3705> (10 Oct. 2023).
12. Lüer, L., Peters, I. M., Corre, V. M. L., Forberich, K., Guldi, D. M. & Brabec, C. J. Bypassing the Single Junction Limit with Advanced Photovoltaic Architectures. *Advanced Materials* **36**, 2308578. ISSN: 0935-9648. <https://onlinelibrary.wiley.com/doi/10.1002/adma.202308578> (14 Apr. 2024).
13. Mojiri, A., Taylor, R., Thomsen, E. & Rosengarten, G. Spectral beam splitting for efficient conversion of solar energy—A review. *Renewable and Sustainable Energy Reviews* **28**, 654–663. ISSN: 13640321. <https://linkinghub.elsevier.com/retrieve/pii/S1364032113005662> (Dec. 2013).
14. Reference Air Mass 1.5 Spectra | Grid Modernization | NREL <https://www.nrel.gov/grid/solar-resource/spectra-am1.5.html>.
15. Solar spectrum calculator <https://www2.pvlighthouse.com.au/calculators/solar\%20spectrum\%20calculator/solar\%20spectrum\%20calculator.aspx>.
16. Ayuga, C. E. T. & Zamorano, J. LICA AstroCalc, a software to analyze the impact of artificial light: Extracting parameters from the spectra of street and indoor lamps. *Journal of Quantitative Spectroscopy and Radiative Transfer* **214**, 33–38. ISSN: 00224073. <https://linkinghub.elsevier.com/retrieve/pii/S0022407317308695> (July 2018).
17. Spectra of Lamps | GUAIX https://guaix.fis.ucm.es/lamps_spectra.
18. Bracher, A., Taylor, M. H., Taylor, B. B., Dinter, T., Röttgers, R. & Steinmetz, F. in. In supplement to: Bracher, A et al. (2015): Using empirical orthogonal functions derived from remote-sensing reflectance for the prediction of phytoplankton pigment concentra-

- tions. *Ocean Science*, 11(1), 139-158, <https://doi.org/10.5194/os-11-139-2015> (PANGAEA, 2015). <https://doi.org/10.5194/os-11-139-2015>.
- 19. Bracher, A., Taylor, M. H., Taylor, B., Dinter, T., Röttgers, R. & Steinmetz, F. Using empirical orthogonal functions derived from remote-sensing reflectance for the prediction of phytoplankton pigment concentrations. *Ocean Science* **11**, 139–158. ISSN: 1812-0792. <https://os.copernicus.org/articles/11/139/2015/> (1 Feb. 2015).
 - 20. Almora, O. *et al.* Device Performance of Emerging Photovoltaic Materials (Version 4). *Advanced Energy Materials* **14**, 2303173. ISSN: 1614-6832. <https://onlinelibrary.wiley.com/doi/10.1002/aenm.202303173> (4 Jan. 2024).
 - 21. Esen, V., Şafak Sağlam & Oral, B. Light sources of solar simulators for photovoltaic devices: A review. *Renewable and Sustainable Energy Reviews* **77**, 1240–1250. ISSN: 13640321. <https://linkinghub.elsevier.com/retrieve/pii/S1364032117303787> (Sept. 2017).
 - 22. Vollbrecht, J., Brus, V. V., Ko, S., Lee, J., Karki, A., Cao, D. X., Cho, K., Bazan, G. C. & Nguyen, T. Quantifying the Nongeminate Recombination Dynamics in Nonfullerene Bulk Heterojunction Organic Solar Cells. *Advanced Energy Materials* **9**, 1901438. ISSN: 1614-6832. <https://onlinelibrary.wiley.com/doi/10.1002/aenm.201901438> (32 Aug. 2019).
 - 23. Lübke, D., Hartnagel, P., Hülsbeck, M. & Kirchartz, T. Understanding the Thickness and Light-Intensity Dependent Performance of Green-Solvent Processed Organic Solar Cells. *ACS Materials Au* **3**, 215–230. ISSN: 2694-2461. <https://pubs.acs.org/doi/10.1021/acsmaterialsau.2c00070> (3 May 2023).
 - 24. Hartnagel, P. & Kirchartz, T. Understanding the Light-Intensity Dependence of the Short-Circuit Current of Organic Solar Cells. *Advanced Theory and Simulations* **3**. ISSN: 2513-0390. <https://onlinelibrary.wiley.com/doi/10.1002/adts.202000116> (10 Oct. 2020).
 - 25. Glowienka, D. & Galagan, Y. Light Intensity Analysis of Photovoltaic Parameters for Perovskite Solar Cells. *Advanced Materials* **34**, 2105920. ISSN: 0935-9648. <https://onlinelibrary.wiley.com/doi/10.1002/adma.202105920> (2 Jan. 2022).
 - 26. Krebs, F. C., Sylvester-Hvid, K. O. & Jørgensen, M. A self-calibrating led-based solar test platform. *Progress in Photovoltaics: Research and Applications* **19**, 97–112. ISSN: 1062-7995. <https://onlinelibrary.wiley.com/doi/10.1002/pip.963> (1 Jan. 2011).

27. Lopez-Fraguas, E., Sanchez-Pena, J. M. & Vergaz, R. A Low-Cost LED-Based Solar Simulator. *IEEE Transactions on Instrumentation and Measurement* **68**, 4913–4923. ISSN: 0018-9456. <https://ieeexplore.ieee.org/document/8660521/> (12 Dec. 2019).
28. Hagen, N. & Tkaczyk, T. S. Compound prism design principles, I. *Applied Optics* **50**, 4998. ISSN: 0003-6935. <https://opg.optica.org/abstract.cfm?URI=ao-50-25-4998> (25 Sept. 2011).
29. Hagen, N. & Tkaczyk, T. S. Compound prism design principles, II: triplet and Janssen prisms. *Applied Optics* **50**, 5012. ISSN: 0003-6935. <https://opg.optica.org/abstract.cfm?URI=ao-50-25-5012> (25 Sept. 2011).
30. Hagen, N. & Tkaczyk, T. S. Compound prism design principles, III: linear-in-wavenumber and optical coherence tomography prisms. *Applied Optics* **50**, 5023. ISSN: 0003-6935. <https://opg.optica.org/abstract.cfm?URI=ao-50-25-5023> (25 Sept. 2011).
31. Donati, G. B. Intorno alle strie degli spettri stellari. *Il Nuovo Cimento* **15**, 292–304. ISSN: 0029-6341. <http://link.springer.com/10.1007/BF02906594> (1 Dec. 1862).
32. Thollon, M. Nouveau spectroscope. *Journal de Physique Théorique et Appliquée* **7**, 141–148. ISSN: 0368-3893. <http://www.edpsciences.org/10.1051/jphystap:018780070014100> (1 1878).
33. Riccò, A. Combinazioni spettroscopiche a visione diretta. *Memorie della Società Degli Spettroscopisti Italiani*, vol. 8, pp. A21-A34 **8**, A21–A34. <https://adsabs.harvard.edu/full/1879MmSSI...8A..21R> (1879).
34. `scipy.optimize.minimize` — SciPy v1.13.0 Manual <https://docs.scipy.org/doc/scipy/reference/generated/scipy.optimize.minimize.html#scipy.optimize.minimize>.
35. Virtanen, P. *et al.* SciPy 1.0: fundamental algorithms for scientific computing in Python. *Nature Methods* 2020 **17**:3 **17**, 261–272. ISSN: 1548-7105. <https://www.nature.com/articles/s41592-019-0686-2> (3 Feb. 2020).
36. Gibert-Roca, M. On Improving the Efficiency of Organic Photovoltaic Devices : Novel Strategies. <https://ddd.uab.cat/record/265797> (May 2022).
37. Best Research-Cell Efficiency Chart | Photovoltaic Research | NREL <https://www.nrel.gov/pv/cell-efficiency.html>.
38. Rasi, D. D. C. & Janssen, R. A. J. Advances in Solution-Processed Multijunction Organic Solar Cells. *Advanced Materials* **31**, 1806499. ISSN: 0935-9648. <https://onlinelibrary.wiley.com/doi/10.1002/adma.201806499> (10 Mar. 2019).

39. Cui, Y. *et al.* Wide-gap non-fullerene acceptor enabling high-performance organic photovoltaic cells for indoor applications. *Nature Energy* **4**, 768–775. ISSN: 2058-7546. <https://www.nature.com/articles/s41560-019-0448-5> (9 Aug. 2019).
40. Yang, Y., Xue, C., Yin, H., Chen, Z. & Hao, X.-T. Bandgap matching strategy for organic photovoltaic cells in oceanic applications. *Cell Reports Physical Science* **3**, 100861. ISSN: 26663864. <https://linkinghub.elsevier.com/retrieve/pii/S2666386422001357> (5 May 2022).
41. Liu, Q., Fang, J., Wu, J., Zhu, L., Guo, X., Liu, F. & Zhang, M. Tuning Aggregation Behavior of Polymer Donor *<i>via</i>* *<scp>Molecular-Weight</scp>* Control for Achieving 17.1% Efficiency Inverted Polymer Solar Cells. *Chinese Journal of Chemistry* **39**, 1941–1947. ISSN: 1001-604X. <https://onlinelibrary.wiley.com/doi/10.1002/cjoc.202100112> (7 July 2021).
42. Guo, Q., Guo, Q., Geng, Y., Tang, A., Zhang, M., Du, M., Sun, X. & Zhou, E. Recent advances in PM6:Y6-based organic solar cells. *Materials Chemistry Frontiers* **5**, 3257–3280. ISSN: 2052-1537. <https://xlink.rsc.org/?DOI=D1QM00060H> (8 2021).
43. Wang, J. *et al.* Tandem organic solar cells with 20.6% efficiency enabled by reduced voltage losses. *National Science Review* **10**, nwad085. ISSN: 2095-5138. <https://academic.oup.com/nsr/article/doi/10.1093/nsr/nwad085/7095866> (6 May 2023).
44. Zheng, Z., Wang, J., Bi, P., Ren, J., Wang, Y., Yang, Y., Liu, X., Zhang, S. & Hou, J. Tandem Organic Solar Cell with 20.2% Efficiency. *Joule* **6**, 171–184. ISSN: 25424351. <https://linkinghub.elsevier.com/retrieve/pii/S2542435121005869> (1 Jan. 2022).
45. Cui, Y. *et al.* Single-Junction Organic Photovoltaic Cell with 19% Efficiency. *Advanced Materials* **33**, 2102420. ISSN: 0935-9648. <https://onlinelibrary.wiley.com/doi/10.1002/adma.202102420> (41 Oct. 2021).
46. Zhan, L., Li, S., Lau, T.-K., Cui, Y., Lu, X., Shi, M., Li, C.-Z., Li, H., Hou, J. & Chen, H. Over 17% efficiency ternary organic solar cells enabled by two non-fullerene acceptors working in an alloy-like model. *Energy & Environmental Science* **13**, 635–645. ISSN: 1754-5692. <https://xlink.rsc.org/?DOI=C9EE03710A> (2 Feb. 2020).
47. Cui, Y. *et al.* Over 16% efficiency organic photovoltaic cells enabled by a chlorinated acceptor with increased open-circuit voltages. *Nature Communications* **10**, 2515. ISSN: 2041-1723. <https://www.nature.com/articles/s41467-019-10351-5> (1 June 2019).

48. Nielsen, C. B., Holliday, S., Chen, H.-Y., Cryer, S. J. & McCulloch, I. Non-Fullerene Electron Acceptors for Use in Organic Solar Cells. *Accounts of Chemical Research* **48**, 2803–2812. ISSN: 0001-4842. <https://pubs.acs.org/doi/10.1021/acs.accounts.5b00199> (11 Nov. 2015).
49. Shockley, W. & Queisser, H. J. Detailed Balance Limit of Efficiency of p -n Junction Solar Cells. *Journal of Applied Physics* **32**, 510–519. ISSN: 0021-8979. <https://pubs.aip.org/jap/article/32/3/510/505950/Detailed-Balance-Limit-of-Efficiency-of-p-n> (3 Mar. 1961).
50. Kim, T. H., Park, N. W., Saeed, M. A., Jeong, S. Y., Woo, H. Y., Park, J. & Shim, J. W. Record indoor performance of organic photovoltaics with long-term stability enabled by self-assembled monolayer-based interface management. *Nano Energy* **112**, 108429. ISSN: 22112855. <https://linkinghub.elsevier.com/retrieve/pii/S2211285523002665> (July 2023).
51. Alkhalayfeh, M. A., Aziz, A. A., Pakhuruddin, M. Z., Katubi, K. M. M. & Ahmadi, N. Recent Development of Indoor Organic Photovoltaics. *physica status solidi (a)* **219**, 2100639. ISSN: 1862-6300. <https://onlinelibrary.wiley.com/doi/10.1002/pssa.202100639> (5 Mar. 2022).
52. Cui, Y., Hong, L. & Hou, J. Organic Photovoltaic Cells for Indoor Applications: Opportunities and Challenges. *ACS Applied Materials & Interfaces* **12**, 38815–38828. ISSN: 1944-8244. <https://pubs.acs.org/doi/10.1021/acsmami.0c10444> (35 Sept. 2020).
53. Busireddy, M. R., Huang, S.-C., Su, Y.-J., Lee, Z.-Y., Wang, C.-H., Scharber, M. C., Chen, J.-T. & Hsu, C.-S. Eco-Friendly Solvent-Processed Dithienosilicon-Bridged Carbazole-Based Small-Molecule Acceptors Achieved over 25.7% PCE in Ternary Devices under Indoor Conditions. *ACS Applied Materials & Interfaces* **15**, 24658–24669. ISSN: 1944-8244. <https://pubs.acs.org/doi/10.1021/acsmami.3c02966> (20 May 2023).
54. Lee, C., Lee, J., Lee, H. H., Nam, M. & Ko, D. Over 30% Efficient Indoor Organic Photovoltaics Enabled by Morphological Modification Using Two Compatible Non-Fullerene Acceptors. *Advanced Energy Materials* **12**. ISSN: 1614-6832. <https://onlinelibrary.wiley.com/doi/10.1002/aenm.202200275> (22 June 2022).
55. Ma, L.-K. *et al.* High-Efficiency Indoor Organic Photovoltaics with a Band-Aligned Interlayer. *Joule* **4**, 1486–1500. ISSN: 25424351. <https://linkinghub.elsevier.com/retrieve/pii/S2542435120302282> (7 July 2020).

56. Lübke, D., Hartnagel, P., Angona, J. & Kirchartz, T. Comparing and Quantifying Indoor Performance of Organic Solar Cells. *Advanced Energy Materials* **11**, 2101474. ISSN: 1614-6832. <https://onlinelibrary.wiley.com/doi/10.1002/aenm.202101474> (34 Sept. 2021).
57. Hofinger, J., Weber, S., Mayr, F., Jodlbauer, A., Reinfelds, M., Rath, T., Trimmel, G. & Scharber, M. C. Wide-bandgap organic solar cells with a novel perylene-based non-fullerene acceptor enabling open-circuit voltages beyond 1.4 V. *Journal of Materials Chemistry A* **10**, 2888–2906. ISSN: 2050-7488. <https://xlink.rsc.org/?DOI=D1TA09752K> (6 Feb. 2022).
58. Hadipour, A., de Boer, B. & Blom, P. Organic Tandem and Multi-Junction Solar Cells. *Advanced Functional Materials* **18**, 169–181. ISSN: 1616-301X. <https://onlinelibrary.wiley.com/doi/10.1002/adfm.200700517> (2 Jan. 2008).
59. Wang, J., Zheng, Z., Zu, Y., Wang, Y., Liu, X., Zhang, S., Zhang, M. & Hou, J. A Tandem Organic Photovoltaic Cell with 19.6% Efficiency Enabled by Light Distribution Control. *Advanced Materials* **33**, 2102787. ISSN: 0935-9648. <https://onlinelibrary.wiley.com/doi/10.1002/adma.202102787> (39 Oct. 2021).
60. Green, M. A. Radiative efficiency of state-of-the-art photovoltaic cells. *Progress in Photovoltaics: Research and Applications* **20**, 472–476. ISSN: 1062-7995. <https://onlinelibrary.wiley.com/doi/10.1002/pip.1147> (4 June 2012).
61. Rau, U., Blank, B., Müller, T. C. & Kirchartz, T. Efficiency Potential of Photovoltaic Materials and Devices Unveiled by Detailed-Balance Analysis. *Physical Review Applied* **7**, 044016. ISSN: 2331-7019. <http://link.aps.org/doi/10.1103/PhysRevApplied.7.044016> (4 Apr. 2017).
62. Benduhn, J. *et al.* Intrinsic non-radiative voltage losses in fullerene-based organic solar cells. *Nature Energy* **2**, 17053. ISSN: 2058-7546. <https://www.nature.com/articles/nenergy201753> (6 Apr. 2017).
63. Chen, X.-K. *et al.* A unified description of non-radiative voltage losses in organic solar cells. *Nature Energy* **6**, 799–806. ISSN: 2058-7546. <https://www.nature.com/articles/s41560-021-00843-4> (8 June 2021).
64. Azzouzi, M., Yan, J., Kirchartz, T., Liu, K., Wang, J., Wu, H. & Nelson, J. Nonradiative Energy Losses in Bulk-Heterojunction Organic Photovoltaics. *Physical Review X* **8**, 031055. ISSN: 2160-3308. <https://link.aps.org/doi/10.1103/PhysRevX.8.031055> (3 Sept. 2018).

65. Vandewal, K., Benduhn, J. & Nikolis, V. C. How to determine optical gaps and voltage losses in organic photovoltaic materials. *Sustainable Energy & Fuels* **2**, 538–544. ISSN: 2398-4902. <https://xlink.rsc.org/?DOI=C7SE00601B> (3 Feb. 2018).
66. Liu, L. *et al.* 4-Terminal Inorganic Perovskite/Organic Tandem Solar Cells Offer 22% Efficiency. *Nano-Micro Letters* **15**, 23. ISSN: 2311-6706. <https://link.springer.com/10.1007/s40820-022-0095-2> (1 Dec. 2023).
67. Rodríguez-Martínez, X., Pascual-San-José, E. & Campoy-Quiles, M. Accelerating organic solar cell material's discovery: high-throughput screening and <i>big data</i>. *Energy & Environmental Science* **14**, 3301–3322. ISSN: 1754-5692. <https://xlink.rsc.org/?DOI=D1EE00559F> (6 June 2021).
68. Yan, J. *et al.* Identifying structure–absorption relationships and predicting absorption strength of non-fullerene acceptors for organic photovoltaics. *Energy & Environmental Science* **15**, 2958–2973. ISSN: 1754-5692. <https://xlink.rsc.org/?DOI=D2EE00887D> (7 July 2022).
69. Kim, S., Márquez, J. A., Unold, T. & Walsh, A. Upper limit to the photovoltaic efficiency of imperfect crystals from first principles. *Energy & Environmental Science* **13**, 1481–1491. ISSN: 1754-5692. <https://xlink.rsc.org/?DOI=D0EE00291G> (5 May 2020).
70. Hofinger, J., Putz, C., Mayr, F., Gugujonovic, K., Wielend, D. & Scharber, M. C. Understanding the low voltage losses in high-performance non-fullerene acceptor-based organic solar cells. *Materials Advances* **2**, 4291–4302. ISSN: 2633-5409. <https://pubs.rsc.org/en/content/articlehtml/2021/ma/d1ma00293ghttps://pubs.rsc.org/en/content/articlelanding/2021/ma/d1ma00293g> (13 July 2021).
71. Liu, Q. *et al.* 18% Efficiency organic solar cells. *Science Bulletin* **65**, 272–275. ISSN: 20959273. <https://linkinghub.elsevier.com/retrieve/pii/S2095927320300013> (4 Feb. 2020).
72. Sun, C., Pan, F., Bin, H., Zhang, J., Xue, L., Qiu, B., Wei, Z., Zhang, Z. G. & Li, Y. A low cost and high performance polymer donor material for polymer solar cells. *Nature Communications* **9**, 1–10. ISSN: 2041-1723. <https://www.nature.com/articles/s41467-018-03207-x> (1 Feb. 2018).
73. Xu, Z. *et al.* Understanding the Morphology of High-Performance Solar Cells Based on a Low-Cost Polymer Donor. *ACS Applied Materials & Interfaces* **12**, 9537–9544. ISSN: 1944-8244. <https://pubs.acs.org/doi/10.1021/acsami.9b22666> (8 Feb. 2020).

74. Pascual-San-José, E., Rodríguez-Martínez, X., Adel-Abdelaleim, R., Stella, M., Martínez-Ferrero, E. & Campoy-Quiles, M. Blade coated P3HT:non-fullerene acceptor solar cells: a high-throughput parameter study with a focus on up-scalability. *Journal of Materials Chemistry A* **7**, 20369–20382. ISSN: 2050-7488. <https://xlink.rsc.org/?DOI=C9TA07361B> (35 2019).
75. Baran, D. *et al.* Reducing the efficiency-stability-cost gap of organic photovoltaics with highly efficient and stable small molecule acceptor ternary solar cells. *Nature Materials* **16**. Paper of the O-IDFBR synthesis, 363–369. ISSN: 14764660. <https://www.nature.com/articles/nmat4797> (3 Nov. 2017).
76. Yan, J., Rezasoltani, E., Azzouzi, M., Eisner, F. & Nelson, J. Influence of static disorder of charge transfer state on voltage loss in organic photovoltaics. *Nature Communications* **12**, 1–12. ISSN: 20411723. <http://dx.doi.org/10.1038/s41467-021-23975-3> (1 2021).
77. Liu, S. *et al.* High-Performance Pseudo-Bilayer Organic Solar Cells Enabled by Sequential Deposition of D18/Y6 Chloroform Solution. *ACS Applied Energy Materials* **6**, 5047–5057. ISSN: 25740962. <https://pubs.acs.org/doi/full/10.1021/acsaem.3c00694> (9 May 2023).
78. Wu, Y., Zheng, Y., Yang, H., Sun, C., Dong, Y., Cui, C., Yan, H. & Li, Y. Rationally pairing photoactive materials for high-performance polymer solar cells with efficiency of 16.53%. *SCIENCE CHINA Chemistry* **63**, 265–271. ISSN: 1674-7291. <https://www.sciengine.com/10.1007/s11426-019-9599-1> (2 Sept. 2019).
79. Harillo-Baños, A., Rodríguez-Martínez, X. & Campoy-Quiles, M. Efficient Exploration of the Composition Space in Ternary Organic Solar Cells by Combining High-Throughput Material Libraries and Hyperspectral Imaging. *Advanced Energy Materials* **10**, 1902417. ISSN: 1614-6832. <https://onlinelibrary.wiley.com/doi/10.1002/aenm.201902417> (1 Jan. 2020).
80. Hunt, R. *The Reproduction of Colour* ISBN: 9780470024256. <https://onlinelibrary.wiley.com/doi/book/10.1002/0470024275> (Wiley, Sept. 2004).
81. Qian, D. *et al.* Design rules for minimizing voltage losses in high-efficiency organic solar cells. *Nature Materials* **17**, 703–709. ISSN: 14764660. <http://dx.doi.org/10.1038/s41563-018-0128-z> (8 2018).
82. Bristow, H. *et al.* Impact of Nonfullerene Acceptor Side Chain Variation on Transistor Mobility. *Advanced Electronic Materials* **5**, 1900344. ISSN: 2199-160X. <https://onlinelibrary.wiley.com/doi/full/10.1002aelm.201900344>

- wiley.com/doi/abs/10.1002/aelm.201900344https://onlinelibrary.wiley.com/doi/10.1002/aelm.201900344 (10 Oct. 2019).
- 83. Halaby, S., Martynowycz, M. W., Zhu, Z., Tretiak, S., Zhugayevych, A., Gonen, T. & Seifrid, M. Microcrystal Electron Diffraction for Molecular Design of Functional Non-Fullerene Acceptor Structures. *Chemistry of Materials* **33**, 966–977. ISSN: 15205002. <https://pubs.acs.org/doi/full/10.1021/acs.chemmater.0c04111> (3 Feb. 2021).
 - 84. Marina, S. *et al.* Polymorphism in Non-Fullerene Acceptors Based on Indacenodithienothiophene. *Advanced Functional Materials* **31**, 2103784. ISSN: 1616-3028. <https://onlinelibrary.wiley.com/doi/full/10.1002/adfm.202103784><https://onlinelibrary.wiley.com/doi/abs/10.1002/adfm.202103784> (29 July 2021).
 - 85. Markvart, T. Thermodynamics of losses in photovoltaic conversion. *Applied Physics Letters* **91**, 1–3. ISSN: 0003-6951. <https://pubs.aip.org/apl/article/91/6/064102/326374/Thermodynamics-of-losses-in-photovoltaic> (6 Aug. 2007).
 - 86. Rühle, S. Tabulated values of the Shockley–Queisser limit for single junction solar cells. *Solar Energy* **130**, 139–147. ISSN: 0038092X. <https://linkinghub.elsevier.com/retrieve/pii/S0038092X16001110> (June 2016).
 - 87. Rau, U. Reciprocity relation between photovoltaic quantum efficiency and electroluminescent emission of solar cells. *Physical Review B - Condensed Matter and Materials Physics* **76**, 085303. ISSN: 10980121. <https://journals.aps.org/prb/abstract/10.1103/PhysRevB.76.085303> (8 Aug. 2007).
 - 88. Adel, R., Morse, G., Silvestri, F., Barrena, E., Martinez-Ferrero, E., Campoy-Quiles, M., Tiwana, P. & Stella, M. Understanding the blade coated to roll-to-roll coated performance gap in organic photovoltaics. *Solar Energy Materials and Solar Cells* **245**, 111852. ISSN: 09270248. <https://linkinghub.elsevier.com/retrieve/pii/S0927024822002720> (Sept. 2022).
 - 89. Carlé, J. E. *et al.* Overcoming the Scaling Lag for Polymer Solar Cells. *Joule* **1**, 274–289. ISSN: 25424351. <https://linkinghub.elsevier.com/retrieve/pii/S2542435117300272> (2 Oct. 2017).
 - 90. Hösel, M., Angmo, D., Søndergaard, R. R., dos Reis Benatto, G. A., Carlé, J. E., Jørgensen, M. & Krebs, F. C. High-Volume Processed, ITO-Free Superstrates and Substrates for Roll-to-Roll Development of Organic Electronics. *Advanced Science* **1**. ISSN: 2198-3844. <https://onlinelibrary.wiley.com/doi/10.1002/advs.201400002> (1 Dec. 2014).

91. Andersen, T. R. *et al.* Scalable, ambient atmosphere roll-to-roll manufacture of encapsulated large area, flexible organic tandem solar cell modules. *Energy & Environmental Science* **7**, 2925. issn: 1754-5692. <https://xlink.rsc.org/?DOI=C4EE01223B> (9 June 2014).
92. Krebs, F. C., Tromholt, T. & Jørgensen, M. Upscaling of polymer solar cell fabrication using full roll-to-roll processing. *Nanoscale* **2**, 873. issn: 2040-3364. <https://xlink.rsc.org/?DOI=b9nr00430k> (6 2010).